2015

Structure-Property Relationship of the Two-Photon Circular Dichroism of Compounds with Axial and Helical Chirality

Carlos Diaz
University of Central Florida

STRUCTURE-PROPERTY RELATIONSHIP OF THE TWO-PHOTON CIRCULAR DICHROISM OF COMPOUNDS WITH AXIAL AND HELICAL CHIRALITY

by

CARLOS DÍAZ
B.S. Universidad Central de Venezuela 2006

A dissertation submitted in partial fulfillment of the requirements
for the degree of Doctor of Philosophy
in the Department of Chemistry
in the College of Sciences
at the University of Central Florida
Orlando, Florida

Summer Term
2015

Major Professor: Florencio Hernández

ABSTRACT

Back in 1894 Lord Kelvin coined the term “chiral” in order to refer to molecules whose mirror images were not superimposable with themselves. Over the years, research has demonstrated the important role that chiral molecules play in life, chemistry, and biology as well as their importance in the development of new drugs and technologies.

The efforts to understand chiral systems have been mainly driven by spectroscopic methods that leverage on the opposite responses that enantiomers have to linear or circularly polarized light of both handedness. More specifically, Electronic Circular Dichroism (ECD) which measures the differences in linear absorption of left and right circularly polarized light has been the method *par excellence* for the spectroscopic characterization of chiral compounds. Unfortunately, the fact that ECD is based on linear absorption severely limits the use of this method in the near to far UV region. This is mainly due to the interferences generated by the strong linear absorption of common organic solvents and buffers in this portion of the light spectrum. Nevertheless, the fact remains that many chiral biomolecules of interest related to deceases like Alzheimer and Parkinson, exhibit most of their linear absorption in the near to far UV region where ECD cannot be employed for their study. Therefore, it has become an urgent necessity to develop spectroscopic methods to study chiral molecules that can circumvent the limitations of ECD at shorter wavelengths.

In order to overcome the existent limitations in linear chiral spectroscopy, the nonlinear equivalent of ECD arises as a promising alternative, i.e. Two-Photon Circular Dichroism (TPCD). Although, this phenomenon was theoretically predicted in 1975, it was not until 2008, with the introduction of the double-L scan, that a reliable and versatile method for the measurement of TPCD was introduced. The high sensitivity of this method is based on the use of

"twin" pulses that allow accounting for fluctuations in the excitation source that prevented the experimental realization of the measurement. The first measurement of a full TPCD spectrum was performed on BINOL enantiomers and the results were supported and discussed with the help of theoretical calculations. After that seminal work, we embarked in expanding the understanding of the structure-property relationship of TPCD by performing, systematically, a series of theoretical-experimental studies in chiral biaryl derivatives and compounds with helical chirality.

In **Chapter 2** we present the theoretical-experimental study of the effect of the π-electron delocalization curvature on the TPCD of molecules with axial chirality. The targeted molecules for this part of our investigation were S-BINOL, S-VANOL, and S-VAPOL. Our findings revealed that an increase in the TPCD signal, within this series of compounds, was related to the curvature of the π–electron delocalization. The contributions of the different transition moments to the two-photon rotatory strength support our outcomes.

Then, in **Chapter 3** we introduce the development of the Fragment-Recombination Approach (FRA) for the calculation of the TPCD spectra of large molecules. This simple but powerful method is based on the additivity of the TPCD signal, and is subject to a strict conditional fragmentation approach. FRA-TPCD is demonstrated, theoretically, in two hypothetical molecular systems from the biaryl derivatives family.

Afterward, in **Chapter 4** we show the first experimental demonstration of FRA-TPCD through the conformational analysis of an axially-chiral Salen ligand in solution (AXF-155). The FRA-TPCD spectra calculated for the different isomers of AXF-155 allowed narrowing the number of possible isomers of this complex molecule in THF solution to only two. This represents a significant improvement from previously reported results using ECD.

Subsequently, in **Chapter 5** we present the study of the effect of intramolecular charge transfer (ICT) in S-BINAP, an axially dissymmetric diphosphine ligand with strong ICT. The evaluation of the performance of two different exchange-correlation functional (XCF) confirmed that in order to properly predict the theoretical TPCD spectrum of a molecule exhibiting strong ICT, it is required to use an XCF such as CAM-B3LYP. In addition, our findings revealed the importance of considering an adequate number of excited states in order to be able to fully reproduce the experimental TPCD spectrum, thus avoiding wrong assignments of theoretical transitions to experimental spectral features.

Finally, and expanding on our previous study, in **Chapter 6** we investigated the effect of the nature of ICT on two hexahelicene derivatives. Our investigation demonstrated that the TPCD signal of chiral molecules with strong ICT does not only depend on the strength of this effect but on its nature, i.e. extension of the π–electronic delocalization increasing beyond (EXO-ICT) or within (ENDO-ICT) the helicene core.

In **summary**, with the results presented in this thesis we closed a first loop in the understanding of the structure-property relationship of TPCD. In the future, we expect to deepen in our knowledge of the structure-property relationship of this phenomenon by studying further helicene derivatives with donor-acceptor motif, and through the application of FRA-TPCD to the conformational analysis of amino acids in peptides. We foresee numerous applications of TPCD for the study of optically active molecules with implications in biology, medicine, and the drug and food industry, and applications in nanotechnology, asymmetric catalysis and photonics.

To my wife Maryhen, my children David, Isaac, Aaron and Gabriel, my mother Aura and my siblings Wilmer, Roosvely and Roxaly. Thank you for all your unconditional love and support; you will always be my biggest inspiration in this world.

ACKNOWLEDGMENTS

First, foremost and above all things I want to express my thanksgivings to our Lord and Savior Jesus Christ for showing me plainly and clearly through the intersection of his Holy Mother, the most Blessed Virgin Mary, that he wanted me to become a PhD in chemistry.

This first acknowledgement takes me invariably to thank the person in whom the Lord invested the responsibility of guiding me to become a doctor in chemistry; I am talking about my true friend in Christ and my PhD mentor Dr. Florencio Eloy Hernández. Under no one else would I have attained the knowledge, the confidence and the skills that today I have. Dr. Hernández has sculpted my intellect, my way of thinking and my vision in his constant effort of making of me a true doctor in chemistry. But more important than all of the doctoral training that I have received from him is the true friendship in Christ that we have cultivated over these years.

I would also like to thank another person that played a key role in my coming to UCF, Dr. Pedro Patiño, a close friend of mine and my teacher, who introduced me to Dr. Hernández and was the first person to talk to me about the possibility of getting a PhD in chemistry.

While at Dr. Hernández Lab, many people have helped me and supported me throughout this journey. I would like to thank Dr. Carlos Toro and Dr. Leonardo de Boni who were the first persons to guide me into the world of lasers. Then, I would like to thank Warinya who has helped me in a selfless way whenever I have needed her. Additionally, I would like to thank my lab co-workers, Yuly and Julie for all their support, especially during the last stages of my PhD. Also, I would like to thank my friends from Venezuela, Dr. Lorenzo Echevarria and Dr. Carlos Borras for the incredible time that I spent in the lab by their side and for their continuous support. Finally, I would like to thank Dr. Stephen Kuebler and the people from his group, Rashi, Ping and Cassey, for the fun times that our groups spent together during many lunches.

I also want to recognize all the people that collaborated in different parts of the research presented in this dissertation. Among them I would like to mention, Dr. Haining Wang and Dr. Sergio Tafur, for helping us to implement Dalton in the chemistry department and at STOKES. Dr. Suren Tatulian, for being so kind and help us in the measurement of many ECD spectra. Dr. Andrew Frazer and Dr. Alma Morales for synthesizing some of the compounds presented in this work. And finally, Dr. Antonio Rizzo, whom I never had the pleasure to meet but without his help all the theoretical calculations of TPCD would not have been possible.

I want to specially acknowledge the National Science Foundation (Projects CHE-0832622 and CHE-0840431) for providing the funds to carry out this research and STOKES ARCC at UCF for providing countless hours of computing time.

I must also recognize the key role that my immediate family and my in-laws have played in helping me to finish my PhD. To my wife Maryhen, thank you for being always by my side, it is thanks to you that I arrived to this beautiful country and that I had the opportunity to pursue a PhD in chemistry. My beloved wife also has given me my four boys David, Isaac, Aaron and Gabriel, who have been the greatest motivation on this earth to finish this episode of my life. My children bring me to my mom Aura, without her help in raising my kids I would not have been able to finish my PhD; I really cannot put into words and could never be able to pay to you all the things that you have done for me; thank you mom. Then, my deepest gratitude to my three siblings, Wilmer, Roosvely and Roxaly; you have been a constant source of inspiration and an incredible support throughout these years. Last, but not least important, is the role that my in-laws, Maribel, Enio and Samuel have played in helping me finishing my PhD, especially by taking me into their house during the last year of my PhD, not as a guest but as a son.

TABLE OF CONTENTS

LIST OF FIGURES

LIST OF TABLES

LIST OF ACRONYMS AND ABREVIATIONS

A6	*P*-(+)-1-aza[6]helicene
AXF-155	[2,2'-(1E,1'E)-(R)-1,1'-binaphthyl-2,2'-diylbis(azan-1-yl-1-ylidene) bis(methan-1-yl-1-ylidene)bis(4-((7-(diphenylamino)-9,9-dihexyl-9H-fluoren-2-l)ethynyl)phenol)]
AXF-169’	[(E)-4-((7-(diphenylamino)-9,9-dihexyl-9H-fluoren-2-yl)ethynyl)-2-((naphthalen-2-ylimino-1-methyl) methyl)phenol]
B3LYP	Becke 3-parameter Lee-Yang-Parr hybrid functional
C-AXF-155	[2,2'-(1E,1'E)-1,1'-binaphthyl-2,2'-diylbis(azan-1-yl-1-ylidene) bis(methan-1-yl-1-ylidene)bis(4-ethynyl)phenol)]
CAM-B3LYP	Coulomb attenuating method Becke 3-parameter Lee-Yang-Parr hybrid functional
CN6	*M*-(-)-2-[4-(cyanophenyl)-1-ethynyl]carbo[6]helicene
c	Speed of light ($3x10^{8}$ m s^{-1})
CARS	Coherent Anti-Stokes Raman Scattering
CD	Circular dichroism
CH_2Cl_2	Dichloromethane
cm	Centimeter
CT	Charge transfer
DFT	Density functional theory
DFWM	Degenerate Four-Wave Mixing
e	Electron charge ($1.602x10^{-19}$ Coulombs)
ECD	Electronic circular dichroism

ENDO-ICT	Intramolecular charge transfer within the helicene core.
EXO-ICT	Intramolecular charge transfer beyond the helicene core
f	Oscillator strength
fs	Femtosecond (10^{-15} s)
FWHM	Full width at half maximum
FRA	Fragmentation-recombination approach
FROG	Frequency-resolved optical gaiting
$g\ \left(n\omega, \omega_{0f}, \Gamma\right)$	Normalized lineshape for an *n*-photon excitation
GM	Goppert-Mayer unit for the TPA cross-section and TPCD (1×10^{-50} cm^4 s photon^{-1} molecule^{-1})
h	Planck's constant (6.626×10^{-34} m^2 kg s^{-1})
H	HOMO (highest occupied molecular orbital)
Hz	Hertz (unit of frequency)
ICT	Intramolecular charge transfer
kJ	Kilojoules
L	LUMO (lowest unoccupied molecular orbital)
LCPL	Left circularly polarized light
LPL	Linearly polarized light
m	Mass of the electron (9.109×10^{-31} kg)
M	Molar (unit of concentration)
M1	(S,S)-spiro[8.8]4,5(1,2),13,14(2,3)-tetranaphtalenaheptadecane
M2	(Δ,S)-(1,1′-binaphthalene-2,2′diolato)(bis(1,2-benzenediolato)sulfate(VI))
M	Two-photon magnetic transition dipole matrix element

MCD	Magnetic circular dichroism
MD	Molecular dynamics
MM	Molecular mechanics
MPA	Multi-photon absorption
mL	Milliliter
n_0	Linear refractive index
n_2	Nonlinear refractive index
Nd:YAG	Neodymium-doped yttrium aluminum garnet
nm	Nanometer (10^{-9} m)
NT	Normalized transmittance
OPA	One-photon absorption
OPG	Optical parametric generator
ORD	Optical rotatory dispersion
P	Two-photon electric transition dipole matrix element
PCM	Polarizable continuum model
Ph	Phenyl group
ps	Picosecond (10^{-9} s)
q^d	Dynamic component of the solvent reaction field
q^i	Delayed component of the solvent reaction field
QM	Quantum mechanics
R_{0f}^{ECD}	Rotatory strength
R-BINOL	(R)-(+)-1,1'-bi(2-naphthol)
RCPL	Right circularly polarized light

ROA	Raman optical activity
s	Seconds
S_0	Ground state, singlet
S_1	First excited state, singlet
S_2	Second excited state, singlet
S_n	n^{th} excited state, singlet
S_{ii}^{0f}	Two-photon transition matrix elements
S-BINAP	(S)-(+)-(1,1′-Binaphthalene-2,2′-diyl)bis(diphenylphosphine)
S-BINOL	(S)-(-)-1,1’-bi(2-naphthol)
SAS	Solvent accessible surface
SES	Solvent excluded surface
SFG	Sum frequency generation
SHG	Second harmonic generation
SCRF	Self-consistent reaction field
SRF	Solvent reaction field
S-VANOL	(S)–3,3’–Diphenyl–[2,2’–binaphthalene]– 1,1’–diol
S-VAPOL	(S)–2,2’–Diphenyl– [3,3’–biphenanthrene]–4,4’–diol
T	Two-photon electric transition quadrupole matrix element
TPA	Two-photon absorption
TPIF	Two-photon induced fluorescence
TD-DFT	Time dependent density functional theory
THF	Tetrahydrofuran
UV	Ultraviolet

VCD	Vibrational circular dichroism
VIS	Visible
w_0	Beam radius at the focal plane
XCF	Exchange correlation functional
z_0	Rayleigh range
#CN	CN6-like helicenes
n-π*	Transition from a non-bonding orbital (n) to an antibonding π orbital (π*)
π-π*	Transition from a bonding π orbital to an antibonding π orbital (π*)
α	One-photon absorption coefficient
β	Two-photon absorption coefficient
γ	Three-photon absorption coefficient
Γ	Empirical linewidth parameter
δ^{TPA}	Two-photon absorption cross-section
δ_L^{TPA}	Two-photon absorption cross-section for left circularly polarized light
δ_R^{TPA}	Two-photon absorption cross-section for right circularly polarized light
$\Delta\delta^{TPCD}$	Two-photon circular dichroism
Δf	Lippert's function
ΔG_{sol}	Free energy of solvation
ΔG_{el}	Electrostatic contribution to the free energy
ΔG_{dr}	Dispersion-repulsion contribution to the free energy
ΔG_{cav}	Cavitation free energy

$\Delta\mu$	Difference between ground and excited state dipole moment
ε	Molar Absorptivity
ε_0	Dielectric constant
$\varepsilon_{\beta\rho\alpha}$	Levi-Civita alternating tensor
θ	Ellipticity
λ_{max}	Maximum absorption wavelength
μ_{0f}	Transition moment (ground to final singlet state)
μ_E	Excited state permanent dipole moment
μ_G	Ground state permanent dipole moment
$\tilde{\nu}_A$	Absorption frequency
$\tilde{\nu}_F$	Emission frequency
$\chi^{(n)}$	n^{th} order nonlinear susceptibility tensor
Ψ_0	Ground state wavefunction
Ψ_f	Excited (final) state wavefunction
ω	Circular frequency

CHAPTER 1 : INTRODUCTION

Light is the most abundant form of energy that surrounds us. Its interaction with matter is what gives color to our world, and has caught the attention of thinkers and researchers for several millennia. [1, 2] Particularly, the interest among scientists and engineers in the understanding of light-matter interaction of novel atomic and molecular assemblies has significantly increased since the late 20th century. This is largely due to the direct link between the optical properties of these entities and some of their potential technological applications. Among the innovative research in chemistry using light one can mention, optical data storage, [3] human cells bioimaging [4] and single molecule imaging. [5] The impact of the latter two areas of research can be fully understood after realizing that the 2014 Nobel Prize in chemistry was awarded to advances in these fields. [6] All the efforts made in order to understand the optical properties of novel materials have been primarily driven by the development of a series of spectroscopic techniques that reveal important information about their electronic properties and structural features. The combination of these two important components, material design and spectroscopy, seeks to connect the fundamental electronic structure of any molecule with its performance in the application of interest. Furthermore, the now common availability in research laboratories of ultrafast laser systems had accelerated the advances in photophysics and photochemistry, by opening new possibilities that have allowed investigators to deepen their understanding of optical phenomena at the molecular level. [7]

Up to the 1950's, linear spectroscopy techniques, i.e. those based on One-Photon Absorption (OPA), dominated the research in photophysics and photochemistry. But the advent of Laser systems in 1960, allowed for the development of nonlinear spectroscopic techniques,

i.e. those based in multiphoton (*n*-photon) absorption. This novel approach has been proved to offer a series of advantages over linear spectroscopy techniques. In multiphoton processes the excitation takes place at a wavelength that is 1/*n* times that of the corresponding energy gap - degenerate case (degenerate case). This increase in the excitation wavelength translates into negligible absorption, reduced scattering and sample photodamage along with an improved penetration in absorbing or scattering media. [8] Furthermore, the I^n dependence of this processes (where I is the intensity of the laser pulse) allows for a higher degree of spatial resolution. [9] These series of advantages have made the use of multiphoton-based processes especially attractive to researchers working in imaging of highly absorbing and scattering media such as biological samples. These advantages have resulted in many novel and promising applications in the fields of bio-imaging and photodynamic therapy. [4, 10]

Among the many possibilities for multi-photon spectroscopy, two-photon spectroscopy has indisputably become one of the top techniques in the analysis of optical properties of molecules. [11, 12] In particular, Two-Photon Absorption (TPA) has been extensively used in the characterization of organic molecules with applications in microscopy, [13] optical limiting [14] and 3D microfabrication, [15] among others. In addition, the design of new molecules exhibiting TPA has been assisted by modern theoretical-computational methods. [11, 12] The access to these powerful tools have increased the efficiency of the design of TPA chromophores, by allowing investigators to finely tune the TPA properties of molecular systems before carrying out their synthesis in the laboratory.

Since the late 1980s, researchers in nonlinear optics have started developing new methods for characterizing molecular systems exhibiting optical activity, [16-24] which is a property exclusively observed in chiral entities, i.e. asymmetric molecules with a non-superimposable

mirror image. The origin of this research interest is rooted in two main reasons: 1) chiral molecules are of the utmost importance in many different areas such as the design of new drugs [25] and asymmetric catalysts, [26] and the understanding of many biological processes related to the origin of life itself, [27] and 2) Electronic Circular Dichroism (ECD), the gold standard technique for the characterization of chiral systems, [28] is based in OPA. ECD measures the differences in OPA when excitation is carried out with circularly polarized light of different handedness. Therefore, the study of chiral molecules in the UV region using ECD is hindered by strong OPA from solvents and buffers and increased scattering of inhomogeneous samples observed in this spectral region. [29] This set of obstacles can potentially be overcome by leveraging on the advantages of multiphoton excitation. To this respect, processes such as second harmonic generation (SHG), [16] sum-frequency generation (SFG), [17] nonlinear optical activity [18, 19] and multiphoton optical rotation have been proposed. [20-24] However, none of these techniques is a truly polarization dependent method like ECD. Fortunately, the nonlinear equivalent of ECD called Two-Photon Circular Dichroism (TPCD), was theoretically predicted in the 1970s [30, 31] and computationally implemented three decades latter. [32] The first step towards the experimental measurement of this property was taken by Richardson and co-workers in 1995 [33] using fluorescence-detected two-photon circular dichroism (FD-TPCD). However, it was not until the advent of the double-L scan [34] that a reliable a versatile method for measuring TPCD over a broad spectral range was developed. Using this technique, Hernandez and co-workers measured the entire TPCD spectrum of BINOL enantiomers. [35]

Hernandez *et al.* seminal research in this field served to prove the viability of experimental TPCD measurements using the double-L scan method and it is the starting point of

this dissertation. Next, we present a thorough description of the theoretical and experimental details of the linear and nonlinear optical properties subject of this dissertation.

1.1. Fundamentals of linear and non-linear absorption processes

1.1.1 One-Photon Absorption

The understanding of the relationship between the electronic structure of a molecule and its properties has to start from one of the simplest and most common cases of light-matter interaction, i.e. linear absorption of electromagnetic radiation, also known as One-Photon absorption. In this process the absorption of one photon induces an electronic transition from an initial state (S_0) to a final excited state (S_n) (See Figure 1-1).

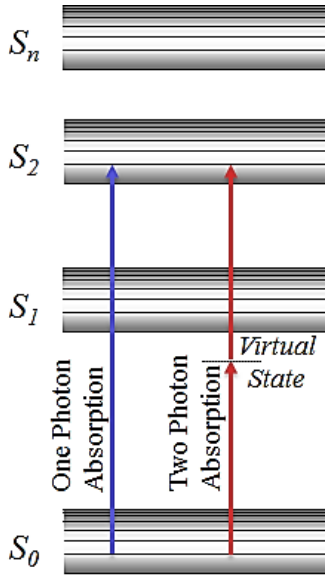

Figure 1-1. Simplified Jablonski diagram

The electromagnetic radiation that impinges on the molecular system will tend to create a perturbation in its electron cloud. If the oscillation frequency of the electric field of the incident photon is equal to one of the natural oscillation frequencies of the molecule, then the two interacting parts, i.e. the photon and the molecule, are said to be at a resonance condition. This

specific state leads to the absorption of the incident photon, generating an oscillating electric dipole within the molecule, i.e. the transition dipole moment (μ_{0f}), and taking the molecule to the excited state S_n. The probability of an electronic transition to take place is strictly bound to μ_{0f} . This is manifested in the following relationship between molar absorptivity (ε) and μ_{0f} , [36]

$$\int \varepsilon d\tilde{\nu} = \left(2.512\times10^{19} l.mol^{-1}cm^{-3}\right)\frac{\tilde{\nu}}{e^2}\left|\mu_{0f}\right|^2, \tag{1-1}$$

where $\tilde{\nu}$ is the frequency of the light expressed in cm^{-1}, e is the electron charge and $\left|\mu_{0f}\right|^2$ is the transition probability.

An additional factor that needs to be taken into consideration is that for many practical purposes OPA measurements are usually performed in solution. If the molecule being measured is polar, the dielectric properties of the solvent can significantly alter the electronic cloud of both, the ground and excited states of the molecule, with the latter being more affected. This perturbation results in a change in the energy gap between these states. The magnitude of the modified energy separation between the ground and the excited state, due to the presence of the solvent, can be determined from the Lippert equation, [37]

$$\tilde{\nu}_A - \tilde{\nu}_F = \frac{2}{hc}\left(\frac{\varepsilon-1}{2\varepsilon+1} - \frac{n^2-1}{2n^2+1}\right)\frac{\left(\mu_E-\mu_G\right)^2}{a^3}, \tag{1-2}$$

here $\tilde{\nu}_A$ and $\tilde{\nu}_F$ are the absorption and emission frequencies in cm^{-1}, respectively, ε and n are the solvent dielectric constant and refractive index, respectively, c is the speed of light *in vacuo*, h is the Planck's constant, and a the radius of the cavity in which the molecule is located. μ_E and μ_G represent the dipole moment of the molecules in their excited and ground state, respectively. The

difference between $\tilde{\nu}_A$ and $\tilde{\nu}_F$ refers to the energy separation between the ground and excited state.

A comprehensive understanding of OPA would not be complete without mentioning a series of additional rules that regulate the occurrence of electronic transitions. These rules are of purely quantum mechanical origin and therefore there are no exceptions to them. However, they can be relaxed by molecular interactions like the one described above between the solvent and the molecular system of interest. Next, a summary of the selection rules for electronic transitions is presented.

1.1.2 Selection Rules

From the dynamics presented above, it seems that the only criterion for an electronic transition to take place is that the energy of the incident photon is equal to that of the difference between S_0 and S_f. Nevertheless, in addition to this basic requirement, there are a series of additional constraints or *rules* that have to be fulfilled in order for OPA to take place. Selection rules are the ones that ultimately determine if a particular electronic transition is "allowed" or "forbidden". These set of rules are derived from the transition dipole moment integral, which involves the wave functions of the initial (Ψ_f) and final (Ψ_f) states: [36]

$$\mu_{0f} = \int \Psi_0^* \mu \Psi_f \, d\tau . \tag{1-3}$$

When the integral in Equation 1-3 vanishes for a given set of Ψ_0 and Ψ_f wave functions, the transition between these two states is forbidden and will not be observed in the experimental spectrum, unless the appropriate perturbation is applied. The absence of OPA when $\mu_{0f} = 0$ is implied in Equation 1-1. On the other hand, Equation 1-1 also indicates that excitations with

non-vanishing transition dipole moment integrals will be observed in the spectrum and their strength will be mainly determined by the magnitude of μ_{0f}.

The selection rules that apply to electronic transitions simply arise from all the conditions that always make the integral in Equation 1-3 equal to zero. Generally, there are two kinds of rules that apply to most chromophores. First, the *spin* selection rules ($\Delta S = 0$), is rooted in the fact that neither the dipole nor the quadrupole moment operators have any effect on the spin. Therefore, an electronic transition is spin allowed only if the multiplicity of the participating states is identical. Second, the *spatial symmetry* selection rules ($\Delta l = \pm 1$) are the result of the need of the integrand in Equation 1-3 to be totally symmetric in order to yield a non-zero value. As a consequence of this, for centrosymmetric molecules, transitions between states of the same symmetry are allowed while those between states of opposite symmetry are forbidden. [36]

In addition, it is important to consider a very specific but relevant case that gives rise to another selection rule. In their "one- electron theory", Condon, Altar and Eyring, [38] describe that if a molecule has either a plane or a center of symmetry, then either the vectors of the induced electric and magnetic dipoles are orthogonal or their sum is zero. However, in the specific case of a chromophore with two transitions, i.e. one electric and one magnetic, the magnetic and electric fields will not be orthogonal. This is due to the perturbation induced by the asymmetry in the states. One case where this rule can apply is to the relatively common n-π* excitations, that are electrically forbidden but magnetically allowed.

Overall, a considerable amount of structural information can be obtained from the study of the OPA spectrum of chromophores. Nevertheless, a variety of other phenomena with useful technological applications occur in the nonlinear regime. Next, a description of one of the most studied of those nonlinear phenomena is presented.

1.1.3 Nonlinear Absorption

In addition to the OPA case, a chemical species can also undergo an electronic transition by means of absorption of multiple photons. In the OPA case the energy of the incident photon has to match that of the energy difference between S_0 and S_f, while for the cases when n photons are absorbed (known as Multiphoton Absorption (MPA) or nonlinear absorption) this difference has to be equal to the addition of the energy of the n photons responsible for the excitation (See Figure 1-1). The possibility to induce electronic excitation by means of MPA was predicted by Göppert−Mayer in 1931, [39] where she specifically addressed the theoretical probability of simultaneous absorption of two photons, i.e. TPA (See Figure 1-1). Her hypothesis was that the transition could occur because of the existence of virtual states located in between real states (See Figure 1-1). In order to observe this phenomenon a high intensity light source was required. For this reason the experimental confirmation of her prediction came only after the invention of lasers, three decades later. [40]

In order to understand the dynamics of nonlinear absorption processes, it is important to consider the behavior of the polarization of the electron cloud in the presence of strong radiation, such as that generated by a laser source. When a molecular system is exposed to an external electric field similar in magnitude to interatomic electric fields, the behavior of the polarization starts deviating from the linearity observed in OPA and the electronic oscillations are better described by an anharmonic oscillator. This nonlinear behavior in response to the laser light is the origin of a variety of nonlinear phenomena. A Taylor expansion of the polarization of the material in the external electric field gives rise to a series of terms that can be associated with such phenomena, [41]

$$\vec{P} = \chi^{(1)} \cdot \vec{E} + \chi^{(2)} \cdot \vec{E}^2 + \chi^{(3)} \cdot \vec{E}^3 + \ldots + \chi^{(n)} \cdot \vec{E}^n , \tag{1-4}$$

where, $\chi^{(n)}$ are macroscopic parameters known as susceptibility tensors of n^{th} order. The first susceptibility $\chi^{(1)}$, describes the linear polarization of the medium, while the nonlinear susceptibilities $\chi^{(n+1)}$ (where *n = 1, 2, …*) describe the induced nonlinear polarization. In general, susceptibilities are complex numbers composed of a real and an imaginary part. The real part of $\chi^{(1)}$ is associated to the refractive index of the medium while its imaginary part is linked to the linear absorption (OPA) coefficient of a molecule.

There are many nonlinear phenomena described by the nonlinear susceptibilities. However, this section will only describe those associated to $\chi^{(3)}$. The real part of the third-order susceptibility $\left(\mathrm{Re}\chi^{(3)} \right)$ is related to the change induced in the refractive index due to the high intensity of the applied electric field ($I \propto E^2$). Then, the nonlinearity induces the appearance of a nonlinear refractive index coefficient (n_2), in addition to the refractive index of the material (n_0),

$$n(I) = n_0 + n_2 I , \tag{1-5}$$

here, n_2 is related to $\left(\mathrm{Re}\chi^{(3)} \right)$ through the following relationship,

$$\mathrm{Re}\chi^{(3)} = \frac{4n_0^2 \varepsilon_0}{3} n_2 , \tag{1-6}$$

where ε_0 is the vacuum permittivity. Two phenomena are a direct consequence of the self-modulation of the incident light due to the appearance of the nonlinear refractive index, i.e. self-focusing ($n_2 > 0$) and self-defocusing ($n_2 < 0$). [42]

On the other hand, the imaginary part of third-order susceptibility $\left(\mathrm{Im}\chi^{(3)}\right)$ is associated with the TPA of the media. The occurrence of nonlinear absorption phenomena leads to a complex dependence of the intensity of the radiation as it propagates through the absorbing media, [12]

$$\frac{dI(z)}{dz} = -\alpha I - \beta I^2 - \gamma I^3 - \eta I^4 - \ldots, \tag{1-7}$$

where, *I(z)* is the intensity of the incident light along the direction of propagation (the *z*-axis) and α, β, γ, and η are the one-, two-, three-, and four-photon coefficients of the medium, respectively. All of these absorption coefficients are related to the imaginary parts of the corresponding odd-numbered susceptibilities, e.g. $\mathrm{Im}\chi^{(1)}$ related to α, $\mathrm{Im}\chi^{(3)}$ related to β, $\mathrm{Im}\chi^{(5)}$ related to γ… For the specific case of two-photon absorption the relationship between $\mathrm{Im}\chi^{(3)}$ and β is given by,

$$\mathrm{Im}\chi^{(3)} = \frac{n_0^2 \varepsilon_0 c^2}{\omega}\beta. \tag{1-8}$$

A practical way to assess the nonlinear optical properties of a medium from measured spectra is by using the Kramers-Kronig (KK) relation. This bidirectional mathematical relation connects the real and imaginary parts of the susceptibility tensors, facilitating the calculation of the refractive index profile of a medium exclusively from its frequency-dependent absorption and *vice versa*. The KK relations for the specific case of $\chi^{(3)}$ are the following, [43]

$$\mathrm{Re}\left\{\chi^{(3)}(\omega)\right\} = \frac{2}{\pi}\wp\int_0^\infty \frac{\omega \mathrm{Im}\left\{\chi^{(3)}(\omega)\right\}}{\omega^2 - \omega'^2}\mathrm{d}\omega, \tag{1-9}$$

and

$$\mathrm{Im}\left\{\chi^{(3)}(\omega)\right\} = -\frac{2\omega'}{\pi}\wp\int_0^{\infty}\frac{\omega\mathrm{Re}\left\{\chi^{(3)}(\omega)\right\}}{\omega^2-\omega'^2}\mathrm{d}\omega, \tag{1-10}$$

where $\wp$ signifies that the integral has to be calculated using a limiting process called the Cauchy principal value. From the practical point of view this principal value is a warning to be cautious when integrating close to the singularity found in the denominator at the resonance frequency ω. [44]

In addition to the two-photon absorption coefficient β, another common way to quantify TPA is through the so called two-photon absorption cross-section (σ_2). This quantity is defined in terms of β through the following equation, [42]

$$\sigma_2 = \frac{\beta\hbar\omega}{N_0} \tag{1-11}$$

where ω is the frequency of the excitation radiation and N_0 is the total number of molecules that can be excited *via* TPA.

A final consideration that has to be addressed in this section is the differences between OPA and TPA that arise from the different selection rules that govern these two processes. [36] The symmetry selection rules dictate that in a centrosymmetric molecule, a transition occurring *via* OPA must take place between two states of opposite symmetry (odd parity). On the other hand, in the TPA case, the symmetry of the initial and final states has to be the same (even parity). This occurs because a TPA transition takes place through a virtual state whose symmetry is opposite to that of the other two states involved in the excitation. As a consequence of this, the set of

excited states that are accessible through one- and two-photon spectroscopies is completely different, at least for centrosymmetric molecules. [45, 46]

1.2. Theoretical framework for the calculation of linear and nonlinear absorption spectra

Nowadays, it is almost customary that every publication in experimental chemistry is accompanied by some sort of computational calculation of at least one or more of the properties of the reported compound. [47] The main reason for this widespread use of computational chemistry is that the computational cost of a reliable calculation has lowered at a rapid pace over the past three decades. This has given access to more chemists to this powerful tool that allow to support, and to better understand, the results obtained from the experiment.

The fields of linear and nonlinear optics have greatly benefited from the use of computational chemistry tools. Time Dependent Density Functional Theory (TD-DFT) [48, 49] is the most widely used method for the prediction of OPA and TPA spectra of a variety of chromophores. [50] This formalism, allows obtaining reliable predictions of the mentioned spectra at a moderate computational cost. However, this can only be attained if the proper combination of functional and basis set is used. For instance, it is known that the widely popular Becke 3-parameter Lee-Yang-Parr (B3LYP) [51-53] exchange correlation functional (XCF) erroneously underestimates excitation energies for molecules with charge transfer (CT) states. [54, 55] In order to correct this deficiency new functionals, like the Coulomb Attenuated Method B3LYP (CAM-B3LYP), [54, 55] are constantly being developed. The above mentioned XCFs are employed throughout this dissertation to perform excited state calculations employing TD-DFT. Next, the

necessary equations for the retrieval of OPA and TPA spectra from molecular parameters obtained from the TD-DFT calculations are presented.

1.2.1 One-Photon Absorption

The experimental OPA is usually reported in molar absorptivity (ε). This quantity is proportional to the oscillator strength (f_{0f}) of each electronic excited state which in turn depends on the electric transition dipole moment (μ_{0f}). For an electronic transition between the ground state and an excited state, the following equation establishes the relationship between the oscillator strength f_{0f} and the molar absorptivity $\varepsilon^{OPA}(\omega)$, [56]

$$\varepsilon^{OPA}(\omega) = \frac{2\pi^2 \omega N_A}{1000 \times ln(10)(4\pi\varepsilon_0)\hbar c_0} \times \frac{1}{\hbar} \sum_f g(\omega, \omega_{0f}, \Gamma) \frac{f_{0f}}{\omega_{0f}}, \tag{1-12}$$

$$\varepsilon^{OPA}(\omega) \approx 1.05495 \times 10^3 \times \omega \sum_f g(\omega, \omega_{0f}, \Gamma) \frac{f_{0f}}{\omega_{0f}}, \tag{1-13}$$

here, $\omega = 2\pi c_0 / \lambda$ is the circular frequency of the incident radiation, c_0 is the speed of light in *vacuo*), ε_0 is the vacuum permittivity, N_A is Avogadro's number, f_{0f} is calculated from μ_{0f} using,

$$f_{0f} = \frac{2 m_e \omega_{0f} |\mu_{0f}|^2}{3\hbar e^2}, \tag{1-14}$$

$g(\omega, \omega_{0f}, \Gamma)$ is the normalized line shape centered at $\omega = \omega_{0f}$ and with a full width half-maximum (FWHM), Γ. Two kinds of normalized line shape functions are usually employed for a general *n*-photon absorption case, either Lorentzian,

$$g_L\left(n\omega,\omega_{0f},\Gamma\right)=\frac{1}{\pi}\frac{\Gamma}{\left(\omega_{0f}-n\omega\right)^2+\Gamma^2}, \tag{1-15}$$

or Gaussian,

$$g_G\left(n\omega,\omega_{0f},\Gamma\right)=\frac{1}{\Gamma\sqrt{2\pi}}\ e^{-\frac{\left(\omega_{0f}-n\omega\right)^2}{2\Gamma^2}}. \tag{1-16}$$

Equation 1-13 yields units of $l.mol^{-1}.cm^{-1}$ for the molar absorptivity when the values of ω are in atomic units and f_{0f} is obtained from μ_{0f} (see Equation 1-14) in atomic units as well.

1.2.2 Two-Photon Absorption

The quantity used to report experimental TPA measurements is the so called two-photon absorption cross section (δ^{TPA}). The theoretical value of δ^{TPA}, for the degenerate case (two photons of equal frequency, $\omega_1=\omega_2=\omega$), can be obtained from the following expression, [30, 57]

$$\delta^{TPA}(\omega)=\frac{1}{30}\frac{(2\pi)^3\omega^2}{c_0^2(4\pi\varepsilon_0)^2}\times\sum_f g\left(2\omega,\omega_{0f},\Gamma\right)\cdot\overline{\delta}_{0f}^{TPA}\left(\omega_{0f}\right), \tag{1-17}$$

$$\delta^{TPA}\left(\omega\right)\approx 8.35150\times10^{-4}\times\omega^2\sum_f g\left(2\omega,\omega_{0f},\Gamma\right)\cdot\overline{\delta}_{0f}^{TPA}\left(\omega_{0f}\right), \tag{1-18}$$

here, the orientationally averaged two-photon probability $\overline{\delta}_{0f}^{TPA}$ is defined in function of the molecular parameters A_1 and A_2,

$$\overline{\delta}_{0f}^{TPA}(\omega_{0f})=F\times\mathsf{A}_1(\omega_{0f})+\left(G+H\right)\times\mathsf{A}_2(\omega_{0f}), \tag{1-19}$$

where *F*, *G*, and *H* are scalars used to define de polarization of the excitation radiation and for the case of linearly polarize light $F = G = H = 2$. [30, 57] The molecular parameters A_1 and A_2 are obtained from the two-photon transition matrix elements S_{ii}^{0f} using,

$$A_1(\omega_{0f}) = \sum_{\rho\sigma} S_{\rho\rho}^{0f}(\omega_{0f}) S_{\sigma\sigma}^{0f,*}(\omega_{0f}), \tag{1-20}$$

$$A_2(\omega_{0f}) = \sum_{\rho\sigma} S_{\rho\sigma}^{0f}(\omega_{0f}) S_{\rho\sigma}^{0f,*}(\omega_{0f}). \tag{1-21}$$

Equation 1-18 yields units of $cm^4.s.photon^{-1}.molecule^{-1}$ (10^{-50} $cm^4.s.photon^{-1}.molecule^{-1}$ = 1 Göppert-Mayer, 1 GM)) for the two-photon absorption cross section when the values of ω and $\overline{\delta}_{0f}^{TPA}$ are in atomic units. In addition, it is important to remark that the OPA and TPA spectra obtained from the theoretical equations presented above only consider single isolated molecules. Next, the main theoretical models for the inclusion of solvent environments are presented.

1.2.3 Solvent models

The solvent effects on the absorption properties of molecular systems were already discussed in Section 1.1. In summary, a solvent environment can potentially modify both the geometry and electronic structure of a chemical species. Excited states are particularly sensitive to perturbations caused by the solvent, due to the increased polarization of charges observed in these states. This behavior can yield to significant changes in the absorption properties of the molecule. Consequently, the application of theoretical models describing solvent effects is highly relevant. Theoretical solvent models can be classified into two major categories, i.e. explicit and implicit models. These two classifications are also commonly referred to as, discrete and continuum models, respectively. [58, 59]

First, explicit solvent models consider some individual solvent molecules interacting with the solute (See Figure 1-2.a). The Supramolecular approach, Molecular Mechanics (MM), Hybrid Quantum Mechanics/Molecular Mechanics (QM/MM) and Molecular Dynamics (MD) are among the explicit models that are widely used for practical applications. The Supramolecular approach describes the solute-solvent interactions in a quantum mechanical way. In the MM approach, classical electrostatic interactions are evaluated considering the charge distribution (point charges, dipoles, etc…) of solute and solvent molecules. The QM/MM method combines a quantum mechanical treatment for one or a few molecules of the solute-solvent ensemble with a molecular mechanical description for the rest of the molecules. The MD approach uses Newton's classical equations of motion to describe the molecular trajectories from theoretically or empirically fitted intramolecular potentials.

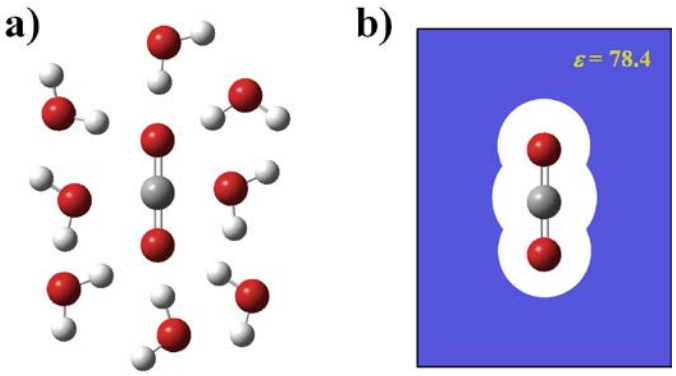

Figure 1-2. Graphical depiction of a) explicit and b) implicit solvent models.

Second, implicit solvent models treat the solvent environment as a polarizable continuum characterized by its dielectric constant ε (See Figure 1-2.b).[59] The solute molecule, which is encapsulated in a cavity surrounded by the continuum medium, is described using a classical electrostatic model or through quantum mechanics. One of the earliest implicit models, the Solvent Reaction Field (SRF) model, was proposed by Onsager in 1936. [60] The SRF model

reduces the solute to a classical point polarizable dipole embedded in a spherical or ellipsoidal cavity within a dielectric continuum. This seminal work served as the basis for the so-called Self-Consistent Reaction Field (SCRF) model. [61] In this approach, the solute molecule is trapped in the same kind of cavity as in the SRF model, but is treated using quantum mechanics. The charge distribution of the solute induces a polarization of the dielectric continuum, generating a new environment that creates changes in the charge distribution of the solute. This cycle repeats itself until an equilibrium condition is achieved. This final state is found through an iterative or self-consistent process. An additional implicit model, that also applies such a self-consistent methodology, is the Polarizable Continuum Model (PCM). [62, 63] The main difference between PCM and SCRF is that the shape of the cavity in the former method resembles that of the solute molecule. Since PCM is the solvent model used throughout this dissertation it will be presented in the next section in more detail.

1.2.3.1 Polarizable Continuum Model

The PCM molecular-shaped cavity is obtained by defining imaginary interlocking spheres centered in each one of the atoms of the solute.[63] The Van der Walls radii, or a slightly increased value of it, are used for defining the sphere size. Using a molecular-shaped cavity instead of a spherical or ellipsoidal one (as in the SRF and SCRF models), allows for a more realistic modeling of the solute. In Figure 1-3, a graphical depiction of the solvent cavity is presented. Two different surfaces are highlighted in this figure, first the cavity surface or Solvent Excluded Surface (SES), that establishes how close the solvent molecules can approach the solute and second the Solvent Accessible Surface (SAS) that is obtained from the addition of the solvent radius to the SES.

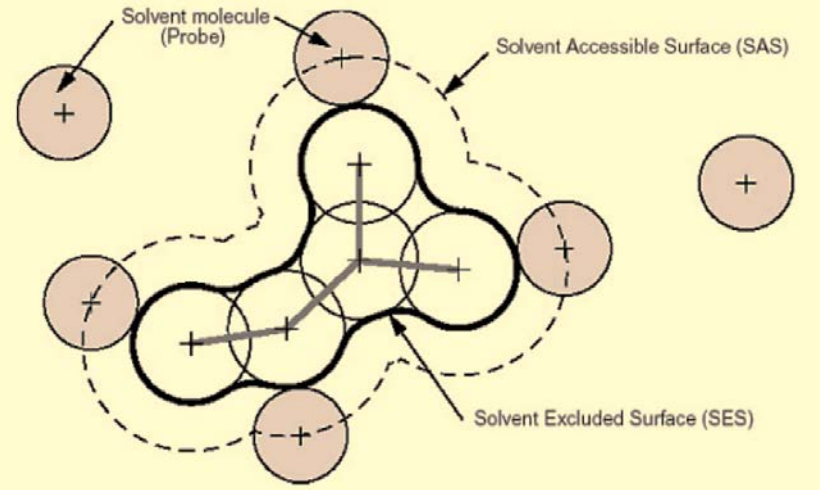

Figure 1-3. Graphical depiction of the PCM cavity (From Ref.63)

In PCM, the solvation free energy (ΔG_{sol}) is calculated using, [64]

$$\Delta G_{sol} = \Delta G_{el} + \Delta G_{dr} + \Delta G_{cav} . \tag{1-22}$$

Here, ΔG_{el} and ΔG_{dr} are the electrostatic and the dispersion-repulsion contributions to the free energy, respectively and ΔG_{cav} is the cavitation energy. The SES is used to calculate ΔG_{el} and ΔG_{cav}, while ΔG_{dr} is obtained from the SAS. In addition, the localization and value of the surface charges are obtained employing a systematic segmentation of the SES in small regions (tesserae) of known areas, where one point charge is considered per surface element.

When PCM is used for the calculation of electronic transitions using time dependent methods, non-equilibrium effects must be included in the model.[63] This modification of the model arises from the fact that upon a sudden change in charge distribution of the solute, due to the incident radiation, the solvent molecules relax in a non-instantaneous fashion. Figure 1-4

shows a graphical representation of an OPA process (red vertical arrow) followed by emission (blue vertical arrow) within the non-equilibrium formulism.

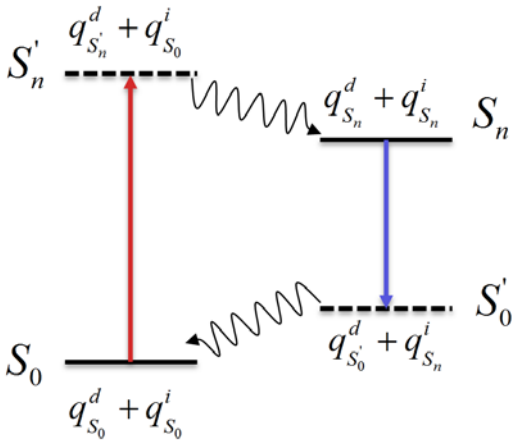

Figure 1-4. Representation of the non-equilibrium formulism

Here, the non-equilibrium effects in PCM have been included by partitioning the reaction field in two components, i.e. one fast and one slow. The fast or dynamic component (q^d) is related to the electronic relaxation and is obtained from the optical or dynamic dielectric constant ε_{opt}, which is given by the square of the refractive index of the solvent. The slow or delayed component (q^i) is calculated from the static dielectric constant ε_{sta}, and is related to the nuclear motions of the solvent molecules.

1.3. Experimental methods for the measurement of two-photon absorption coefficient

Motivated by the many applications of materials with relatively significant third-order susceptibilities,[11, 65] researchers in nonlinear optics have developed several different methods to estimate the TPA coefficients (β) of molecular systems. These methods can be classified in three different categories, i.e. wave mixing techniques, indirect methods and direct methods. [65]

Coherent Anti-Stokes Raman Scattering (CARS), [66, 67] Optical Kerr effect [68, 69] and Degenerate Four-Wave Mixing (DFWM) [70, 71] are among the wave mixing techniques. The former two approaches require the use of two different beams while the latter uses a total of three beams. The experimental setups of these methods are relatively complex because they require a careful control of temporal and spatial overlapping of the beams used. This has limited the use of wave-mixing techniques for practical purposes. [65] In contrast, most indirect methods have the advantage of requiring relatively simple experimental setups. These techniques are based on monitoring the different processes involved in the relaxation of the molecule after the TPA process takes place. The most common indirect method is the so-called Two Photon Induced Fluorescence (TPIF). [72, 73] This technique relies on the availability of an adequate reference compound whose TPA spectrum is known. If this is the case, the TPA spectrum of the sample can be obtained from the direct comparison of its one- and two-photon induced fluorescence spectra with the same spectra for the reference compound, measured under the exact same experimental conditions. The use of this double-referencing methodology eliminates the necessity of knowing several experimental variables, such as parameters related to the excitation beam (pulse duration, pulse energy and temporal intensity distribution), the wavelength dependence of the detector response, the sample concentration or its fluorescence quantum yield. However, one of the main disadvantages of this method is that any uncertainty in the molar absorptivity of the sample will lead to an inaccurate estimation of β. In addition to this, TPIF is limited to samples with detectable fluorescence emission. On the other hand, direct methods do not rely on the emission properties of the molecule under study but rather on its nonlinear absorption. In 1989, Sheik-Bahae *et.al.* [42] introduced the Z-scan technique, which has established itself as the most versatile, simple and widely used direct method for measuring not only β but

the nonlinear refractive indexes (n_2) as well. Next, the basic principles of this approach are presented.

1.3.1 Z-scan technique

A Z-scan consists in the translation of a sample along the propagation axis (*z* axis) of a focused beam with a Gaussian spatial profile and fixed energy. [42] The focusing geometry naturally creates a distribution of intensities along the *z*-axis that is maximum at the focal plane. When the energy of the beam is high enough, variations of the real ($\mathrm{Re}\,\chi^{(3)}$) and imaginary ($\mathrm{Im}\chi^{(3)}$) parts of the third-order susceptibility of the sample can be observed in the vicinity of the focal plane. The magnitude of these changes can be monitored by measuring the transmitted power as a function of the *z* position at the far field, employing two different setups.

In the open aperture setup (see Figure 1-5.a) a collection lens is placed after the sample to ensure that all the transmitted light reaches the far field detector, this variant is used to measure nonlinear absorption (β in the case of TPA). On the other hand, the measurement of nonlinear refraction (n_2) is performed using the closed aperture setup (see Figure 1-5.b), where a circular aperture is placed concentrically with the beam before the far field detector. In both cases, the sample thickness (L) is limited by the confocal parameter of the beam (Raleigh range), z_0, which is a function of the beam radius at the focal plane (w_0) and is defined as $z_0 = \pi w_0^2 / \lambda$ for Gaussian beams. The sample to be scanned has to be "thin" i.e. $L < z_0$, in order to avoid any changes in the beam spatial distribution within the cell, due to the nonlinear diffraction or nonlinear absorption. In addition, a minimum scan length of $\pm 5z_0$ from the focal plane has to be employed to ensure that all the nonlinear behavior is properly measured. In the specific case of the closed aperture Z-scan, the aperture has to be placed at a distance much greater than the Raleigh range (usually between $20z_0$ to $100z_0$) so as to fulfill the far field approximation. A

parameter that is exclusive to the closed aperture Z-scan is the so-called transmittance factor of the aperture (S), which is determined by the fraction of the transmitted beam that passes through the aperture. Typical values for S are between 0.1 and 0.5. Here, it is important to emphasize that the beam distortions associated to nonlinear refraction can only be detected when at least a fraction of the light ($0 < S < 1$) is cut by the aperture.

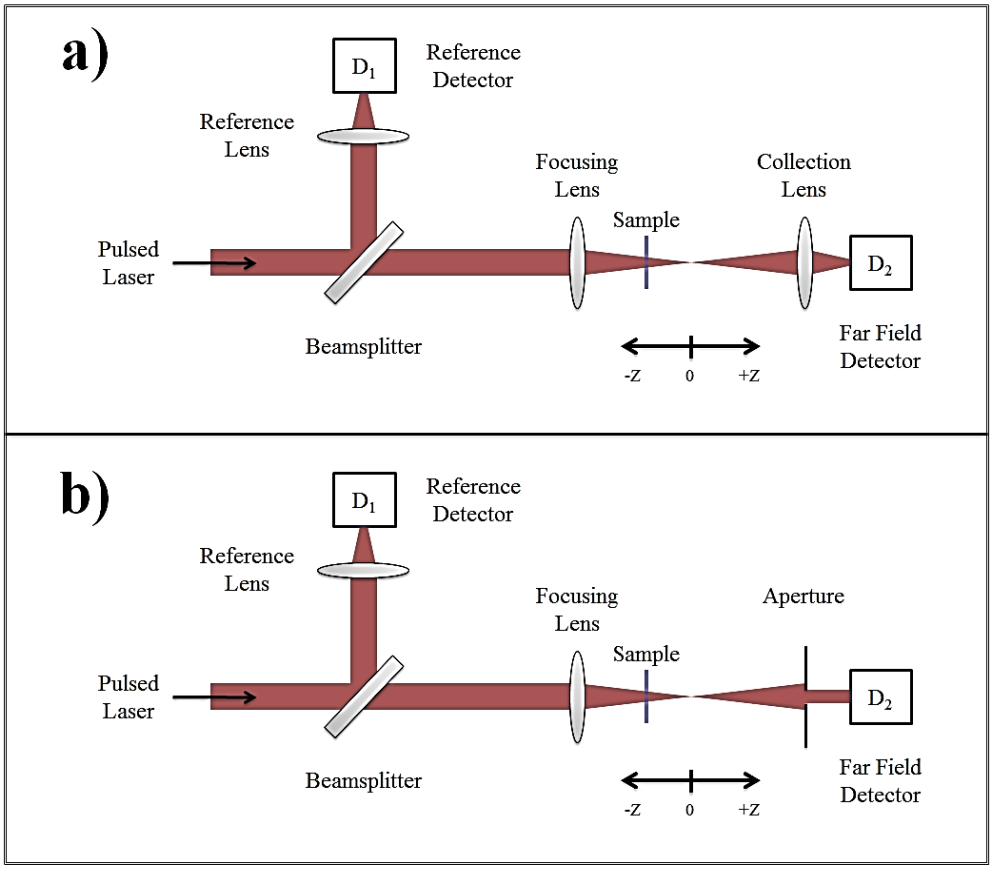

Figure 1-5. (a) Closed aperture Z-scan setup. **(b)** Open aperture Z-scan setup.

The typical outputs for the closed aperture Z-scan of a sample exhibiting nonlinear refraction (without any nonlinear absorption) are shown in Figure 1-6.a. The two curves correspond to self-focusing ($n_2 > 0$, red line) and self-defocusing ($n_2 < 0$, black line) nonlinearities. In the former case, as the sample approaches the focal plane, the beam size

increases and a transmittance minimum is observed, once the sample passes the focal plane the beam size decreases and the additional light that goes through the aperture generates a transmittance maximum. In the latter case, the opposite behavior is registered. A common feature of both cases is that the transmittance at the focal plane is identical to the far field transmittance. This behavior is a direct result of the "thin lens" approximation. The magnitude of n_2 can be approximately determined from,

$$|n_2| = \left(\frac{\lambda}{2\pi}\right)\frac{|\Delta\Phi_0|}{I_0 L}, \tag{1-23}$$

where, I_0 is the irradiance at the focal point and $|\Delta\Phi_0|$ is the absolute value of the nonlinear phase shift, which is given by,

$$|\Delta\Phi_0| = \frac{\Delta T_{pv}}{0.406(1-S)^{0.25}}, \tag{1-24}$$

here ΔT_{pv} is the value of the difference between the peak and valley transmittances. An additional useful application of the closed aperture Z-scan is in the estimation of the Raleigh range through the empirical relationship $\Delta Z_{pv} \sim 1.7 z_0$, where ΔZ_{pv} is the difference between the Z positions of the peak and the valley.

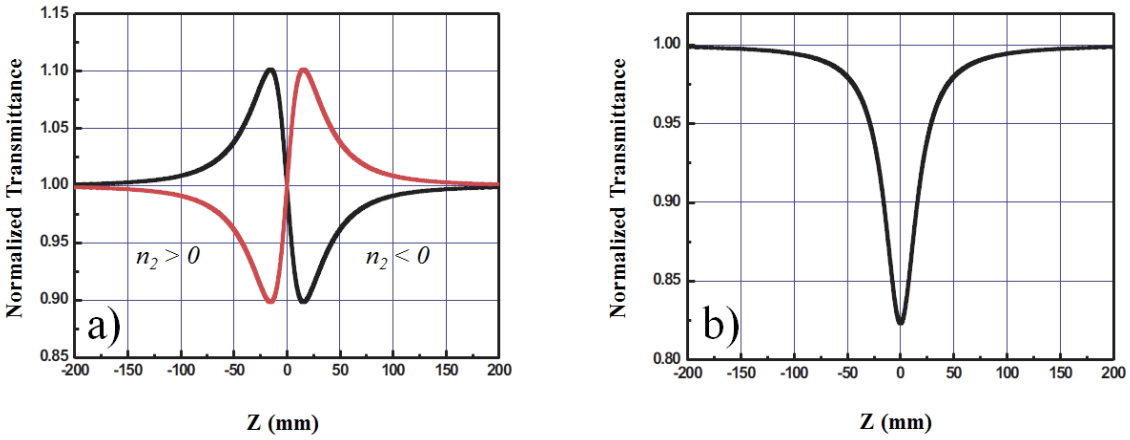

Figure 1-6. Typical outputs for **(a)** Closed aperture z-scan and **(b)** Open aperture Z-scan.

Figure 1-6.b shows the typical output of an open aperture Z-scan of a sample exhibiting nonlinear absorption. The removal of the aperture in this experiment is crucial to avoid any interferences coming from changes in the wavefront of the beam due to nonlinear refraction. The collection of all the transmitted light ensures that any decrease in transmittance is due to nonlinear absorption of the sample. Far from the focal plane, the size of the Gaussian beam is not small enough to attain the intensity required to induce nonlinear absorption on the sample. Therefore, the Normalized Transmittance (NT) can be set equal to unity using this point as a reference. As the sample continues its way towards the focal plane of the focused Gaussian beam ($z = 0$), the nonlinear absorption starts to occur and NT decreases. The minimum NT is observed at the focal point, where the maximum nonlinear absorption takes place. Then the sample is moved away from the focal plane and the decreased intensity of the beam allows NT to reach its original base value. The magnitude of β can be indirectly determined from the open aperture Z-scan curve using the following relationship,

$$T(z) = \frac{1}{\sqrt{\pi} \cdot q_0} \int_{-\infty}^{+\infty} \ln\left(1 + q_0 e^{-t^2}\right) dt, \tag{1-25}$$

where the temporally Gaussian pulse is time integrated to give NT and $q_0 = I_0 \beta L w_0^2 / w^2(z)$. Here, I_0 is related to the intensity at the focal plane and $w(z)$ is the beam radius at a given z position.

The linear and nonlinear optical phenomena described up to this point are applicable to any molecular system. However, in chiral molecules additional optical properties are observed. These properties are at the core of this dissertation and understanding them is crucial for the comprehension of this work. Next, the fundamentals of the absorption properties of chiral molecules are presented.

1.4. Fundamentals of linear and nonlinear circular dichroism

Chiral systems are those whose mirror images are not superimposable. [74] This group of molecules exhibit specific optical properties, both in the linear and nonlinear regime. Such properties are called chiroptical, and their occurrence is strictly bound to the polarization state of the light used to induce them. Therefore, before considering the different chiroptical properties it is important to revise the fundamentals of polarized light.

When the orientation of the electric field of a light wave is constant in time, such wave is said to be linearly polarized. In order to understand the origin of the different polarization states of light, it is necessary to first analyze the case of two orthogonal linearly polarized waves propagating in time (t) along the z axis. [75] In this case the electric field vector ($\vec{E}_i$) of the two waves can be described by,

$$\vec{E}_x(z,t) = \hat{i}E_{0x}\cos(kz - \omega t), \tag{1-26}$$

and

$$\vec{E}_y(z,t) = \hat{j}E_{0y}\cos(kz - \omega t + \varphi), \tag{1-27}$$

where k is the light wave vector, ω is the frequency of the light, φ is the relative phase difference between them, and E_{0x} and E_{0y} are the amplitude of the electric field in the x and y direction, respectively. The linear combination of these two waves yields,

$$\vec{E}(z,t) = \vec{E}_x(z,t) + \vec{E}_y(z,t). \tag{1-28}$$

If the two waves are in phase, i.e. $\varphi = \pm n\pi$, where $n = 0, 1, 2, 3\ldots$, $\vec{E}(z,t)$ can be written as,

$$\vec{E}(z,t) = \left(\hat{i}E_{0x} + \hat{j}E_{0y}\right)\cos(kz - \omega t), \tag{1-29}$$

where this resultant wave has a constant amplitude in time equal to $\left(\hat{i}E_{0x} + \hat{j}E_{0y}\right)$ that makes it linearly polarized also.

However, the linear combination of two linearly polarized waves does not always yield linearly polarized light. For instance, if the two waves have identical amplitude $E_{0x} = E_{0y} = E_0$, and $\varphi = (-\pi/2) + (2m\pi)$, where $m = \pm 1, \pm 2, \ldots$, the resultant quarter-wave phase difference changes the behavior of $\vec{E}_y(z,t)$ from cosinusoidal to sinusoidal, and then the linear combination of the two waves is given by,

$$\vec{E} = E_0\left[\hat{\mathrm{i}}\cos(kz - \omega t) + \hat{\mathrm{j}}\sin(kz - \omega t)\right], \tag{1-30}$$

where the amplitude of the electric field is constant but its direction rotates continuously in time around the *z* axis, resulting in circularly polarized light. The direction of the rotation is determined by the sign of the quarter-wave phase difference. The wave described by Equation 1-30 rotates in a clockwise direction, as seen by an observer towards whom the wave is propagating. In this case the light is said to be Right Circularly Polarized. On the other hand, if the phase difference is $\varphi = (\pi/2) + (2m\pi)$, the same observer will perceive the wave rotating counterclockwise, which corresponds to Left Circularly Polarized Light that is described by $\vec{E} = E_0\left[\hat{\mathrm{i}}\cos(kz-\omega t) - \hat{\mathrm{j}}\sin(kz-\omega t)\right]$. If left and right circularly polarized light of the same amplitude are mixed, the resulting wave will have linear polarization because of the cancelation of the $\vec{E}_y(z,t)$ components of the mixed waves. Therefore, linearly polarized light can be seen as a combination of circularly polarized light of both handedness. [75]

1.4.1 Electronic Circular dichroism

When a beam of linearly polarized light passes through a chiral sample, its circularly polarized components exhibit different refractive indexes $(n_L \neq n_R)$ and can have different absorption coefficients $(k_L \neq k_R)$. The occurrence of this behavior gives rise to two different chiroptical phenomena, circular birefringence and circular dichroism.[76] The former effect, also known as optical rotation, induces the rotation of the plane of polarization of linearly polarized light as the beam passes through the chiral sample. The latter chiroptical phenomenon manifests in the preferential absorption of one circularly polarized light over the other.

In order to better understand the chiroptical phenomenon of circular dichroism it is necessary to analyze the behavior of linearly polarized light as it is absorbed by a chiral medium. Before the linearly polarized light passes through a chiral sample (See Figure 1-7.a), its two circularly polarized components have electric field vectors of the same magnitude. After passing through the chiral sample both vectors have decreased in magnitude, due to absorption (See Figure 1-7.b). However, as a result of circular dichroism, the magnitude of the electric field of one of the two circularly polarized components decreased more than the other ($E_L < E_R$ in the case of Figure 1-7.b). Therefore, the polarization of the transmitted light is no longer linear but elliptical. [74]

The degree of ellipticity (θ) is obtained from the arctangent of the minor to the major elliptical axis (See Figure 1-7.b). The value of θ (in degrees) is related to the differences in absorption of circularly polarized light through the following relationship, [77]

$$\theta = 32.988\Delta A\,, \tag{1-31}$$

where $\Delta A = A_L - A_R$ is the circular dichroism, here A_L and A_R are the absorbance for left and right circularly polarized light, respectively. An expression for molar ellipticity $([\theta])$ can be obtained after combining Equation 1-31 with Beer's law, [77]

$$[\theta] = \frac{\theta}{c \cdot l} = \frac{32.988\Delta A}{c \cdot l} = 32.988\Delta\varepsilon\,, \tag{1-32}$$

where, c is the molarity, l is the path length in centimeters, $\Delta\varepsilon$ is the circular dichroism in terms of molar absorptivity. Experimental measurements of circular dichroism are usually reported in terms of $[\theta]$ or $\Delta\varepsilon$.

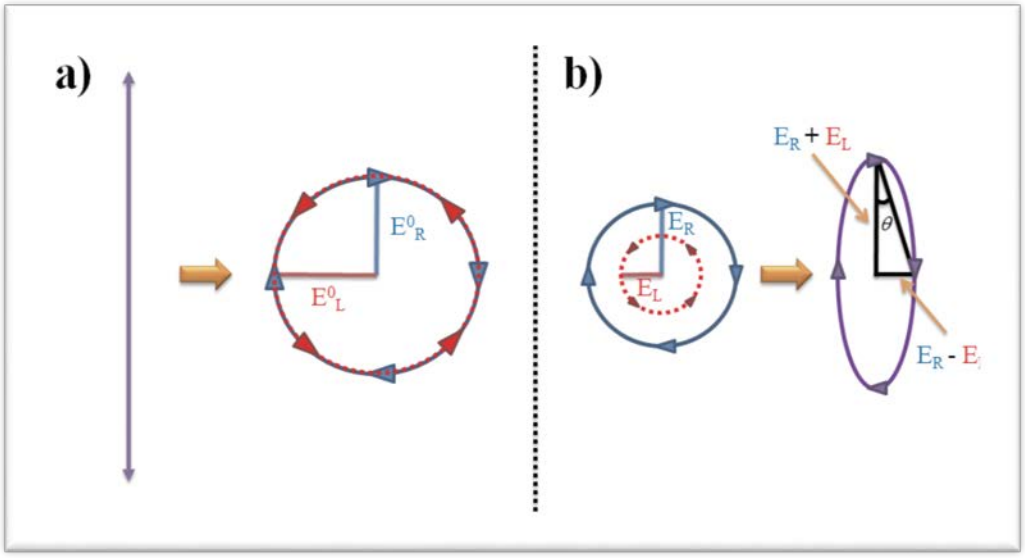

Figure 1-7. (a) Linearly polarized light (vertical double headed arrow) can be described by a left (circle with red arrowheads) and right (circle with blue arrowheads) circularly polarized components with electric fields of the same magnitude ($E^0_R = E^0_L$). **(b)** After interacting with a chiral medium, both components are unequally absorbed (concentric circles) and their sum describes an elliptical polarization state (purple ovoid). Note: The four diagrams depicted in the Figure show a complete oscillation (2π) of the electric field vectors from the point of view of an observer who is in front of the propagation axis.

When referred to electronic excitations (OPA), circular dichroism is known as electronic circular dichroism (ECD). ECD is widely used on the assignment of absolute configurations, because the enantiomers of a chiral molecule, i.e. the pair molecules with non-superimposable mirror images, yield mirror image ECD spectra (opposite sign for each excitation wavelength). [28] In addition, ECD is sensitive to conformational and structural changes affecting the 3D structure of chiral molecules, thus establishing this spectroscopic tool among the most powerful methods for stereochemical analysis. However, for electronic excited states that correspond to excitation wavelengths of less than 200 nm, ECD measurements are hindered by the increased linear absorption of solvents and buffers in this region, as well as by the increased scattering observed in inhomogenous samples. [29] In order to overcome these limitations, approaches such as synchrotron radiation circular dichroism (SRCD), [78] magnetic circular dichroism (MCD), [79]

vibrational circular dichroism (VCD), [80] and Raman optical activity (ROA), [81] have been proposed. However, none of these methods have been able to successfully reveal the spectral features located in the near to far UV region that are obscure to ECD. The only experimental approach that has shown the potential to achieve this goal and it is also a truly polarization dependent method (like ECD), is the so-called Two-Photon Circular Dichroism (TPCD)

1.4.2 Two-Photon Circular Dichroism

TPCD is defined as $\Delta\delta^{TPCD}(\lambda) = \delta_L^{TPA}(\lambda) - \delta_R^{TPA}(\lambda)$, where $\delta_L^{TPA}(\lambda)$ and $\delta_R^{TPA}(\lambda)$ are the TPA cross-section for left and right circularly polarized light, respectively. [30, 31] In other words, TPCD is the nonlinear equivalent of ECD (See Figure 1-8) and consists on the differences in TPA cross-section observed when chiral molecules are excited with circularly polarized light of different handedness. This approach combines the chiral discrimination capabilities of circular dichroism with the many advantages described in Section 1.3 for TPA based techniques, thus giving TPCD the potential to overcome the shortcomings of ECD at lower wavelengths. In addition, the different selection rules that govern OPA and TPA processes (see Section 1.2), suggest that ECD and TPCD should have different spectral features. However, since selection rules are relaxed in chiral molecules due to their inherent lack of symmetry, these differences are not as marked as the differences observed between OPA and TPA of centrosymmetric molecules. In spite of this, TPCD has proven to provide spectroscopic information for chiral molecules that is complementary to that found employing ECD. [82]

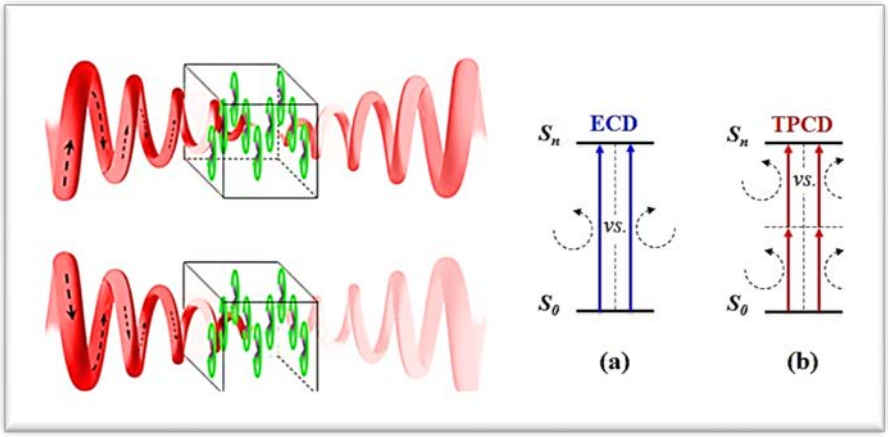

Figure 1-8. Comparative representation of **(a)** Electronic circular dichroism and **(b)** Two-photon circular dichroism.

1.5. Theoretical framework for the calculation of linear and nonlinear circular dichroism spectra

1.5.1 Electronic Circular Dichroism

As mentioned in Section 4.1, experimental ECD spectra are usually reported as differences in molar absorptivity $\left(\Delta\varepsilon^{ECD}\right)$. This quantity is proportional to the ECD rotatory strength $\left(R_{0f}^{ECD}\right)$ of each electronic excited state which in turn depends on the electric $\left(\boldsymbol{\mu}\right)$ and magnetic $\left(\mathbf{m}\right)$ transition dipole moments. For an electronic transition between the ground state and an excited state, the following equation establishes the relationship between R_{0f}^{ECD} and the molar absorptivity $\Delta\varepsilon^{ECD}\left(\omega\right)$, [30, 56, 83]

$$\Delta\varepsilon^{ECD}\left(\omega\right)=\varepsilon_L\left(\omega\right)-\varepsilon_R\left(\omega\right)=\frac{64\pi^2 N_A\omega}{9\times1000\times\ln\left(10\right)\times\left(4\pi\varepsilon_0\right)\times\hbar c_0^2}\sum_f g\left(\omega,\omega_{0f},\Gamma\right)R_{0f}^{ECD}, \tag{1-33}$$

$$\Delta\varepsilon^{ECD}\left(\omega\right)\approx 2.73719\times10^1\times\omega\sum_f g\left(\omega,\omega_{0f},\Gamma\right)\cdot R_{0f}^{ECD}, \tag{1-34}$$

where $\omega = 2\pi c_0/\lambda$ is the circular frequency of the incident radiation, c_0 is the speed of light in *vacuo*), ε_0 is the vacuum permittivity, N_A is Avogadro's number, $g\left(\omega, \omega_{0f}, \Gamma\right)$ is the normalized lineshape centered at $\omega = \omega_{0f}$ and with a full width half-maximum (FWHM), Γ (see Equations 1-15 and 1-16 for a full description of the lineshapes employed) and R_{0f}^{ECD} is calculated from,[38, 83]

$$R_{0f}^{ECD} = \frac{3}{4}\Im\left[\langle 0|\boldsymbol{\mu}|f\rangle\langle f|\mathbf{m}|0\rangle\right], \tag{1-35}$$

where the gauge length is employed. Equation 1-34 implies that R_{0f}^{ECD} is used in a.u. and then the units of $\Delta\varepsilon^{ECD}$ are $mol^{-1}cm^{-1}L$.

1.5.2 Two-Photon Circular Dichroism

Tinoco [30] and Power, [31] simultaneously but independently, were the first to predict the theoretical possibility of TPCD in 1975. However, the computational implementation of their predictions was not performed until three decades later, when Rizzo and co-workers made possible the calculation of TPCD for complex molecular systems. According to the formalism proposed by Tinoco [30] the TPCD spectrum of a chiral molecule can be obtained from the TPCD rotatory strength $\left(R_{0f}^{TPCD}\right)$ through the following relationship, [56]

$$\Delta\delta^{TPCD}\left(\omega\right) = \delta_L^{TPA}\left(\lambda\right) - \delta_R^{TPA}\left(\lambda\right) = \frac{4}{15}\frac{(2\pi)^3\omega^2}{c_0^3(4\pi\varepsilon_0)^2} \times \sum_f g\left(2\omega, \omega_{0f}, \Gamma\right) \cdot R_{0f}^{TPCD}\left(\omega_{0f}\right), \tag{1-36}$$

$$\Delta\delta^{TPCD}\left(\omega\right) \approx 4.87555x10^{-5} \times \omega^2 \sum_f g\left(2\omega, \omega_{0f}, \Gamma\right) \cdot R_{0f}^{TPCD}\left(\omega_{0f}\right), \tag{1-37}$$

where $R_{0f}^{TPCD}\left(\omega_{0f}\right)$ is obtained from,

$$R_{0f}^{TPCD}\left(\omega_{0f}\right) = -b_1 \mathsf{B}_1(\omega_{0f}) - b_2 \mathsf{B}_2(\omega_{0f}) - b_3 \mathsf{B}_3(\omega_{0f}), \tag{1-38}$$

here b_1, b_2 and b_3 are scalars that depend on the experiment. In the case of two co-linear and co-propagating right or left circularly polarized photons, b_1 = 6 and b_2 = -b_3 = 2. The molecular parameters $\mathsf{B}_i(\omega_{0f})$ can be obtained from, [82]

$$\mathsf{B}_1^{TI}(\omega_{0f}) = \frac{1}{\omega_{0f}^3} \sum_{\rho\sigma} \mathsf{M}_{\rho\sigma}^{p,0f}(\omega_{0f}) \mathsf{P}_{\rho\sigma}^{p*,0f}(\omega_{0f}), \tag{1-39}$$

$$\mathsf{B}_2^{TI}(\omega_{0f}) = \frac{1}{2\omega_{0f}^3} \sum_{\rho\sigma} \mathsf{T}_{\rho\sigma}^{+,0f}(\omega_{0f}) \mathsf{P}_{\rho\sigma}^{p*,0f}(\omega_{0f}), \tag{1-40}$$

$$\mathsf{B}_3^{TI}(\omega_{0f}) = \frac{1}{\omega_{0f}^3} \left[\sum_{\rho} \mathsf{M}_{\rho\rho}^{p,0f}(\omega_{0f}) \right] \left[\sum_{\sigma} \mathsf{P}_{\sigma\sigma}^{p*,0f}(\omega_{0f}) \right], \tag{1-41}$$

where $\mathsf{P}_{\alpha\beta}^{p*,0f}(\omega_\beta)$ and $\mathsf{T}_{ii}^{+,0f}$ are the electric transition dipole and quadrupole matrix elements in the velocity formulation, respectively, and $\mathsf{M}_{\alpha\beta}^{p,0f}(\omega_\beta)$ is the magnetic transition dipole matrix element. These tensors are defined through the following sum-over state expressions:

$$\mathsf{P}_{\alpha\beta}^{p*,0f}(\omega_\beta) = \frac{1}{\hbar} \sum_P \sum_{n\neq 0} \frac{\left(\mu_\alpha^p\right)^{0n} \left(\mu_\beta^p\right)^{nf}}{\omega_\alpha - \omega_{0n}}, \tag{1-42}$$

$$\mathsf{M}_{\alpha\beta}^{p,0f}(\omega_\beta) = \frac{1}{\hbar} \sum_P \sum_{n\neq 0} \frac{\left(\mu_\alpha^p\right)^{0n} \left(m_\beta^p\right)^{nf}}{\omega_\alpha - \omega_{0n}}, \tag{1-43}$$

$$\mathsf{T}_{\alpha\beta}^{+,0f}(\omega_\beta) = \frac{1}{\hbar} \varepsilon_{\beta\rho\alpha} \sum_P \sum_{n\neq 0} \frac{\left(T_{\alpha\rho}^{+}\right)^{0n} \left(\mu_\sigma^p\right)^{nf}}{\omega_\alpha - \omega_{0n}}, \tag{1-44}$$

where $\varepsilon_{\beta\rho\alpha}$ is the Levi Civita alternating tensor, μ_α^p is the α component of the dipole velocity operator, given by,

$$\mu_{\alpha}^{p} = \sum_{i} \frac{q_i}{m_i} p_{i\alpha} \,, \tag{1-45}$$

m_{β}^{p} is the magnetic dipole operator:

$$m_{\beta}^{p} = \sum_{i} \frac{q_i}{2m_i} \left(r_i \times p_i \right)_{\beta} \,, \tag{1-46}$$

and the $\alpha\beta$ component of the mixed length-velocity form of the quadrupole operator $T_{\alpha\rho}^{+}$, is defined as

$$T_{\alpha\rho}^{+} = \sum_{i} \frac{q_i}{m_i} \left(p_{i\alpha} r_{i\beta} + r_{i\alpha} p_{i\beta} \right). \tag{1-47}$$

Equation 1-37 yields units of *cm*^{4}*.s.photon*$^{-1}$*.molecule*$^{-1}$ (10^{-50} *cm*^{4}*.s.photon*$^{-1}$*.molecule*$^{-1}$ = 1 Göppert-Mayer, 1 GM)) for the TPCD when the values of ω and $R_{0f}^{TPCD}\left(\omega_{0f}\right)$ are in atomic units.

It is interesting to highlight that Tinoco [30] and Power [31] also addressed the feasibility of experimental measurements of TPCD. Both authors showed in their remarks that the ratio of the TPCD to TPA signals would be similar to that found between ECD and OPA signals, which is usually in the order of 10^{-3}. This led them to conclude that TPCD would be experimentally undetectable. In spite of this prediction, experimentalists in nonlinear optics have made efforts to overcome this limitation. However, it was not until recently that a reliable and versatile technique for the measurement of TPCD was developed. The next section addresses the fundamentals of this experimental approach.

1.6. Experimental measurements of two-photon circular dichroism

The earliest successful attempt for the measurement of TPCD is attributed to Gunde and Richardson, [33] who in 1995 observed TPCD on a Gd^{3+} complex using fluorescence based method called Fluorescence Detected TPCD (FD-TPCD). However, only a very limited portion of the TPCD spectrum (approximately 23 nm) was measured. Due to the lack of versatility of this experimental approach, the quest for different methods for measuring TPCD continued. Experiments employing pump-probe, [18] Z-scan with modulation of the polarization, [84] resonance-enhanced multiphoton ionization [85, 86] have been attempted. Unfortunately, none of these approaches have been capable of yielding pure TPCD spectra of any optically active molecule.

The challenge at hand was not solved until the introduction of a novel experimental approach in 2008 by Hernandez and co-workers called the double-L scan. [34] This method was based on the Z-scan technique and had the necessary sensitivity to allow for the detection of TPCD. The experimental strategy behind this improved sensitivity is that the TPA measurements for the different polarization states are carried out simultaneously using "twin pulses". Because all the experimental TPCD measurements presented in this dissertation were performed using the double-L scan, the details of this experimental approach are presented in the following section.

1.6.1 Double-L scan

The first attempts of Hernandez and co-workers to measure TPCD [87] were performed using the Z-scan technique. The approach consisted in measuring the TPA cross-sections for right circularly polarized light (RCPL) and left circularly polarized light (LCPL), as well as Linearly Polarized Light (LPL). Apart from the polarization state of the light, all the

experimental conditions for these measurements were kept constant within the experimental limitations. (S)-(-)-1,1'-bi(2-naphthol) (S-BINOL) and (R)-(+)-1,1'-bi(2-naphthol) (R-BINOL) in THF solution, were the two enantiomers employed in the study. The enantiomeric ratio for both compounds was ≥ 99:1. The excitation source consisted of an Optical Parametric Generator (OPG) pumped by the third harmonic of a mode locked Nd:YAG laser (EKSPLA). The whole system was capable of generating pulses of 25 ps (FWHM) at a 10 Hz repetition rate and with an energy stability of <30%.

Because of the instability of the laser source, the experiments were performed employing a very small energy window (± 2%) and hundreds of pulses were averaged at each *z* position. The use of these extreme experimental conditions was thought to allow for the observation of the small differences in TPA cross-section between the different circular polarization states (TPCD). Nevertheless, the RCPL and LCPL TPA spectra of both enantiomers showed no differences within the experimental error. Surprisingly, the error of the TPA measurements was greater than the selected 2% energy window. (See Figure 1-9 for the TPA spectra of R-BINOL, similar results were observed for S-BINOL)

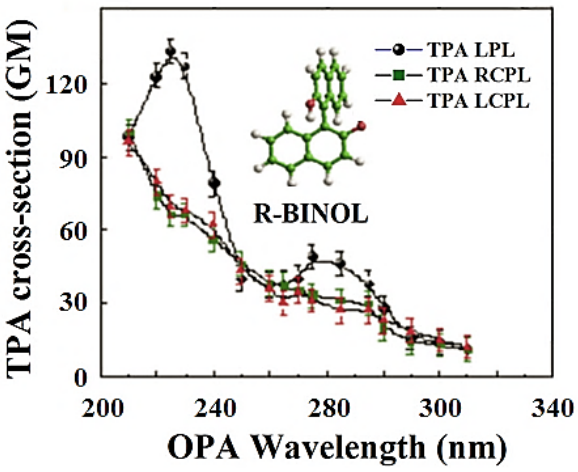

Figure 1-9. Z-scan TPA spectra of R-BINOL in THF, pumping with LPL (black spheres), RCPL (green squares) and LCPL (red triangles) plotted at the half the excitation wavelength.

In light of this outcome, they proposed the following hypothesis: *Common changes observed in the beam size and shape, and even modal fluctuations can lead to significant changes in the spatial energy distribution that could create changes in irradiance for the different z positions, thus increasing the error of the measurement. This artifact can mask the TPCD signal.*

In order to prove the proposed hypothesis, Hernandez and co-workers [87] captured the beam profile for a series of pulses using a CCD camera. Figure 1-10 shows the snapshots of a sequence of eight different pulses that were used in a typical Z-scan. It is evident from the pictures that there were significant differences in the spatial profile, energy distribution and size of the different pulses.

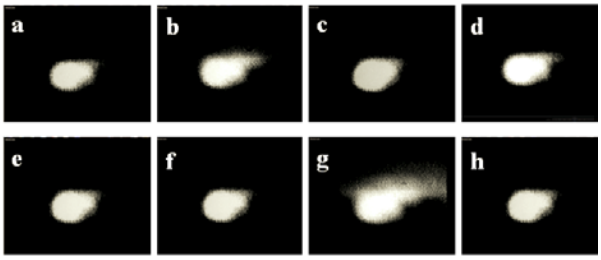

Figure 1-10. Snapshot of a sequence of eight laser pulses used in a Z-scan.

The approach, that Hernandez and co-workers proposed in order to avoid the artifact generated by these fluctuations, consisted in the simultaneous measurement of $\delta_L^{TPA}(\lambda)$ and $\delta_R^{TPA}(\lambda)$ using a double arm setup at 90°. This variation from a standard Z-scan required the sample to be held at a fixed position, in order to be able to scan the focal plane along the z-axis of both arms in a simultaneous fashion. Therefore, the scan was performed moving the focuses of the two beams by translating the lenses of both arms along the z-axis. For this reason the method was named double-L scan.

The main principle of the double-L scan approach can be explained using Figure 1-11.

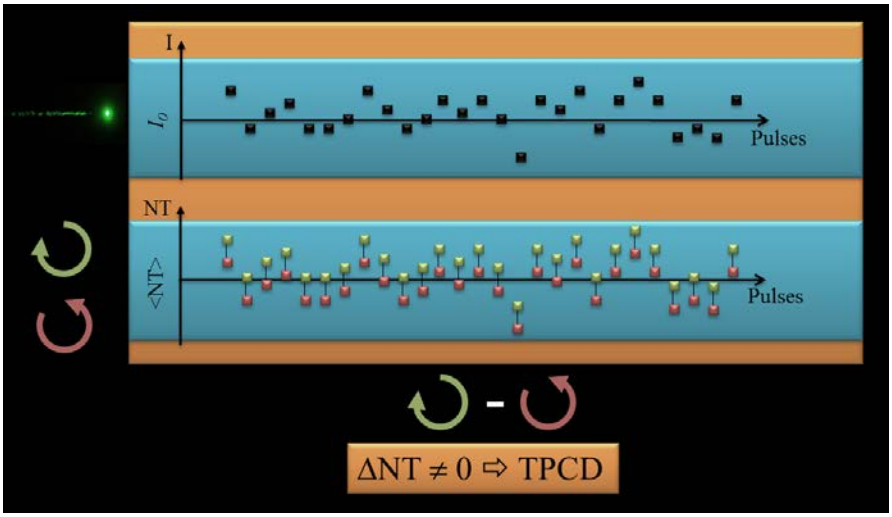

Figure 1-11. Graphical representation of TPA measurements performed using the double-L scan technique. Excitation is carried out using pulses with RCPL (green squares) and LCPL (red squres). The top drawing displays the Intensity (I) of different laser pulses and the bottom drawing shows the normalized transmittance (NT) of the sample for each pulse for both circular polarization states.

Here, a seed beam is used to create two identical or "twin beams" that will induce the TPA excitation using different circular polarization states. The two beams pass through virtually identical optical elements and travel the same paths, which is a guarantee that any spatial fluctuations in the laser pulses will be equally experienced in both arms. This implies that if pulse *i* impinges the sample with an irradiance that is higher than the preselected average value (I_0), due for instance to a size change on the beam, the signal on both arms will increase in an identical fashion. Conversely, if pulse *i'* creates an irradiance lower than I_0 when it hits the sample, the observed signal will decrease equally in both arms. As a result, any difference between the two measurements shall always be observed ($\Delta NT \neq 0$) and it will retain its sign. Therefore, the value of ΔNT obtained from the averaging of the different pulses is bound to exclusively occur due to TPCD.

The double-L scan setup is depicted in Figure 1-12. [34] Here, the same EKSPLA system used in the Z-scan experiments was used as the excitation source. It is clear from this diagram that the two arms of the double-L scan (after BS2 up until D2 and D3) have identical optical elements and paths.

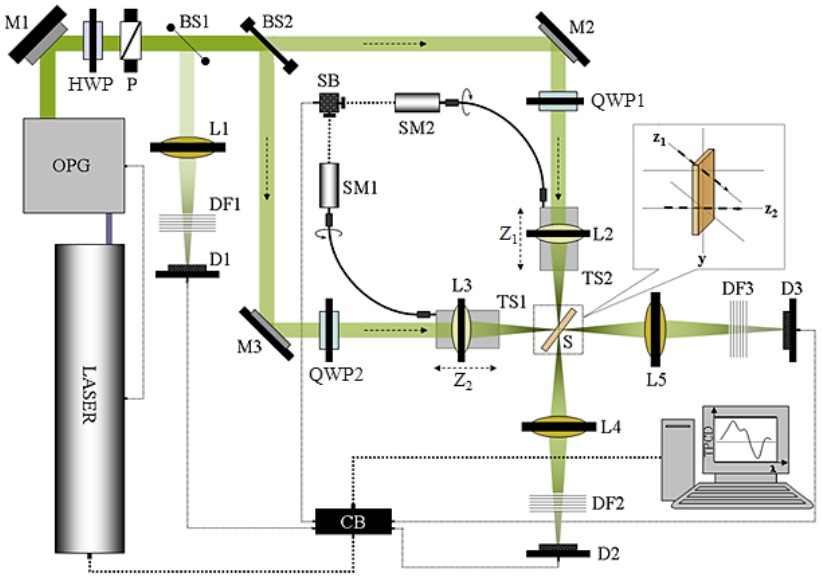

Figure 1-12. Double L-Scan setup. Mirrors (M1, M2, M3); half wave plate (HWP); quarter wave plates (QWP1, QWP2); polarizer (P); beam splitters (BS1, BS2); convergent lenses (L1, L2, L3, L4, L5); detectors (D1, D2, D3); neutral density filters (DF1, DF2, DF3); translation stages (TS1, TS2); step-motors (SM1, SM2); synchronization box (SB); sample (S), and control box (CB)

With the aim of confirming the effectiveness of the double-L scan setup for the creation of "twin beams", another capture of pulse profiles was performed with a CCD camera. The snapshots of the two pulses were taken right before they encounter the sample, by placing the CCD camera at 45° angle from both beams.

Figure 1-13 shows a sequence of twelve snapshots of the pair of pulses. Here it is relevant to highlight that the small, difference in size observed within a pair of pulses for all the snapshots is due to the positioning of the CCD camera and not to differences arising from the

experiment. Apart from this, there are no additional differences observed between pulses in a snapshot. Therefore, the double-L scan setup indeed compensates for any temporal or spatial fluctuations experienced by the laser source, thus allowing for the detection of the small TPCD signal.

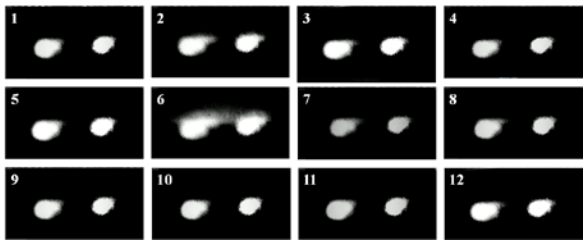

Figure 1-13. Snapshot of a sequence of twelve pairs of laser pulses used in a double L-scan. The small difference in size within a pair of pulses is due to the angle used to take the snapshots with the CCD camera.

A necessary requirement to be able to perform TPCD measurements using the double-L scan setup is that the experimental conditions on both arms have to be identical. This creates the need for a calibration of the setup prior to the actual polarization dependent measurement. The calibration procedure consists in performing the measurement of the TPA of the sample under study, using LPL on both arms. Only when the energy in both arms is identical, ΔNT would be equal to zero and the double-L scan is considered to be calibrated. Once this condition is achieved, the TPCD measurement can be performed by changing the polarization state of the two arms to RCPL and LCPL, respectively. This is achieved by a 45° rotation of the extraordinary axis of the corresponding quarter waveplate on each arm (QWP1 and QWP2 in Figure 1-13) with respect to the plane of polarization of the incident light.

Then, employing the protocol described above for the double-L scan, a new attempt to measure the TPCD spectrum of R- BINOL in THF was carried out. Figure 1-14 shows the experimental TPA spectrum of R-BINOL in THF using LPL, RCPL and LCPL, in addition to the

OPA spectrum. All the spectra are plotted using the OPA wavelength (half the TPA excitation wavelength), in order to facilitate their comparison. Under this experimental conditions, the percent error of the TPA measurements was significantly reduced (<1%).

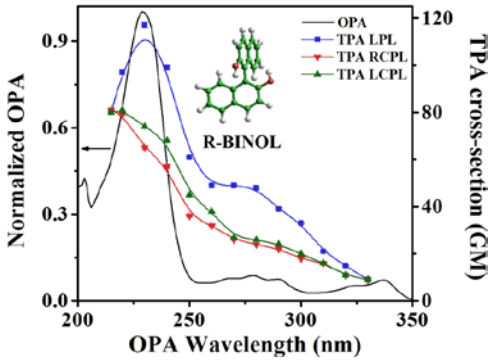

Figure 1-14. Double-L scan TPA spectra of R-BINOL in THF, pumping with LPL (black spheres), RCPL (green squares) and LCPL (red triangles) plotted at the half the excitation wavelength. The normalized OPA spectrum is also shown (solid black line).

The most noticeable feature of Figure 1-14 is the difference in magnitude and shape between the TPA spectra measured using LPL and those taken using RCPL and LCPL (also observed for the Z-scan casa in Figure 1-9). This is due to a phenomenon called Two-Photon Circular Linear Dichroism (TPCLD) [88] that is out of the scope of this dissertation. The second, but most relevant observation, are the appreciable differences between $\delta_L^{TPA}(\lambda)$ and $\delta_R^{TPA}(\lambda)$ across the spectrum. From this data the experimental TPCD spectrum of R-BINOL was obtained (See Figure 1-15.a). The spectrum yielded a positive signal for most of the measured spectral range, with a negative signal observed only at 216 nm. The spectrum of S-BINOL was also obtained after polarization dependent measurements employing the double-L scan (See Figure 1-15.a). [35] Remarkably, the TPCD spectrum of both enantiomers are mirror images of each other, which is the expected behavior. In addition, the experimental TPCD was also measured for a racemic mixture of BINOL (50 % R-BINOL and 50 % S-BINOL). This resulted in a constant

value of 0 ± 1 GM for the entire spectrum, thus confirming that the origin of the TPCD signal was tied to the pure enantiomers. Next, in order to obtain the theoretical TPCD spectra, the structures of both BINOL enantiomers were optimized using Density Functional Theory (DFT) [48] at the B3LYP [51-53]/6-31++G(d,p) [89, 90] level of theory, followed by the time dependent DFT (TD-DFT) [48] calculations of the $R_{0f}^{TPCD}\left(\omega_{0f}\right)$ for the first 25 electronic excited states at the B3LYP/aug-cc-pVDZ [91] level of theory, considering solvent effects (THF) under the polarizable continuum model (PCM). [63] The geometry optimizations were performed in Gaussian 03, [92] while the TD-DFT calculations were carried out in DALTON 2.0. [93]

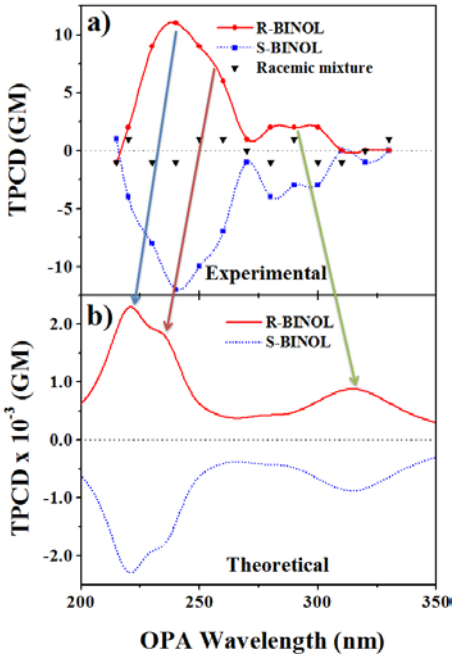

Figure 1-15. (a) Experimental and **(b)** Theoretical TPCD spectra of R-BINOL and S-BINOL in THF. The experimental TPCD for a racemic mixture of BINOL is also shown

The resemblance between theory (See Figure 1-15.b) and experiment was striking, with all the major experimental features being reproduced for both enantiomers (See arrows between Figures 1-15.a and 1-15.b). The only relevant discrepancy found between theory and experiment

was that the experimental intensity of the TPCD was approximately 10^3 times larger than in the theory. This was tentatively attributed to exciton coupling effects and possible excited state absorption due to the use of picosecond pulses.

Overall, the work performed by Hernandez and co-workers on BINOL enantiomers proved the feasibility of the double-L scan as an effective, reliable and versatile method for the measurement of TPCD spectra of chiral molecules in solution. This seminal study served as a foundation for our theoretical–experimental research on TPCD.

In the next five chapters, we present the novel advances towards the deeper understanding of the structure-property relationship of TPCD. This thesis work is the fruit of a truly systematic study of optically active molecules with axial and helical chirality.

1.7. References

1. Sabra, A. I., *Theories of light, from Descartes to Newton*. CUP Archive: 1981.

2. Smith, A. M., Ptolemy's Theory of Visual Perception: An English Translation of the "Optics" with Introduction and Commentary. *Trans. Am. Philos. Soc.* **1996,** *86* (2), iii-300.

3. Mustroph, H.; Stollenwerk, M.; Bressau, V., Current developments in optical data storage with organic dyes. *Angew. Chem. Int. Ed.* **2006,** *45* (13), 2016-2035.

4. Escobedo, J. O.; Rusin, O.; Lim, S.; Strongin, R. M., NIR dyes for bioimaging applications. *Curr. Opin. Chem. Biol.* **2010,** *14* (1), 64-70.

5. Moerner, W., New directions in single-molecule imaging and analysis. *Proceedings of the National Academy of Sciences* **2007,** *104* (31), 12596-12602.

6. Nobelprize.org The Nobel Prize in Chemistry 2014 - Press Release. . (accessed Web. 9 Apr 2015).

7. Zewail, A. H., Four-dimensional electron microscopy. *Science* **2010,** *328* (5975), 187-193.

8. Denk, W.; Strickler, J.; Webb, W., Two-Photon Laser Scanning Fluorescence Microscopy. *Science* **1990,** *248*, 73-76.

9. Cumpston, B. H.; Ananthavel, S. P.; Barlow, S.; Dyer, D. L.; Ehrlich, J. E.; Erskine, L. L.; Heikal, A. A.; Kuebler, S. M.; Lee, I.-Y. S.; McCord-Maughon, D., *et al.*, Two-Photon Polymerization Initiators for Three-Dimensional Optical Data Storage and Microfabrication. *Nature* **1999,** *398*, 51-54.

10. Celli, J. P.; Spring, B. Q.; Rizvi, I.; Evans, C. L.; Samkoe, K. S.; Verma, S.; Pogue, B. W.; Hasan, T., Imaging and photodynamic therapy: mechanisms, monitoring, and optimization. *Chem. Rev.* **2010,** *110* (5), 2795-2838.

11. Pawlicki, M.; Collins, H. A.; Denning, R. G.; Anderson, H. L., Two-Photon Absorption and the Design of Two-Photon Dyes. *Angew. Chem. Int. Ed.* **2009,** *48* (18), 3244-3266.

12. He, G. S.; Tan, L.-S.; Zheng, Q.; Prasad, P. N., Multiphoton absorbing materials: molecular designs, characterizations, and applications. *Chem. Rev.* **2008,** *108* (4), 1245-1330.

13. Helmchen, F.; Denk, W., Deep tissue two-photon microscopy. *Nat. Methods* **2005,** *2* (12), 932-940.

14. Spangler, C., Recent development in the design of organic materials for optical power limiting. *J. Mater. Chem.* **1999,** *9* (9), 2013-2020.

15. Sun, H.-B.; Kawata, S., Two-photon photopolymerization and 3D lithographic microfabrication. In *NMR• 3D Analysis• Photopolymerization*, Springer: 2004; pp 169-273.

16. Burke, B. J.; Moad, A. J.; Polizzi, M. A.; Simpson, G. J., Experimental confirmation of the importance of orientation in the anomalous chiral sensitivity of second harmonic generation. *J. Am. Chem. Soc.* **2003,** *125* (30), 9111-9115.

17. Ji, N.; Ostroverkhov, V.; Belkin, M.; Shiu, Y. J.; Shen, Y. R., Toward Chiral Sum-Frequency Spectroscopy. *J. Am. Chem. Soc.* **2006,** *128*, 8845-8848.

18. Mesnil, H.; Hache, F., Experimental evidence of third-order nonlinear dichroism in a liquid of chiral molecules. *Phys. Rev. Lett.* **2000,** *85*, 4257-4260.

19. Baranowska, A.; Rizzo, A.; Jansík, B.; Coriani, S., Nonlinear effects in the interaction of time-dependent fields and chiral systems: A computational investigation. *J. Chem. Phys.* **2006,** *125* (5), 054107.

20. Gedanken, A.; Tamir, M., Multiphoton optical rotary dispersion. *Rev. Sci. Instrum.* **1987,** *58* (6), 950-952.

21. Power, E., *Developments in the theory of multiphoton absorption by molecules (bound-bound): Applications of a chirooptic character*. Plenum Press: New York, NY, USA: 1990.

22. Cameron, R.; Tabisz, G. C., Observation of Two-Photon Optical Rotation by Molecules. *Mol. Phys.* **1997,** *90*, 159-164.

23. Cameron, R.; Tabisz, G. C., Characterization of intensity-dependent optical rotation phenomena in chiral molecules in solution. *J. Chem. Phys.* **2007,** *126*.

24. Qu, W.; Tabisz, G. C., Ab initio calculations of nonlinear optical rotation by several small chiral molecules and by uridine stereoisomers. *J. Chem. Phys.* **2006,** *124* (18), 184305.

25. McConnell, O.; Bach, A.; Balibar, C.; Byrne, N.; Cai, Y.; Carter, G.; Chlenov, M.; Di, L.; Fan, K.; Goljer, I., *et al.*, Enantiomeric Separation and Determination of Absolute Stereochemistry of Asymmetric Molecules in Drug Discovery: Building Chiral Technology Toolboxes. *Chirality* **2007,** *19*, 658-682.

26. Noyori, R., Asymmetric Catalysis: Science and Opportunities (Nobel Lecture). *Angew. Chem. Int. Ed. Engl.* **2002,** *41* (12), 2008-2022.

27. Tamura, K., Origin of Amino Acid Homochirality: Relationship with the RNA World and Origin of tRNA Aminoacylation. *BioSyst.* **2008,** *92*, 91-98.

28. Nakanishi, K.; Berova, N.; Woody, R. W., *Circular Dichroism: Principles and Applications*. 2nd ed.; VCH: New York, 2000.

29. Tinoco, I., Jr.; Mickols, W.; Maestre, M. F.; Bustamante, C., Absorption, Scattering, and Imaging of Biomolecular Structures with Polarized Light. *Annu. Rev. Biophys. Biophys. Chem.* **1987,** *16*, 319-349.

30. Tinoco, I., Two-Photon Circular Dichroism. *J. Chem. Phys.* **1975,** *62*, 1006-1009.

31. Power, E. A., Two-Photon Circular Dichroism. *J. Chem. Phys.* **1975,** *63*, 1348-1350.

32. Jansik, B.; Rizzo, A.; Agren, H., Response Theory Calculations of Two-Photon Circular Dichroism. *Chem. Phys. Lett.* **2005,** *414*, 461-467.

33. Gunde, K. E.; Richardson, F. S., Fluorescence-Detected Two-Photon Circular Dichroism of Gd^{3+} in Trigonal $Na_3[Gd(C_4H_4O_5)_3] \cdot 2NaClO_4 \cdot 6H_2O$. *Chem. Phys.* **1995,** *194*, 195-206.

34. De Boni, L.; Toro, C.; Hernandez, F. E., Synchronized Double L-Scan Technique for the Simultaneous Measurement of Polarization-Dependent Two-Photon Absorption in Chiral Molecules. *Opt. Lett.* **2008,** *33*, 2958-2960.

35. Toro, C.; De Boni, L.; Lin, N.; Santoro, F.; Rizzo, A.; Hernandez, F. E., Two-Photon Absorption Circular Dichroism: A New Twist in Nonlinear Spectroscopy. *Chem. Eur. J.* **2010,** *16*, 3504-3509.

36. Spencer, N. D.; Moore, J. H., *Encyclopedia of chemical physics and physical chemistry: Methods*. Taylor & Francis: 2001; Vol. 2.

37. Lakowicz, J. R., *Principles of fluorescence spectroscopy*. 3rd ed.; Springer Science & Business Media: 2007.

38. Condon, E. U.; Altar, W.; Eyring, H., Theories of Optical Rotatory Power. *Reviews of Modern Physics* **1937,** *9* (4), 432-457.

39. Goeppert-Mayer, M., Uber Elementarakte mit zwei Quantensprungen. *Ann. Phys.* **1931,** *8*, 273-294.

40. Maiman, T., Stimulated emission of radiation in ruby. *Nature* **1960,** *187*, 493-494.

41. Boyd, R. W., *Nonlinear Optics*. Academic Press: San Diego, CA, 1992.

42. Sheik-Bahae, M.; Said, A. A.; Wei, T. H.; Hagan, D. J.; Van Stryland, E. W., Sensitive measurement of optical nonlinearities using a single beam. *IEEE J. Quantum Electron.* **1990,** *26*, 760-769.

43. Peiponen, K.; Saarinen, J., Generalized Kramers–Kronig relations in nonlinear optical-and THz-spectroscopy. *Rep. Prog. Phys.* **2009,** *72* (5), 056401.

44. Sheik-Bahae, M.; Hasselbeck, M. P., Third-order optical nonlinearities. *Handbook of Optics* **2000,** *4*, 16.11-16.36.

45. Bonin, K. D.; McIlrath, T. J., Two-Photon Electric-Dipole Selection Rules. *J. Opt. Soc. Am. B* **1984,** *1*, 52-55.

46. McClain, W.; Harris, R.; Lim, E., Excited States. *Lim, EC, Ed* **1977**, 1-56.

47. Fernández, I.; Cossío, F. P., Applied computational chemistry. *Chem. Soc. Rev.* **2014,** *43* (14), 4906-4908.

48. Runge, E.; Gross, E. K. U., Density-Functional Theory for Time-Dependent Systems. *Phys. Rev. Lett.* **1984,** *52*, 997-1000.

49. Dierksen, M.; Grimme, S., A Theoretical Study of the Chiroptical Properties of Molecules with Isotopically Engendered Chirality. *J. Chem. Phys.* **2006,** *124*, 174301.

50. Masunov, A.; Tretiak, S., Prediction of two-photon absorption properties for organic chromophores using time-dependent density-functional theory. *J. Phys. Chem. B* **2004,** *108* (3), 899-907.

51. Becke, A. D., Density-Functional Exchange-Energy Approximation with Correct Asymptotic Behavior. *Phys. Rev. A* **1988,** *38*, 3098-3100.

52. Becke, A. D., Density-Functional Thermochemistry. III. The Role of Exact Exchange. *J. Chem. Phys.* **1993,** *98*, 5648-5652.

53. Lee, C.; Yang, W.; Parr, R. G., Development of the Colle-Salvetti Correlation-Energy Formula into a Functional of the Electron Density. *Phys. Rev. B: Condens. Matter* **1988,** *37*, 785-789.

54. Yanai, T.; Tew, D. P.; Handy, N. C., A new Hybrid Exchange-Correlation Functional using the Coulomb-Attenuating Method (CAM-B3LYP). *Chem. Phys. Lett.* **2004,** *393*, 51-57.

55. Peach, M. J. G.; Helgaker, T.; Sałek, P.; Keal, T. W.; Lutnaes, O. B.; Tozer, D. J.; Handy, N. C., Assessment of a Coulomb-attenuated exchange-correlation energy functional. *Phys. Chem. Chem. Phys.* **2006,** *8*, 558-562.

56. Guillaume, M.; Ruud, K.; Rizzo, A.; Monti, S.; Lin, Z.; Xu, X., Computational Study of the One- and Two-Photon Absorption and Circular Dichroism of (L)-Tryptophan. *J. Phys. Chem. B* **2010,** *114*, 6500-6512.

57. McClain, W. M., Two-Photon Molecular Spectroscopy. *Acc. Chem. Res.* **1974,** *7*, 129-135.

58. Macák, P., *Solvent and vibrational effects on nonlinear optical properties*. Ph. D. thesis, Royal Institute of Technology: Stockholm: 2002.

59. Cammi, R.; Cappelli, C.; Mennucci, B.; Tomasi, J., Properties of Excited States of Molecules in Solution Described with Continuum Solvation Models. In *Practical Aspects of Computational Chemistry*, Springer: 2010; pp 19-36.

60. Onsager, L., Electric moments of molecules in liquids. *J. Am. Chem. Soc.* **1936,** *58* (8), 1486-1493.

61. Tapia, O.; Goscinski, O., Self-consistent reaction field theory of solvent effects. *Mol. Phys.* **1975,** *29* (6), 1653-1661.

62. Miertuš, S.; Scrocco, E.; Tomasi, J., Electrostatic Interaction of a Solute with a Continuum. A Direct Utilizaion of AB Initio Molecular Potentials for the Prevision of Solvent Effects. *Chem. Phys.* **1981,** *55* (1), 117-129.

63. Tomasi, J.; Mennucci, B.; Cammi, R., Quantum Mechanical Continuum Solvation Models. *Chem. Rev.* **2005,** *105*, 2999-3093.

64. de O. Mendes, C. L.; da Silva, C. O.; da Silva, E. C., Parametrizing PCM to obtain solvation free energies from group contributions. 1. *J. Phys. Chem. A* **2006,** *110* (11), 4034-4041.

65. Rumi, M.; Perry, J. W., Two-photon absorption: an overview of measurements and principles. *Advances in Optics and Photonics* **2010,** *2* (4), 451-518.

66. Anderson, R. J.; Holtom, G. R.; McClain, W. M., Absolute two-photon absorptivity of trans-stilbene near the two-photon absorption maximum via three wave mixing. *J. Chem. Phys.* **1977,** *66* (8), 3832-3833.

67. Anderson Richard, J.; Holtom Gary, R.; McClain Wm, M., Two-photon absorptivities of the all transdiphenylpolyenes from stilbene to diphenyloctatetraenl via t hree wave m ixing. *J. Chem. Phys.* **1979,** *70* (9), 4310-4315.

68. Orczyk, M.; Samoc, M.; Swiatkiewicz, J.; Manickam, N.; Tomoaia-Cotisel, M.; Prasad, P., Optical heterodyning of the phase-tuned femtosecond optical Kerr gate signal for the determination of complex third-order susceptibilities. *Appl. Phys. Lett.* **1992,** *60* (23), 2837-2839.

69. Pfeffer, N.; Charra, F.; Nunzi, J. M., Phase and frequency resolution of picosecond optical Kerr nonlinearities. *Opt. Lett.* **1991,** *16* (24), 1987-1989.

70. Zhao, M.; Cui, Y.; Samoc, M.; Prasad, P. N.; Unroe, M. R.; Reinhardt, B. A., Influence of two-photon absorption on third-order nonlinear optical processes as studied by degenerate four-wave mixing: The study of soluble didecyloxy substituted polyphenyls. *J. Chem. Phys.* **1991,** *95* (6), 3991-4001.

71. Sutherland, R.; Rea, E.; Natarajan, L.; Pottenger, T.; Fleitz, P., Two-photon absorption and second hyperpolarizability measurements in diphenylbutadiene by degenerate four-wave mixing. *J. Chem. Phys.* **1993,** *98* (4), 2593-2603.

72. Xu, C.; Webb, W. W., Measurement of two-photon excitation cross sections of molecular fluorophores with data from 690 to 1050 nm. *Journal of the Optical Society of America B-Optical Physics* **1996,** *13*, 481-491.

73. Birge, R. R., One-photon and two-photon excitation spectroscopy. *Ultrasensitive laser spectroscopy* **1983**, 109-174.

74. Eliel, E. L.; Wilen, S. H., *Stereochemistry of organic compounds*. John Wiley & Sons: 2008.

75. Hecht, E., *Optics*. Pearson Education, Inc.: San Francisco, 2002.

76. Berova, N.; Polavarapu, P. L.; Nakanishi, K.; Woody, R. W., *Comprehensive Chiroptical Spectroscopy*. John Wiley & Sons: Hoboken, NJ, 2012; Vol. 2.

77. Polavarapu, P. L., Kramers-Kronig transformation for optical rotatory dispersion studies. *J. Phys. Chem. A* **2005,** *109*, 7013-7023.

78. Miles, A. J.; Wallace, B. A., Synchrotron Radiation Circular Dichroism Spectroscopy of Proteins and Applications in Structural and Functional Genomics. *Chem. Soc. Rev.* **2006,** *35*, 39-51.

79. Mason, W. R. A., *Practical Guide to Magnetic Circular Dichroism Spectroscopy*. John Wiley & Sons: New Jersey, 2007.

80. Devlin, F. J.; Stephens, P. J.; Scafato, P.; Superchi, S.; Rosini, C., Determination of Absolute Configuration Using Vibrational Circular Dichroism Spectroscopy: The Chiral Sulfoxide 1-thiochromanone S-Oxide. *Chirality* **2002,** *14*, 400-406.

81. Barron, L. D., *Molecular Light Scattering and Optical Activity*. Cambridge University Press: Cambridge, 2004.

82. Jansík, B.; Rizzo, A.; Agren, H., Ab Initio Study of the Two-Photon Circular Dichroism in Chiral Natural Amino Acids. *J. Phys. Chem. B* **2007,** *111*, 446-460.

83. Thirunamachandran, T.; Craig, D. P., *Molecular Quantum Electrodynamics, An Introduction to Radiation Molecule Interaction*. Dover Publ., Inc., Mineaol, NY: 1998.

84. Markowicz, P. P.; Samoc, M.; Cerne, J.; Prasad, P. N.; Pucci, A.; Ruggeri, G., Modified Z-scan Techniques for Investigations of Nonlinear Chiroptical Effects. *Opt. Express* **2004,** *12*, 5209-5214.

85. Li, R.; Sullivan, R.; Al-Basheer, W.; Pagni, R. M.; Compton, R. N., Linear and nonlinear circular dichroism of R-(+)-3-methylcyclopentanone. *J. Chem. Phys.* **2006,** *125*.

86. Bornschlegl, A.; Logé, C.; Boesl, U., Investigation of CD effects in the multi photon ionisation of R-(+)-3-methylcyclopentanone. *Chem. Phys. Lett.* **2007,** *447*, 187-191.

87. Hernández, F. E.; Rizzo, A., Two-Photon Polarization Dependent Spectroscopy in Chirality: a Novel Experimental-Theoretical Approach to Study Optically Active Systems. *Molecules (Basel, Switzerland)* **2011,** *16*, 3315-3337.

88. Toro, C.; De Boni, L.; Lin, N.; Santoro, F.; Rizzo, A., Two-Photon Absorption Circular-Linear Dichroism on Axial Enantiomers. *Chirality* **2010,** *22*, E202-E210.

89. Krishnan, R.; Binkley, J. S.; Seeger, R.; Pople, J. A., Self-Consistent Molecular Orbital Methods. XX. A Basis Set for Correlated Wave Functions. *J. Chem. Phys.* **1980,** *72* (1), 650-654.

90. Clark, T.; Chandrasekhar, J.; Spitznagel, G. W.; Schleyer, P. V. R., Efficient Diffuse Function-Augmented Basis Sets for Anion Calculations. III. The 3-21+G Basis Set for First-Row Elements, Li–F. *J. Comput. Chem.* **1983,** *4* (3), 294-301.

91. Kendall, R. A.; Dunning, T. H.; Harrison, R. J., Electron affinities of the first-row atoms revisited. Systematic basis sets and wave functions. *J. Chem. Phys.* **1992,** *96* (9), 6796-6806.

92. Frisch, M. J.; Trucks, G. W.; Schlegel, H. B.; Scuseria, G. E.; Robb, M. A.; Cheeseman, J. R.; Montgomery, J., J. A.; Vreven, T.; Kudin, K. N.; Burant, J. C., *et al.*, Gaussian 03, Revision C.03. Gaussian, Inc.: Wallingford CT, 2004.

93. DALTON *A Molecular Electronic Structure Program, Release Dalton 2.0, see http://www.kjemi.uio.no/software/dalton/dalton.html*, 2005.

CHAPTER 2 : THE EFFECT OF THE Π-ELECTRON DELOCALIZATION ON THE TWO-PHOTON CIRCULAR DICHROISM OF MOLECULES WITH AXIAL CHIRALITY

Reproduced with permission of the American Chemical Society from: C. Diaz, N. Lin, C. Toro, R. Passier, A. Rizzo, F.E. Hernández, J. Phys. Chem. Lett. ***2012****, 3, 1808-1813.*

In this first chapter, we present the theoretical-experimental study of the effect of the π-electron delocalization curvature on the TPCD signal of molecules with axial chirality. The targeted molecules for this part of our investigation were S-BINOL, S-VANOL, and S-VAPOL. Our findings revealed that an increase in the TPCD signal, within this series of compounds, is strictly related to a greater curvature of the π–electron delocalization. The contributions of the different transition moments to the two-photon rotatory strength explain the outcomes. Theoretical calculations for the studied family of compounds were performed considering solvent effects as implemented in the polarizable continuum model (PCM) at the B3LYP/aug-cc-pVDZ and CAM-B3LYP/aug-cc-pVDZ, levels of theory. The theoretical-experimental analysis of the TPCD spectra was based on the former approach because it better reproduced the spectral features found experimentally. The better performance of B3LYP is attributed to a weak intramolecular charge transfer of the excited states contributing to the spectra of the family of biaryl derivatives.

2.1 Introduction

The understanding of chiral systems has been the aim of study of many scientists in our community during the last two decades. This effort has been mainly motivated by the central role this type of molecules play in biological processes, [1] their implications in the drug and food industry, [2, 3] their applications in nanotechnology, [4] optics and photonics [5] and in asymmetric catalysis. [6]

In particular, asymmetric catalysts have allowed for the synthesis of highly enantiomerically pure compounds without the need of complex chiral separations. BINOL derivatives are among the asymmetric catalysts with the most applications. These molecules exhibit a high degree of chiral selectivity over a broad range of reactions, and are widely used in fundamental and applied research, as well as in industry. [6] VANOL and VAPOL are among the best known BINOL derivatives. The common feature of these molecules is the chiral axis at the center of their binaphtyl core (See Figure 2-1). Their ability to limit racemization resides in the selectivity imposed by the C_2-symmetry framework that is product of the atropisomerism found on these compounds.

Few years ago, and after developing the double L-scan technique, [7] Hernandez and co-workers demonstrated experimentally two-photon circular dichroism (TPCD) in S−BINOL and R−BINOL. These remarkable results proved the theoretical predictions done first by Tinoco and Power in the 1970s, [8, 9] and which were revitalized thirty years later by Rizzo and co-workers. [10] Although, Hernandez *et al.* have already revealed the complex contribution of the excited states to the overall TPCD rotatory strength, i.e. the parameter that determines the TPCD signal of chiral systems, [11] TPCD is still in its infancy. Therefore, there is still a great need of more systematic studies to truly understand the structure-property relationship of this phenomenon.

In order to expand on this initial investigation, in this chapter, we report on the theoretical-experimental study of the TPCD of BINOL, VANOL and VAPOL. Specifically, we investigated the effect of the π-electron delocalization curvature on the TPCD.

2.2 Experimental Section

(S)–3,3'–Diphenyl–[2,2'–binaphthalene]– 1,1'–diol (S–VANOL), (S)–2,2'–Diphenyl–[3,3'–biphenanthrene]–4,4'–diol (S–VAPOL) and tetrahydrofuran (THF) were purchased from Sigma-Aldrich and used without further purification. The linear absorption spectra of all the compounds were measured in 0.2 mM/THF solutions placed in a 1 mm quartz cell, using a single beam Agilent 8453 spectrometer (contributions from the solvent and the cell were always subtracted). The nonlinear optical characterization of these compounds was performed using the double L-scan technique[7] in THF solutions at a concentration of 0.1 M. Two-photon excitation was induced with an optical parametric generator, pumped by the third harmonic of a mode-locked Nd:YAG laser, operating at 10 Hz repetition rate and a pulse width of 25 ps (FWHM). The covered spectral range was from 440 to 700 nm. The absence of molecular aggregates in solution at such a high concentration was corroborated by examining the UV-vis spectra and comparing the two-photon absorption cross-sections of two different solutions (0.1 and 0.002 M). The UV-vis spectra and the cross-sections did not change with the concentration. In addition, the visible inspection of the solutions did not reveal the formation of clusters.

2.3 Computational Methods

The theoretical background involved in this research has been given in detail in references 12-17 and is also presented in sections 1.2 and 1.5 of the introduction to this

dissertation. Therefore, in this part we only present the computational details relevant to the corresponding calculations.

The optimized gas phase structures of S-VANOL and S-VAPOL were obtained from Polavarapu *et. al.* [18, 19] Both structures were re-optimized, to include solvent effects, using Becke's three-parameter exchange, Lee, Yang, Parr correlation (B3LYP) [20-22] level of theory. Basis set 6-31G* [23] was used for all calculations under C_2 geometry restrictions, using GAUSSIAN 09. [24] The polarizable continuum model (PCM) [25, 26] was employed to simulate the effect of CH_2Cl_2 using: a) universal force field radii with a multiplicative factor of 1.1 and b) a non-equilibrium regime for CH_2Cl_2 with a dielectric constant of 8.930 and an optical dielectric constant of 2.028. Note: CH_2Cl_2 was employed in the calculations and not THF because the cavity for the former was one of the few implemented in Dalton for the calculations of TPCD.

Two-photon absorption (TPA) and two-photon circular dichroism (TPCD) were calculated for the first 20 electronic excited states of the B3LYP/6-31G* optimized structures using time-dependent density functional theory (TD-DFT), [27, 28] specifically, DFT/B3LYP, [20-22] and DFT/CAM-B3LYP [29, 30] with the 6-31G* basis set (the largest basis set we could afford given the size of the molecules and the computational cost of the two-photon calculations) and PCM for CH_2Cl_2 using the same dielectric constant parameters used for the geometry optimizations, employing DALTON 2.0. [31] The convolution of the TPA and TPCD spectra were obtained employing Equations 1-18 and 1-37 (See dissertation introduction), respectively, using a normalized Lorentzian lineshape (See Equation 1-15 in dissertation introduction) with Γ = 0.20 eV (FWHM). The CAM-B3LYP method has proven to give reliable results for this kind of compound, mainly for properties involving delocalized, Rydberg or charge-transfer, in general diffuse excited states. [32] However, it tends to overestimate excitation energies and yield little if

any improvement with respect to its still more popular alternative, B3LYP, in the region of low lying, valence excited states. [13, 32] Therefore, the latter was chosen to explain the most intense TPA and TPCD response of S-VANOL and S-VAPOL (see bands below 250 nm in Figures 2-2 and 2-3) with less uncertainty.

2.4 Results and Discussion

S–BINOL, S-VANOL, and S-VAPOL were chosen for this investigation because of their molecular structures (see Figure 2-1) and their great applicability as chiral auxiliaries in asymmetric catalysis. [33] In addition, they are all commercially available in high enantiomeric excess (enantiomeric ratio *R*:*S* ≥ 99:1).

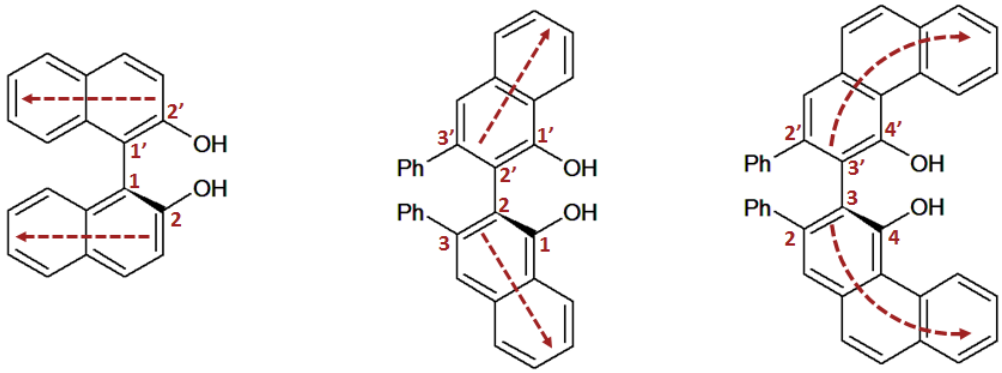

Figure 2-1. Molecular structures of S-BINOL (left), S-VANOL (center) and S-VAPOL (right). The arrows inside the molecules display the direction of the π–electron delocalization. The numbering for some carbon atoms is shown.

The theoretical (DFT/B3LYP) and experimental TPA spectra of S-BINOL, [34] S-VANOL and S-VAPOL, using linearly polarized light (LPL) and plotted at half of their excitation wavelength, are displayed in Figure 2-2. In order to show a better overlapping between experiment and theory, the theoretical spectra were slightly shifted by: +18 nm, -17 nm and -3 nm for S-BINOL, S-VANOL and S-VAPOL, respectively. Here, we ought to mention that

calculations using B3LYP and CAM-B3LYP (data not shown) reproduced quite well the spectral position. However, the former method yields a better reproduction of the observed experimental spectral features. Therefore, the discussion solely focuses on the results obtained using B3LYP.

The first observation in Figure 2-2 is the theoretical-experimental spectral matching in all the spectra. The matching is excellent in S-BINOL (bands at *ca.* 230 nm and 275 nm). The features get more intricate for S-VANOL and S-VAPOL. For S-VANOL the experiment shows a broad band at 270nm, followed by an increase in absorption arising below 240 nm. Our calculations yield some intensity above 280 nm, then a couple of states absorbing around 240 nm and a strong increase in absorption for our frontier states (the 19^{th} and the 20^{th}). It is likely that further TPA strengths might be produced by states beyond the 20^{th}, which would contribute then to the sharp increase in the experiment. In the range of wavelengths explored in the experiment, the TPA absorption of S-VANOL is therefore reasonably reproduced by theory. For S-VAPOL the distribution of two-photon strengths is more complex, with a sequence of two-photon absorption strengths of different intensities lying between 330 and 220 nm. The bands seen in the experiment at 320 nm and 280 nm and the increase in intensity at the low wavelength end of the interval (220 nm) are all in correspondence with electronic states which are particularly active in two-photon absorption.

The second observation is related to the differences in magnitude between the theory and the experiment. While in S-BINOL and S-VANOL the two magnitudes differ by approximately eight and four folds, respectively, the difference increases for S-VAPOL. The difference in magnitude between the theory and experiment was already attributed, in Ref. 11, to exciton coupling for dimers undergoing electrically allowed transitions[35, 36] and excitation pulse width of the excitation source which can lead to excited-state absorption. The contribution of the latter, in

measurements of polarization dependent optical properties of organics, was recently reported in the literature. [37, 38]

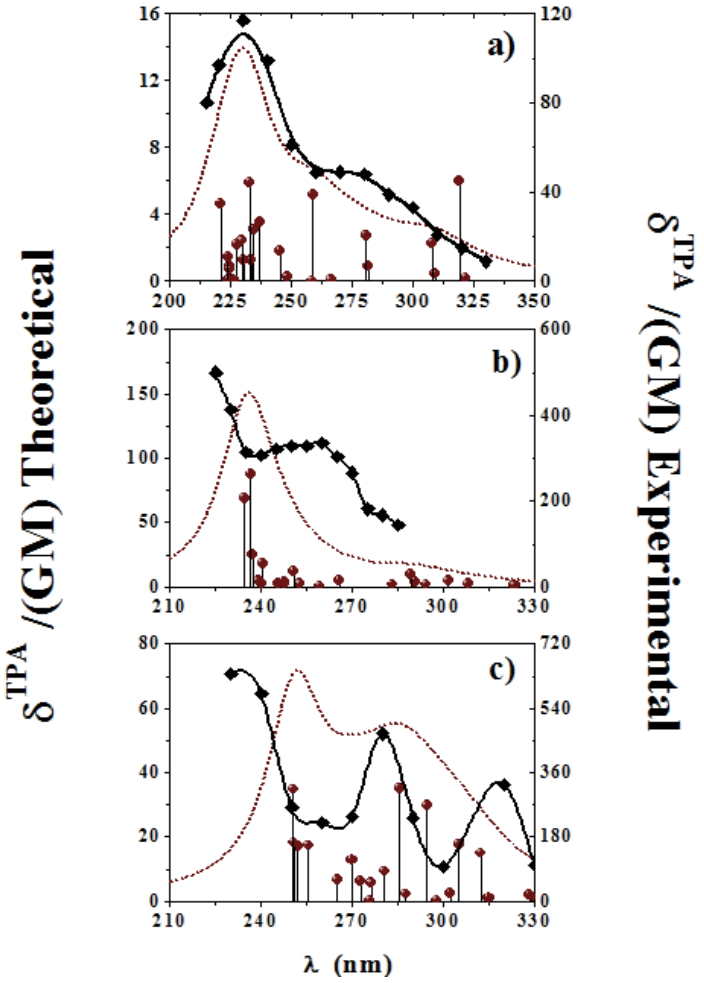

Figure 2-2. TPA spectra of S-BINOL (a), S-VANOL (b) and S-VAPOL (c), plotted at half of the excitation wavelength. Theoretical electronic transitions with Lorentzian convolution [linewidth 0.20 eV FWHM] (scattered spheres and dashed lines), and experimental TPA spectra (solid line with filled squares). The theoretical spectra are shifted +18 nm, -17 nm and -3 nm for S-BINOL, S-VANOL and S-VAPOL, respectively.

The third and perhaps the most relevant observation in Figure 2-2 is the fact that the theoretical and experimental TPA cross-sections show the same trend: $\delta^{TPA}_{S-BINOL}(\lambda) << \delta^{TPA}_{S-VANOL}(\lambda) \approx \delta^{TPA}_{S-VAPOL}$. This tendency suggests the existence of a weaker charge transfer in S-BINOL compared to that in the other two compounds due to the position of the

external phenyl ring in the naphthalene and phenanthrene systems. This statement is supported by the position of the theoretical and experimental maximum of the linear absorption spectra of all three compounds ($\lambda_{Max,S\text{-}BINOL} \approx 229$ nm, $\lambda_{Max,S\text{-}VANOL} \approx 248$ nm and $\lambda_{Max,S\text{-}VAPOL} \approx 266$ nm) [18, 19, 32] which indicates a shorter effective extent of the π–electron delocalization in S-BINOL. However, the difference in $\delta_i^{TPA}(\lambda)$ between the last two is less important. This implies that the conjugation through the π–system is not effectively increased going from S-VANOL to S-VAPOL because of the twist in the π–electron delocalization found in the latter (see Figure 2-1). This result is consistent with the extensive theoretical-experimental evidence given in the literature sustaining that the dependence of the TPA cross-section of conjugated systems with respect to the π-electron delocalization length is more effective in molecules with one dimensional (linear) charge transfer. [39] Note: Electron delocalization to the phenyl rings attached in positions 3,3' in S-VANOL and 2,2'in S-VAPOL, is considered negligible because of the large dihedral angle (~ 53^0) existent between the two systems. [19, 40]

In Figure 2-3 we present the theoretical (DFT/B3LYP) and experimental TPCD spectra of S-BINOL,[21] S-VANOL and S-VAPOL, plotted at half of their excitation wavelength. In these plots the suitable spectral agreement between the theory and the experiment is noticeable (All theoretical $R_{0f}^{TPCD}(\omega_{0f})$ have the same spectral shift utilized in Figure 2-2). In S-BINOL, R_{0f}^{TPCD} over the entire spectrum clearly sums-up to reproduce the main spectral features, i.e. overall negative signal and a negative band at 225 nm. In S-VANOL, a series of negative transitions spanning from 240 nm to 320 nm are in agreement with the sum of negative bands within the same region. The experimental positive band centered at 245 nm is not observed in the theoretical spectrum. Again, it is likely that further R_{0f}^{TPCD} might be produced by states beyond

the 20th, which would reproduce the mentioned positive band. Although, states 18 and 19 have the strongest intensity their net contribution to R_{0f}^{TPCD} cancels almost completely because of their spectral proximity as explained in Ref. 11. Experiment and theory display a series of positive and negative contributions in S-VAPOL. Positive transitions at 255 nm, 270 nm, 285 nm, 302 nm and 328 nm reproduce the positive bands centered at 250 nm, 280 nm and 330 nm. Negative transitions at 250 nm, 272 nm, 280 nm, 294 nm, 299 nm, 305 nm, are in agreement with negative bands centered at 245 nm, 270 nm and 290 nm.

The moderate theoretical-experimental agreement in S-VAPOL, could perhaps be attributed to the quality of the chosen basis set (6-31G*). Using the aug-cc-pVDZ in this molecule represented a very expensive computational challenge for us. Nevertheless, since our level of theory has been proven to predict, [32] at least qualitatively, the behaviors and trends in systems exhibiting axial chirality, the use of the chosen functional and basis set for S-VAPOL is justified.

Another interesting observation in Figure 2-3 is the resultant trend in the TPCD signal magnitude of these three biaryl derivatives, i.e. $\Delta\delta_{S-BINOL}^{TPCD} < \Delta\delta_{S-VANOL}^{TPCD} < \Delta\delta_{S-VAPOL}^{TPCD}$. Although there is a difference in magnitude between the theoretical and the experimental values, the observed tendency is the same in both cases. Knowing that the TPCD signal directly depends on the different contributions from the electric transition quadrupole moment and the magnetic transition dipole moment through R_{0f}^{TPCD} (See Equation 0-38), a comparison of the weight of each of these parameters to $\Delta\delta^{TPCD}$, in all three molecules, was performed by theoretical means.

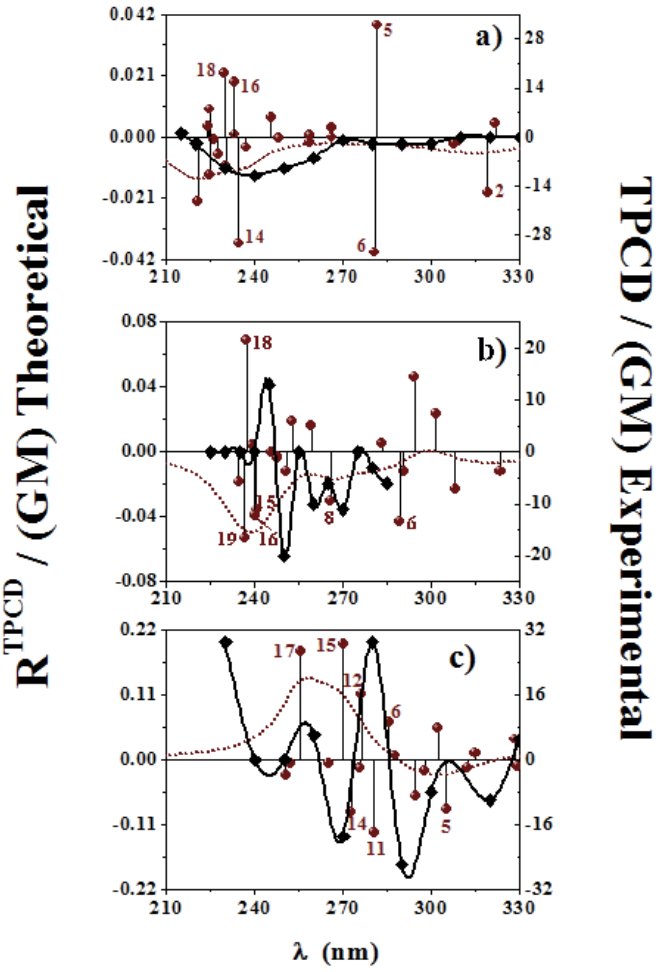

Figure 2-3. TPCD spectra of S-BINOL (a), S-VANOL (b) and S-VAPOL (c), plotted at half of the excitation wavelength. Theoretical electronic transitions with Lorentzian convolution [linewidth 0.20 eV FWHM] (scattered spheres and dashed lines), and experimental TPA spectra (solid line with filled squares). The theoretical spectra are shifted +18 nm, -17 nm and -3 nm for S-BINOL, S-VANOL and S-VAPOL, respectively. The numbers in the plots refer to some of the most important excited states to the TPCD signal.

Figure 2-4 displays the contribution of the electric transition quadrupole moment [B_2 *vs.*λ] and the magnetic transition dipole moment [(B_1+B_3) *vs.* λ] to R_{0f}^{TPCD}, between 200 nm and 350 nm. In Figure 2-4.a one can observe an overwhelming influence of the electric transition quadrupole moment $\left(B_{2\,S-BINOL} < B_{2\,S-VANOL} < B_{2\,S-VAPOL}\right)$ onto the TPCD on S-VAPOL (mainly within the strongest TPA region), followed by that of S-VANOL in the spectral region above 250 nm.

The weight of B_2 in S-BINOL is very small. This outcome was anticipated after examining the molecular structure of all three molecules and realizing that the position of the external ring in S-VANOL and S-VAPOL, compared to that in S-BINOL, favors a larger charge transfer away from the center of the molecule or *vice-versa* (in S-BINOL the spherically-symmetrical electronic charge distribution is mostly retained). [41]

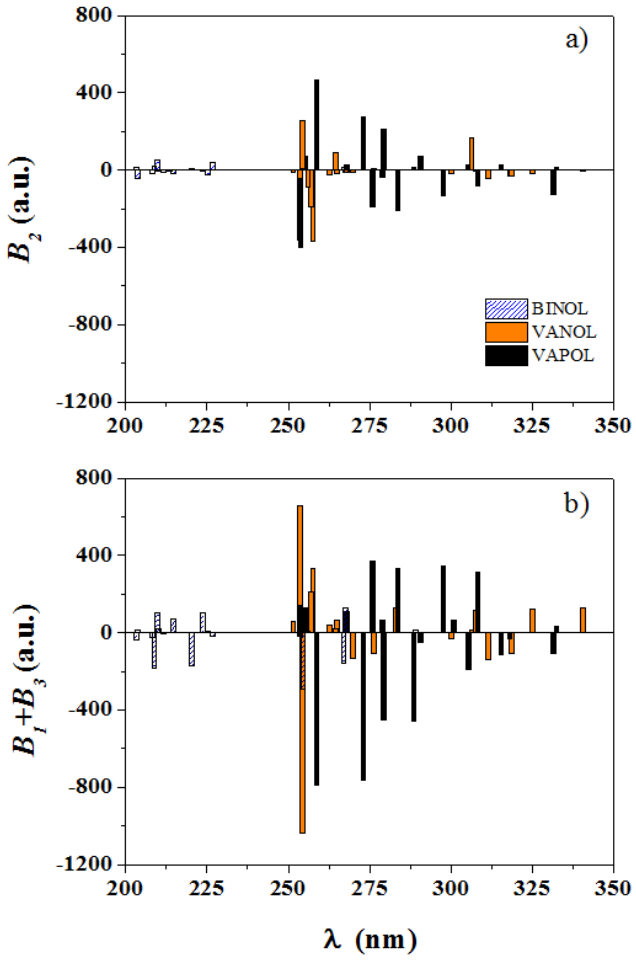

Figure 2-4. Plot of molecular parameter B_2 *vs.* λ (a) and and B_1+B_3 *vs.* λ (b), λ is half of the excitation wavelength. S-BINOL (patterned bars), S-VANOL (orange bars) and S-VAPOL (solid black bars).

The most remarkable finding, however, is the overpowering contribution of the magnetic transition dipole moment to the TPCD signal in S-VAPOL (see Figure 2-4.b). The observed trend of this effect turns out to be $(B_1 + B_3)_{S-BINOL} < (B_1 + B_3)_{S-VANOL} < (B_1 + B_3)_{S-VAPOL}$. $(B_1 + B_3)_{S-BINOL} < (B_1 + B_3)_{S-VANOL}$ is the result of the relative position of the two naphthalene moieties with respect to the center of the molecule. While in S-BINOL, the π–electron delocalization, considering both moieties, takes place at a normal angle (~89^0), in S-VANOL it happens at approximately 125^0 (see Figure 2-1). Therefore, a stronger contribution of the magnetic transition dipole moment to the TPCD signal in S-VANOL, compared to that S-BINOL, can be expected due to the slight helicity found in the former. In S-VAPOL this effect is even stronger. In addition to having the two phenanthrene structures in a similar relative orientation as the two naphthalenes in S-VANOL, S-VAPOL has its third and most external phenyl ring in the aromatic system in a position that imposes an additional curvature to the π–electron delocalization (see Figure 2-1). This twist in the π–electron delocalization induces a stronger contribution of the magnetic transition dipole moment to the TPCD signal of this molecule compared to the other two. The apparent large contribution of $(B_1 + B_3)$ to the TPCD of S-VANOL, at 255 nm, is broadly cancelled by the two, opposite in sign but relatively close in amplitude, transitions (states 18 and 19) observed at virtually the same wavelength (Figure 2-4.b). The effect of cancellation of contributions that affect the shape and amplitude of the TPCD spectrum of chiral molecules has already been observed by Rizzo and co-workers in S-BINOL (e.g. excited states 5 and 6). [11]

In order to corroborate this outcome, a comparison between the summations over the absolutes values of both contributions, independently, to the TPCD signal in each molecule was performed (See Table 2-1). In this comparison we have also included the absolute values of those contributions in S-VANOL (255 nm) that cancelled in the TPCD spectrum to make a fair evaluation of the effect. First, values displayed in Table 2-1 show a clear augmentation of both contributions the electric transition quadrupole moment and the magnetic transition dipole moment, going from S-BINOL to S-VAPOL. The greater increase of the contribution of the latter to R_{0f}^{TPCD} is evident. This comparative analysis is in agreement with the explanation given above. Therefore, the contribution of the magnetic transition dipole moment to the TPCD signal in S-VAPOL is enhanced as a result of the extra twist present in the π–electron delocalization in this vaulted structure. Our explanation is supported by previous theoretical works on photo-induced electric currents in ring-shape molecules, [42] and chiral control of electron transfer in helical molecular bridges, both using circularly polarized radiation. [43] While in the former the authors demonstrate that ring currents, originated by a second-order nonlinear optical response, produces a magnetic dipole moment in aromatic molecules, in the latter Skourtis *et al*. describe the effect in the framework of a general novel phenomenon of transfer of charge with its momentum information.

Table 2-1. Summation over the absolute values of the theoretical molecular parameters $|B_2|$ and $|B_1 + B_3|$ in *S-BINOL*, S-VANOL and S-VAPOL, from 200 nm to 350 nm, using B3LYP.

	$\sum_{i=1}^{20}\|B_2\|$	$\sum_{i=1}^{20}\|B_1 + B_3\|$
S-BINOL	347.80	1,190.04
S-VANOL	1,402.89	3,654.55
S-VAPOL	2,770.71	5,421.73

2.5 Conclusion

In summary, the comparative analysis of the measured and calculated TPA and TPCD spectra on a series of compounds with axial chirality led us to a better understanding of the molecular structure-property relationships of TPCD. The TPCD signal varied according to $\Delta\delta^{TPACD}_{S-BINOL} < \Delta\delta^{TPACD}_{S-VANOL} < \Delta\delta^{TPACD}_{S-VAPOL}$. This trend obeys the contributions of the different transition moments to the TPCD signal. On the one hand, we found that the influence of the electric transition quadrupole moment to the TPCD becomes more important in molecule in which the charge transfer away from the center of the molecule or *vice versa*, is favored. On the other hand, we determined that the effect of the magnetic transition dipole moment to the TPCD rotatory strength, thus the TPCD signal, is strongly enhanced by the twist in the π–electron delocalization of the chiral molecules.

An important finding during this part of the thesis work was the increase in computational cost with the size of the aryl derivatives. Finding ways to overcome the anticipated computational limitations to calculate TPCD spectra of molecules as their size and complexity increases is very much required.

2.6 References

1. Tamura, K., Origin of Amino Acid Homochirality: Relationship with the RNA World and Origin of tRNA Aminoacylation. *BioSyst.* **2008,** *92*, 91-98.

2. Simo, C.; Barbas, C.; Cifuentes, A., Chiral electromigration methods in food analysis. *Electrophoresis* **2003,** *24*, 2431-2441.

3. McConnell, O.; Bach, A.; Balibar, C.; Byrne, N.; Cai, Y.; Carter, G.; Chlenov, M.; Di, L.; Fan, K.; Goljer, I., *et al.*, Enantiomeric Separation and Determination of Absolute Stereochemistry of Asymmetric Molecules in Drug Discovery: Building Chiral Technology Toolboxes. *Chirality* **2007,** *19*, 658-682.

4. Zhang, J.; Albelda, M. T.; Liu, Y.; Canary, J. W., Chiral Nanotechnology. *Chirality* **2005,** *17*, 404-420.

5. Haupert, L. M.; Simpson, G. J., Chirality in Nonlinear Optics. *Annu. Rev. Phys. Chem.* **2009,** *60*, 345-365.

6. Noyori, R., Asymmetric Catalysis: Science and Opportunities (Nobel Lecture). *Angew. Chem. Int. Ed. Engl.* **2002,** *41* (12), 2008-2022.

7. De Boni, L.; Toro, C.; Hernandez, F. E., Synchronized Double L-Scan Technique for the Simultaneous Measurement of Polarization-Dependent Two-Photon Absorption in Chiral Molecules. *Opt. Lett.* **2008,** *33*, 2958-2960.

8. Tinoco, I., Two-Photon Circular Dichroism. *J. Chem. Phys.* **1975,** *62*, 1006-1009.

9. Power, E. A., Two-Photon Circular Dichroism. *J. Chem. Phys.* **1975,** *63*, 1348-1350.

10. Jansik, B.; Rizzo, A.; Agren, H., Response Theory Calculations of Two-Photon Circular Dichroism. *Chem. Phys. Lett.* **2005,** *414*, 461-467.

11. Toro, C.; De Boni, L.; Lin, N.; Santoro, F.; Rizzo, A.; Hernandez, F. E., Two-Photon Absorption Circular Dichroism: A New Twist in Nonlinear Spectroscopy. *Chem. Eur. J.* **2010,** *16*, 3504-3509.

12. Rizzo, A.; Jansík, B.; Pedersen, T. B.; Agren, H., Origin Invariant Approaches to the Calculation of Two-Photon Circular Dichroism. *J. Chem. Phys.* **2006,** *125*, 64113.

13. Jansík, B.; Rizzo, A.; Agren, H., Ab Initio Study of the Two-Photon Circular Dichroism in Chiral Natural Amino Acids. *J. Phys. Chem. B* **2007,** *111*, 446-460.

14. Jansík, B.; Rizzo, A.; Ågren, H.; Champagne, B., Strong Two-Photon Circular Dichroism in Helicenes: A Theoretical Investigation. *J. Chem. Theory Comput.* **2008,** *4*, 457-467.

15. Rizzo, A.; Lin, N.; Ruud, K., Ab Initio Study of the One- and Two-Photon Circular Dichroism of R-(+)-3-Methyl-Cyclopentanone. *J. Chem. Phys.* **2008,** *128*, 164312.

16. Lin, N.; Santoro, F.; Rizzo, A.; Luo, Y.; Zhao, X.; Barone, V., Theory for Vibrationally Resolved Two-Photon Circular Dichroism Spectra. Application to (R)-(+)-3-Methylcyclopentanone. *J. Phys. Chem. A* **2009,** *113*, 4198-4207.

17. Guillaume, M.; Ruud, K.; Rizzo, A.; Monti, S.; Lin, Z.; Xu, X., Computational Study of the One- and Two-Photon Absorption and Circular Dichroism of (L)-Tryptophan. *J. Phys. Chem. B* **2010,** *114*, 6500-6512.

18. Petrovic, A. N. A. G.; Vick, S. E.; Polavarapu, P. L., Determination of the Absolute Stereochemistry of Chiral Biphenanthryls in Solution Phase Using Chiroptical Spectroscopic Methods :. *Chirality* **2008,** *510*, 501-510.

19. Polavarapu, P. L.; Petrovic, A. G.; Vick, S. E.; Wulff, W. D.; Ren, H.; Ding, Z.; Staples, R. J., Absolute Configuration of 3, 3′-Diphenyl-[2, 2′-binaphthalene]-1, 1′-diol Revisited. *J. Org. Chem.* **2009,** *74* (15), 5451-5457.

20. Becke, A. D., Density-Functional Exchange-Energy Approximation with Correct Asymptotic Behavior. *Phys. Rev. A* **1988,** *38*, 3098-3100.

21. Becke, A. D., Density-Functional Thermochemistry. III. The Role of Exact Exchange. *J. Chem. Phys.* **1993,** *98*, 5648-5652.

22. Lee, C.; Yang, W.; Parr, R. G., Development of the Colle-Salvetti Correlation-Energy Formula into a Functional of the Electron Density. *Phys. Rev. B: Condens. Matter* **1988,** *37*, 785-789.

23. Rassolov, V. A.; Pople, J. A.; Ratner, M. A.; Windus, T. L., 6-31G* Basis Set for Atoms K through Zn. *J. Chem. Phys.* **1998,** *109*, 1223-1229.

24. Frisch, M. J.; Trucks, G. W.; Schlegel, H. B.; Scuseria, G. E.; Robb, M. A.; Cheeseman, J. R.; Scalmani, G.; Barone, V.; Mennucci, B.; Petersson, G. A., *et al.*, Gaussian 09, Revision A.1. Gaussian, Inc.: Wallingford CT, 2009.

25. Mennucci, B.; Tomasi, J.; Cammi, R.; Cheeseman, J. R.; Frisch, M. J.; Devlin, F. J.; Gabriel, S.; Stephens, P. J., Polarizable Continuum Model (PCM) Calculations of Solvent Effects on Optical Rotations of Chiral Molecules. *J. Phys. Chem. A* **2002,** *106*, 6102-6113.

26. Tomasi, J.; Mennucci, B.; Cammi, R., Quantum Mechanical Continuum Solvation Models. *Chem. Rev.* **2005,** *105*, 2999-3093.

27. Runge, E.; Gross, E. K. U., Density-Functional Theory for Time-Dependent Systems. *Phys. Rev. Lett.* **1984,** *52*, 997-1000.

28. Dierksen, M.; Grimme, S., A Theoretical Study of the Chiroptical Properties of Molecules with Isotopically Engendered Chirality. *J. Chem. Phys.* **2006,** *124*, 174301.

29. Yanai, T.; Tew, D. P.; Handy, N. C., A new Hybrid Exchange-Correlation Functional using the Coulomb-Attenuating Method (CAM-B3LYP). *Chem. Phys. Lett.* **2004,** *393*, 51-57.

30. Peach, M. J. G.; Helgaker, T.; Sałek, P.; Keal, T. W.; Lutnaes, O. B.; Tozer, D. J.; Handy, N. C., Assessment of a Coulomb-attenuated exchange-correlation energy functional. *Phys. Chem. Chem. Phys.* **2006,** *8*, 558-562.

31. DALTON *A Molecular Electronic Structure Program, Release Dalton 2.0, see* *http://www.kjemi.uio.no/software/dalton/dalton.html*, 2005.

32. Lin, N.; Santoro, F.; Zhao, X.; Toro, C.; De Boni, L.; Hernández, F. E.; Rizzo, A., Computational Challenges in Simulating and Analyzing Experimental Linear and Nonlinear Circular Dichroism Spectra. R-(+)-1,1'-bis(2-naphthol) as a Prototype Case. *J. Phys. Chem. B* **2011,** *115*, 811-824.

33. Loncaric, C.; Wulff, W. D., An Efficient Synthesis of (-)-Chloramphenicol via Asymmetric Catalytic Aziridination: A Comparison of Catalysts Prepared from Triphenylborate and Various Linear and Vaulted Biaryls. *Org. Lett.* **2001,** *3* (23), 3675-3678.

34. Toro, C.; De Boni, L.; Lin, N.; Santoro, F.; Rizzo, A., Two-Photon Absorption Circular-Linear Dichroism on Axial Enantiomers. *Chirality* **2010,** *22*, E202-E210.

35. Woody, R. W., The Exciton model and the circular dichroism of polypeptides. *Monatsh. Chem.* **2005,** *136*, 347-366.

36. Di Bari, L.; Pescitelli, G.; Salvadori, P., Conformational study of 2,2 '-homosubstituted 1,1 '-binaphthyls by means of UV and CD spectroscopy. *J. Am. Chem. Soc.* **1999,** *121*, 7998-8004.

37. Zhang, S.; Zhang, H.; Lu, C.; Jia, T.; Wang, Z.; Sun, Z., Mechanism of Polarization-Induced Single-Photon Fluorescence Enhancement. *J. Chem. Phys.* **2010,** *133* (21), 214504.

38. Nag, A.; Goswami, D., Polarization Induced Control of Single and Two-Photon Fluorescence. *J. Chem. Phys.* **2010,** *132* (15), 154508.

39. Nalwa, H. S.; Miyata, S., *Nonlinear Optics of Organic Molecules and Polymers*. CRC press: 1996.

40. Petrovic, A. G.; Vick, S. E.; Polavarapu, P. L., Determination of the Absolute Stereochemistry of Chiral Biphenanthryls in Solution Phase Using Chiroptical Spectroscopic Methods: 2, 2′-Diphenyl-[3, 3′-biphenanthrene]-4, 4′-diol. *Chirality* **2008,** *20* (3-4), 501-510.

41. Calvert, R. L.; Ritchie, G. L., Molecular Quadrupole Moment of Naphtalene. *J.C.S. Faraday II* **1980,** *76*, 1249-1253.

42. Nobusada, K.; Yabana, K., Photoinduced Eelectric Currents in Ring-Shaped Molecules by Circularly Polarized Laser Pulses. *Phys. Rev. A* **2007,** *75* (3), 032518.

43. Skourtis, S.; Beratan, D.; Naaman, R.; Nitzan, A.; Waldeck, D., Chiral Control of Electron Transmission through Molecules. *Phys. Rev. Lett.* **2008,** *101* (23), 238103.

CHAPTER 3 : OVERCOMING THE EXISTENT COMPUTATIONAL CHALLENGES IN THE AB-INITIO CALCULATIONS OF THE TWO-PHOTON CIRCULAR DICHROISM SPECTRA OF LARGE MOLECULES USING A FRAGMENT-RECOMBINATION APPROACH

Reproduced with permission of Elsevier from: C. Diaz, L. Echevarria, F.E. Hernández, Chem. Phys. Lett. ***2013****, 568-569, 176-183.*

In addition to understanding the effect of the twist in the π–electron delocalization of chiral molecules on the TPCD spectra of aryl derivatives, in Chapter I we found challenging to perform calculations of TPA and TPCD spectra in large molecules.

In order to surmount the uncovered barrier in the calculation of the TPCD spectra of more complex molecules, in this chapter we present an innovative method called the fragment-recombination approach (FRA) for the calculation of the TPCD spectra of such systems. In order to demonstrate the principle of FRA-TPCD we selected two molecular systems with increased size and complexity from the same group of chiral biaryl derivatives studied before. Although, FRA-TPCD is subject to strict fragmentation rules, following the proposed protocol to calculate the corresponding TPCD spectra of the different fragments one can reconstruct the full TPCD spectrum of the whole molecule at a lower computational cost. Additionally, this novel approach allows to identifying and assigning the structural origin of the different spectral features.

3.1 Introduction

We have already discuss through this dissertation the unique possibilities TPCD bring to the community to perform novel structural and conformational studies of biological and chemical chiral systems at shorter wavelengths, i.e. within the near and far UV region. We have also highlighted, the experimental and theoretical contributions to the TPCD field accomplished by Hernandez and co-workers, mainly in catalysts with axial chirality. [1, 2] However, all their studies have been restricted to relatively small molecules due to the computational challenges found in the determination of this nonlinear chiroptical property.

With the aim of uncovering the full potential of TPCD for the determination of the structural conformation of large chiral molecules, we have developed a fragment-recombination approach (FRA) that allows overcoming the existent computational challenges found throughout the calculation of the TPCD spectrum of large molecules. In this chapter we present the description of FRA and demonstrate its direct application on two different molecules, one with two fragments exhibiting axial chirality, and one with a combination of entities with axial and propeller chirality. The comparative theoretical analysis of the TPCD spectra of the corresponding fragments with that of the full molecule proves that TPCD is an additive property. This characteristic permits, as shown next, to identifying the origin of the different spectral features observed in the TPCD spectrum of the entire molecule from those on its segments. This approach is expected to find great applications in the structural analysis of large catalysts and polypeptides.

3.2 Computational Methods.

The theoretical background involved in this research has been given in detail in references 3-8 and is also presented in sections 1.2 and 1.5 of the introduction to this dissertation. Therefore, in this part we only present the computational details relevant to the corresponding calculations.

The molecular structure of the two molecules and their corresponding fragments (see Figures 3-2.a and 3-2.b) were optimized using Density Functional Theory (DFT) [9, 10] − employing the Becke's three-parameter exchange, Lee, Yang and Parr correlation (B3LYP) hybrid functional [11-13] − in conjunction with the 6-31G* basis set [14] − using Gaussian 09. [15] The TPA and TPCD response for the lowest 30 electronic excited states of all optimized structures were computed using Time-Dependent DFT (TD-DFT) [9, 10] at the same level of theory as for the geometry optimizations using Dalton 2011. [16] All the calculations were carried out *in vacuo*. The convolution of the TPA and TPCD spectra were obtained employing Equations 1-18 and 1-37 (See dissertation introduction), respectively, using a normalized Lorentzian lineshape (See Equation 1-15 in dissertation introduction) with $\Gamma = 0.15$ eV (FWHM).

3.2.1 Fragment-recombination approach (FRA)

The method described next allows overcoming the computational challenges present when modeling the TPCD spectrum of large molecules, and opens a new possibility for performing the structural analysis of large chiral systems through the calculation of this nonlinear chiroptical property on independent chiral constituent fragments of the entire molecule.

Figure 3-1 displays, in three general steps, the required protocol to apply FRA to large chiral systems. In this general example the molecular arrangement consists of four different chiral entities (A, B, C and D) bound together through not optically active moieties that avoid π–electron delocalization through the entire molecule.

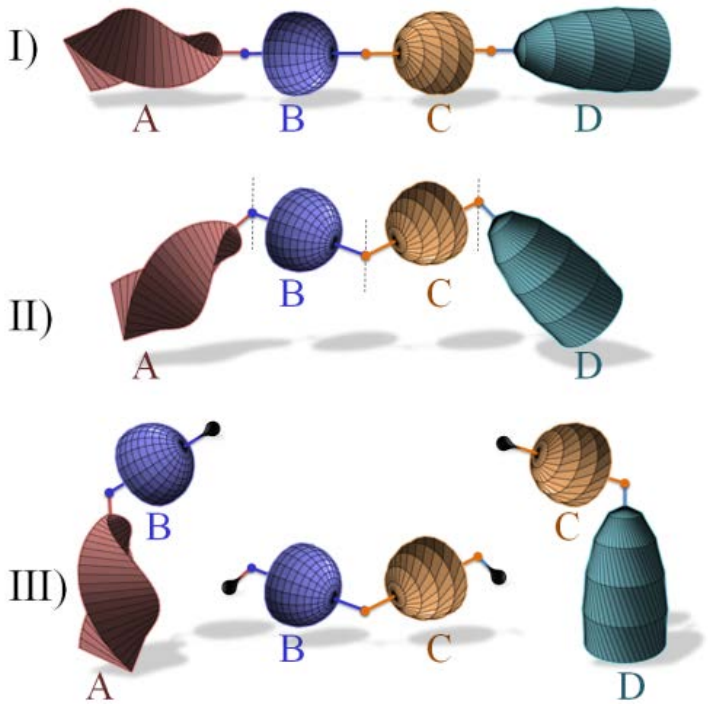

Figure 3-1. Schematic of the three main steps in FRA: Initial structure of molecule of interest (I), Optimized molecular structure of the entire system (II), "Conditional" fragmentation of the optimized molecular structure (III). A, B, C and D represent four unspecific chiral entities.

The general steps to follow when applying FRA are: 1) Build the structure of the molecule of interest (I). In this initial step the molecular structure has not yet been optimized, therefore, dihedral angles, bond distances and relative group positions are far from their final configuration. 2) Optimization of the molecular structure of the whole system (II). In this subsequent step the molecular structure is taken to its final lowest energy state, thus it is in its finest structural configuration. 3) "Conditional" fragmentation of the optimized molecular

structure (III). The application of this final step is restrictive with respect to the following points: i) In order to avoid an artificial spectral blue-shift on the TPCD spectrum of the fragments, the original π–electron delocalization should not be broken (distorted) in molecules with extended electron conjugation. Incurring in this severe artifact would not allow to directly combine the various contributions from the TPCD rotatory strength of the different fragments to reconstruct that of the complete molecule. ii) The relative position of the moieties, as well as the original dihedral angles between fragments should remain intact in each segment after step (2) has been completed. Because TPCD is very susceptible to the structural conformation of chiral molecules, not fulfilling this condition will lead to the calculation of the TPCD spectrum of misrepresented fragments. Therefore, geometry re-optimization of the fragments should be avoided at this stage of FRA. iii) The existent overall and partial chirality in the full molecule must continue in the corresponding fragments (A, B, C, D). This important restriction guarantees the presence of their respective contributions to the TPCD spectrum of the entire molecule. It also allow to accounting for multiple chiral moieties in large molecules. iv) On this last stage of the procedure, the removed segments should be replaced by functional groups that are passive to the overall electronic properties of the residual fragment subject to study. This is common practice in computational chemistry when trying to reduce the complexity of a system without modifying its equilibrium geometry and electronic properties.

After completing the systematic fragmentation of the whole molecule using FRA, one proceeds to calculate, independently, the TPCD spectra of all the fragments. With the corresponding stick-spectra of the segments, a direct addition of all them, respecting the relative proportions of the fragments in the full molecule, is performed. This procedure guarantee taking into account the contribution of repeated segments, weighted through their corresponding TPCD

rotational strength contribution, to the overall TPCD spectrum of the entire molecule. Finally, a normalized Lorentzian lineshape function with a linewidth (Γ) is applied to all transitions in the TPCD spectrum of each segment in order to reproduce the corresponding theoretical TPCD spectrum of the original (large) molecule. This generalized approximation could introduce some errors in the determination of the TPCD spectrum of the complete molecule since all transitions does not necessarily contribute the same way in every single fragment. Nevertheless, this approximation does not seem to affect significantly the anticipated performance of FRA on the molecules studied so far. Further studies in this direction are in progress.

3.3 Results and discussion

In order to test FRA, we calculated the TPCD spectra of two relatively large molecules M1 and M2, i.e. (S,S)-spiro[8.8]4,5(1,2),13,14(2,3)-tetranaphtalenaheptadecane and (Δ,S)-(1,1′-binaphthalene-2,2′diolato)(bis(1,2-benzenediolato)sulfate(VI)), respectively. While M1 was chosen because of our previous studies on S-BINOL and S-VANOL, [1, 2] M2 was selected because of its structural similarity with BINPHAT, a well-studied asymmetric chiral catalyst with hexacoordinated chemistry. [17]

Figures 3-2 and 3-3 display the molecular structures of M1 and M2, respectively, as well as those of their corresponding fragments.

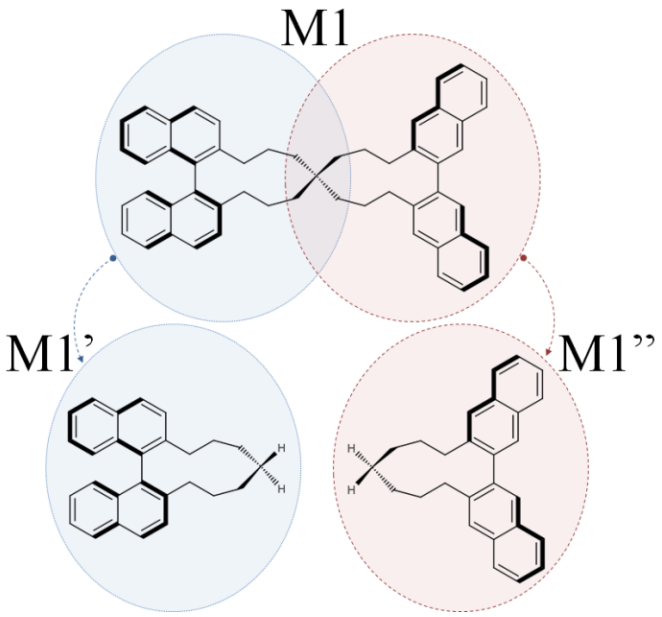

Figure 3-2. Molecular structures of M1 (top), M1' (left bottom corner) and M1" (right bottom corner).

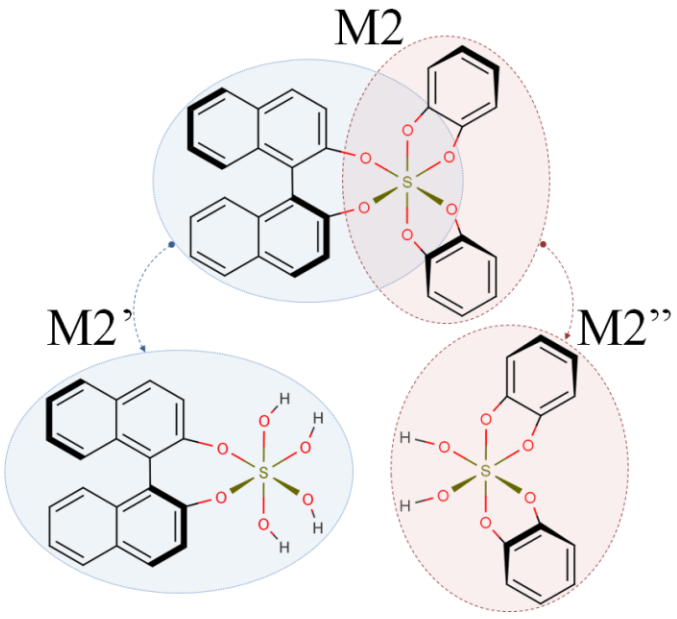

Figure 3-3. Molecular structures of M2 (top), M2' (left bottom corner) and M2" (right bottom corner).

As one can notice, M1 and M2 were disjointed at the center where the dissociation of the whole molecule does not considerably alter their electronic properties. The resultant portions in M1 are two different optically active biaryl derivatives with axial chirality, i.e. the (S)-4,5(1,2)-binaphtalena (M1') and the (S)-13,14(2,3)-binaphtalena (M1") fragments. M2 was split around the sulfur to generate the (Δ)-bis(1,2-benzenediolato) (M2') segment and that with the (S)- 1,1′-binaphthalene-2,2′diolato (M2") fragment. In M1' and M1" the terminal groups were substituted by hydrogen and in M2 and M2" the moieties were substituted by hydroxyls groups (−OH). Interesting to highlight is the fact that while in M1 the contribution to the overall chirality of the large molecule only derives from M1' and M1", in M2 the center also contributes to the total optical activity of the entire molecule through its propeller chirality. The molecular structure optimizations of the entire molecules were performed according to the theoretical and computational methods described above. The generation of the fragments was performed according to step (3) in FRA.

In Figure 3-4 we show the stick and convoluted TPCD spectra of M1' (a), M1" (b), M1 (d), and the addition of the TPCD spectra of M1'and M1" (c), all calculated independently. First thing to notice is the existent differences between the spectra of M1' and M1" (see Figure 3-4.a and II-4.b). On the one hand, it can be observed that in M1 the most important transitions, contributing with negative TPCD rotatory strength, are those to excited states 2 and 6−8, while in M1" are those to excited states 2, 7, 9 and 10. On the other hand, it can be noticed that the most important contribution of the TPCD rotatory strength, with positive sign, is that to excited state 5 in M1, and that to excited state 3 in M1". These differences complement each other on the TPCD-FRA spectrum of M1. As shown in Figure 3-4.c, the TPCD rotatory strength of the

dominant transitions add up respecting their corresponding signs to reconstructing subsequently the overall TPCD spectrum of the large molecule.

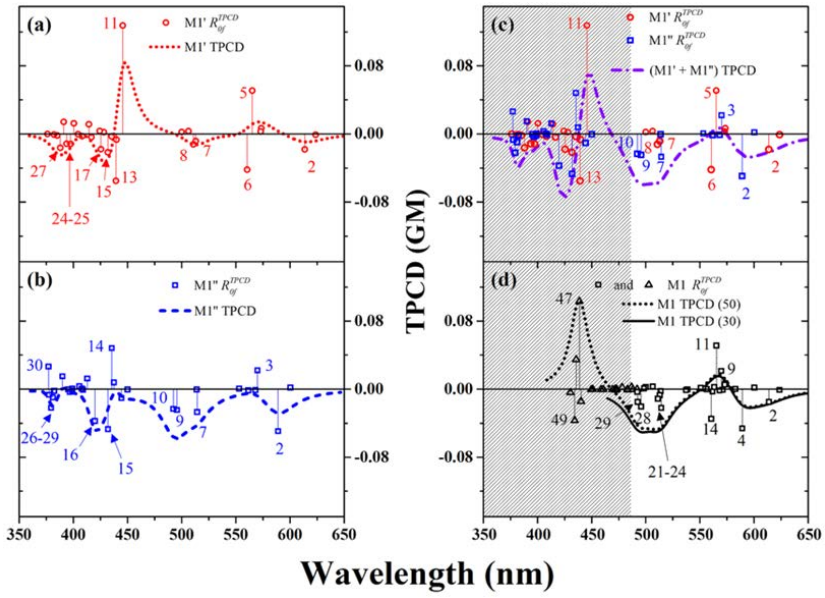

Figure 3-4. Theoretical TPCD stick and convoluted (lines) spectra of M1' (a), M1" (b), M1'+M1" (c), and M1 (d). The TPCD-FRA spectra shown in (c) was generated by directly adding the TPCD stick spectra of M1' and M1". All spectra are plotted with respect to the TPA excitation wavelength.

In addition, since the mentioned transitions contribute independently to the spectrum of the complete molecule, one can identify the contribution of each fragment to the overall nonlinear chiroptical property of M1. The direct comparison between the spectra shown in Figure 3-4.c and 3-4.d reveals the correspondence between the preponderant transitions in M1' and M1" and the dominant transitions in M1 (see Table 3-1). It also exhibits a virtually perfect match between both spectra. This is the result of the additivity of the TPCD rotatory strength generated by the fragments. This valuable piece of information allows to recognizing the origin of the specific spectral fingerprints on the TPCD spectrum of M1. The spectral agreement corroborates that FRA is indeed a reliable method for studying TPCD in large molecules. In

addition, because calculations done on fragments are less demanding in terms of computational cost, and because the separation between excited states in those shorter segments is larger, applying FRA allows gaining access to TPCD fingerprints at shorter wavelengths, a region that is not affordable by the direct calculation on the entire molecule. This statement is supported by the additional spectral region 360 nm − 480 nm, highlighted on Figure 3-4.c compared to Figure 3-4.d, which was obtained employing FRA using 30 excited states (see shadowed area,). The features observed in this region are mainly determined by the contributions of higher energy excited states in M1' and M1" (see Table 3-1). Even in the event where calculations were done on the maximum number of excited states allowed by our computational resources on M1 (50 excited states - dotted line) the TPCD spectrum of the entire molecule only covers a region between 420 nm to 640 nm.

Table 3-1. Assignment of the predominant transitions that define the main positive and negative TPCD bands in M1' and M1", and with a direct correspondence with those obtained in M1. Values in parenthesis at the bottom of the table correspond to transitions present in a spectral region only accessible by TPCD-FRA.

Wavelength (nm)	**Excited States**		
	M1	M1'	M1''
614	2	2	-
589	4	-	2
567	9, 11	5	3
560	14	6	-
510	21-24	7-8	7
495	28-29	-	9-10
(446)	-	11	14
(425)	-	13, 15, 17	15, 16
(383)	-	24, 25, 27	26-29, 30

This demonstrates the benefit of using FRA in large systems. Because calculations on the two fragments can still afford the inclusion of more than 30 excited states, the computation of the TPCD spectrum of M1 using FRA can provide more spectral information farther into the UV region. Considering the reduced computational cost afforded by the proposed method, FRA opens a path to using larger basis sets and more thorough functionals on molecules (large or small) where the computational cost on the entire molecule exceeds the limits of the resources. All these advantages combined can help improve the accuracy on the calculation of this nonlinear chiroptical property in optically active molecules and macromolecules.

In order to expand our analysis we extended the study to a molecule with axial and propeller chirality (see Figure 3-3). This type of molecules can also present an important charge transfer. Figure 3-5 present the stick and convoluted TPCD spectra of M2' (a), M2" (b), M2 (d), and the addition of the TPCD spectra of M2' and M2" (c), all calculated independently. Again, differences between the TPCD spectra of the fragments (M2' and M2") are present (see Figure 3-5.a and 3-5.b). Interesting to highlight in this specific example is the fact that the amplitude of the TPCD spectrum of M2' is approximately 10 fold larger that of M2". This result suggests, as confirmed later, that the expected TPCD spectrum of the entire molecule should be mainly determined by the overwhelming contributions of M2'. Nevertheless, one can still review the transitions on M2" with negative and positive TPCD rotatory strength (see inset, Figure 3-5.b) in parallel with those in M2'. The most important transitions in M2', contributing with negative TPCD rotatory strength, are those to excited states 3-6, while in M2" are 3, 4, 5 and 7. The predominant contributions of the TPCD rotatory strength of M2', with positive sign, are those to excited states 1, 9, 10, 11, 15 and 16, and none in M2". Figure 3-5.c, shows the sum of TPCD spectra of M2' and M2". As anticipated, the TPCD spectrum of M2 is indeed strongly dominated

by the contributions of the TPCD rotatory strength of M2'. This result evidence the independent contribution of different moieties and their corresponding chirality to the total TPCD signal, and corroborate the additive of the property which reproduces the TPCD spectrum of the complete molecule.

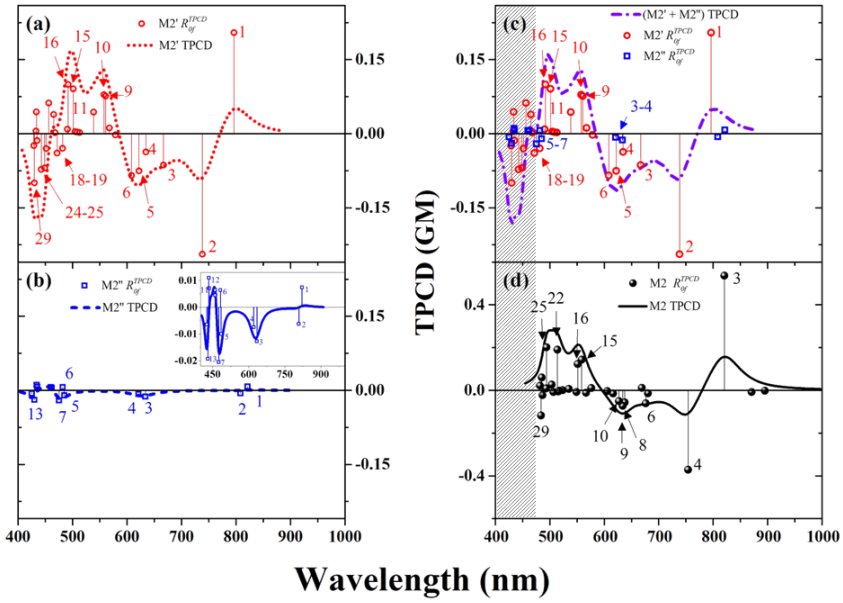

Figure 3-5. Theoretical TPCD stick and convoluted (lines) spectra of M2' (a), M2" (b), M2'+M2" (c), and M2 (d). The TPCD-FRA spectra shown in (c) was generated by directly adding the TPCD stick spectra of M1' and M1". All spectra are plotted with respect to the TPA excitation wavelength.

In addition, because TPCD is an additive function, one can identify the individual contributions from each fragment on the TPCD spectrum of the entire molecule. The direct comparison between Figure 3-5.c and 3-5.d reveals an excellent correspondence between dominant transitions in M2' and M2" and those in M2 (see Table 3-2). This correlation results in an excellent match between the two spectra. However, a small difference between their maximum amplitude and a slight spectral blue shift of 24 nm on M2' compared to M2 can be noticed. This outcome is attributed to apparent differences in intramolecular charge transfer (ICT) in the entire molecule compared to that in the fragments. In order to prove our hypothesis,

in Figure 3-6, we show the molecular orbitals corresponding to the two main transitions on the red side of the spectrum, i.e. those to excited states 1 and 2 in M2' and, 3 and 4 in M2. It can be observed that ICT in M2' is truncated at the hydroxyl moieties on the clear side of the sulfur while in M2 it can be transferred even further into the phenyl rings. In addition, TPCD is a property that is very sensitive to the structural conformation of chiral systems. Therefore, the absence of the missing fragment in the two independent portions could have an effect on the amplitude of the signal due to long range van der Walls interactions (dipole-dipole or quadrupole-quadrupole). This effect become more important when the different chiral moieties are placed at a close enough distance to feel the field effect of each other, on each other (Further studies in this direction are in progress).

Table 3-2. Assignment of the predominant transitions that define the main positive and negative TPCD bands in M2' and M2", and with a direct correspondence with those obtained in M2. Values in parenthesis at the bottom of the table correspond to transitions present in a spectral region only accessible by TPCD-FRA.

Wavelength (nm)	**Excited States**		
	M2	M2'	M2''
820	3	1	-
753	4	2	-
679	6	3	-
631	8-10	5-6	3-4
556	15-16	9-10	-
502	22-25	15-16	-
482	29	18-19	5-7
(437)	-	24, 25, 29	13

Finally, in M2 we have reconfirmed the potential of FRA to predicting more spectral features in the blue – UV region. Calculations over 30 excited states (see shadowed area, Figure 3-5.c and 3-5.d) with FRA provide TPCD fingerprints down to 400 nm. Features observed in those extra 80 nm are mainly determined by the contributions of excited states 24, 25 and 29 in

M2’ and excited states 13 in M2” (see Table 3-2). Of course, FRA allows to going below 400 nm through the inclusion of more excited states in M2’ and M2”, a calculation not affordable for M2.

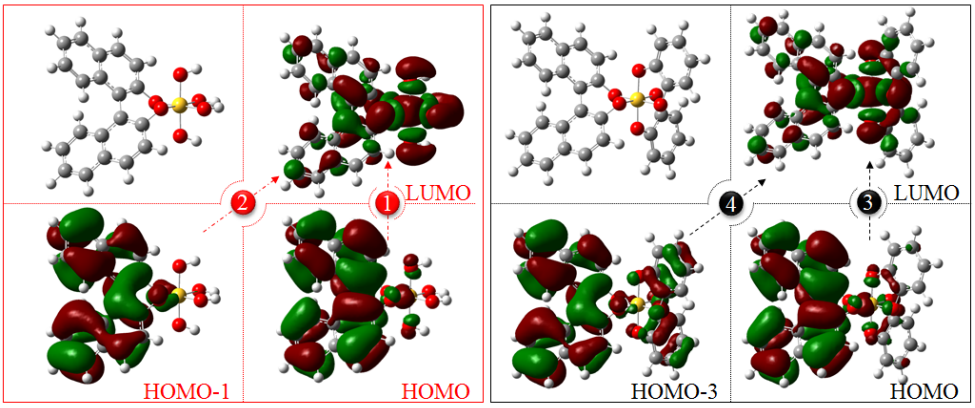

Figure 3-6. Molecular orbitals of M2’ (left) and M2 (right). Calculated using Gaussian 09[35] at the B3LYP/6-31G* level of theory *in vacuo*. The arrows-numbered balls represent transitions 1 and 2 in M2’ and transition 3 and 4 in M2.

To finish with this analysis, we would like to present the applicability of FRA to TPA as well. Figure 3-7 and Figure 3-8 present the theoretical TPA spectra of M1 and M2, respectively, and those of their corresponding fragments. As observed in TPCD, TPA-FRA confirmed the additive property of TPA and allows assigning specific transitions to the different segments that form the entire molecule. The comparison of the TPA spectra, calculated on the entire molecules M1 and M2, with those obtained, in each case, applying FRA help supports this statement. The first thing to notice is the similarity between the TPA spectra in both molecules. The fact that the spectral match is better in M1 (Figure 3-7) than in M2 (Figure 3-8) is not totally unexpected considering the relative weak interaction between the two fragments in M1 compared to M2. Nevertheless, TPA-FRA reproduces very well the TPA of M2. The observed minor differences in the latter are attributed to the strong intramolecular charge-transfer present in M2 which is not

fully considered through the separate analysis of the segments. This effect was also observed in the TPCD-FRA of this molecule.

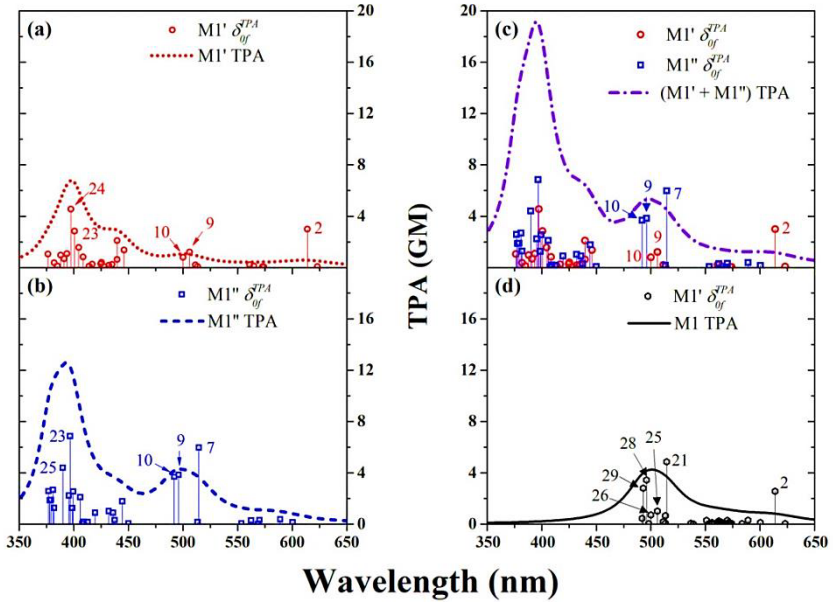

Figure 3-7. Theoretical TPA stick and convoluted (lines) spectra of M1' (a), M1" (b), M1'+M1" (c), and M1 (d). The TPA-FRA spectra shown in (c) was generated by directly adding the TPA stick spectra of M1' and M1". All spectra are plotted with respect to the TPA excitation wavelength.

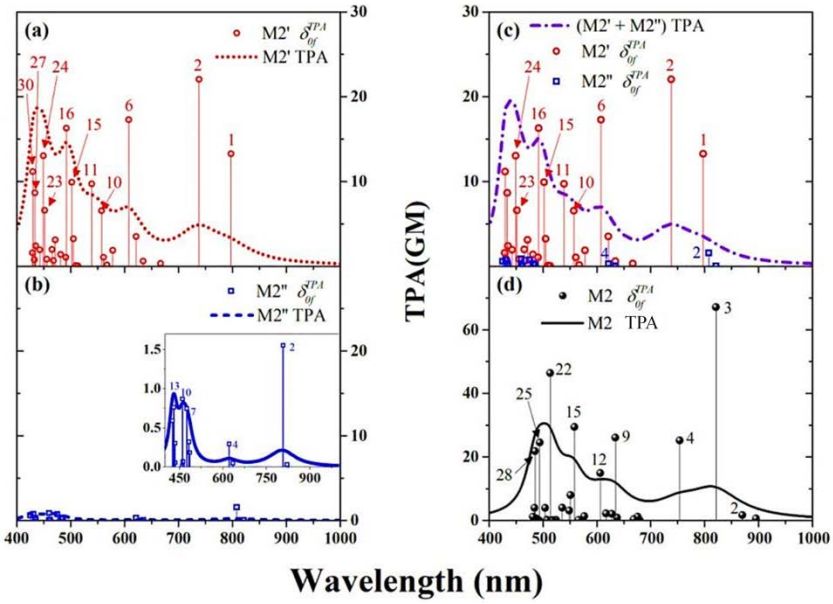

Figure 3-8. Theoretical TPA stick and convoluted (lines) spectra of M2' (a), M2" (b), M2'+M2" (c), and M2 (d). The TPA-FRA spectra shown in (c) was generated by directly adding the TPA stick spectra of M1' and M1". All spectra are plotted with respect to the TPA excitation wavelength.

The careful examination of the TPA spectra of M1 shown in Figure 3-7, reveal the correspondence between transitions to excited states 2, 9, 10 in M1' and those to excited states 2, 25, 26 in M1, and transitions to excited states 7, 9 and 10 in M1" and those to excited states 21, 28 and 29 in M1. This direct assignment evidence the potential of TPA-FRA to identifying the origin and contributions of different transitions of the fragments to the TPA spectrum of the entire molecule. Similarly, the cautious inspection of Figure 3-8 shows the connection between transitions to excited states 1, 2, 5, 6, 11 and 16 in M2' and those to excited states 3, 4, 9, 12, 15 and 22 in M2. Because of its small TPA cross-section, M2" does not strongly contribute to the TPA spectrum of M2, at least within the spectral range under study (400 nm – 1000 nm). Although, the overall shape of the TPA spectra of M2 obtained using FRA and calculated directly on the complete molecule is very similar, the relative intensities of certain transitions in M2', e.g. 1 and 2, and 9 and 12, are inverted in M2, i.e. 3 and 4, and 9 and 12. This behavior, which was not observed in TPCD-FRA, is attributed to existent differences in superposition of basis set functions in the fragments compared to that in the whole molecule. This result indicates, *a priori*, that TPA-FRA is more susceptible to effects of electron-correlation than TPCD-FRA.

3.4 Conclusions

We have shown, theoretically, a new powerful and reliable method for determining the TPCD spectrum of chiral molecules that allows performing the recognition of specific spectral features and the origin of spectral fingerprints on the TPCD spectrum of large optically active systems. We verified that this method can also be applied to the calculation and analysis of the TPA spectra of extended systems. We have demonstrated that calculations using FRA affords the efficient use of computing resources, thus offering the possibility to perform structural analysis

of chiral systems over a broader spectral range. We have revealed the capability of FRA to using larger basis sets and more thorough functionals on large and small molecules where the computational cost exceeds the limits of the resources. However, experimental evidence that certifies the application of FRA-TPCD to large, highly conjugated, chiral complex molecules is needed before arriving to any further solid conclusions. Proving this last point will open new opportunities in the conformational analysis and characterization of biological macromolecules such as peptides, polypeptides and proteins in a spectral region that is obscure for standard ECD.

3.5 References

1. Toro, C.; De Boni, L.; Lin, N.; Santoro, F.; Rizzo, A.; Hernandez, F. E., Two-Photon Absorption Circular Dichroism: A New Twist in Nonlinear Spectroscopy. *Chem. Eur. J.* **2010,** *16*, 3504-3509.

2. Diaz, C.; Lin, N.; Toro, C.; Passier, R.; Rizzo, A.; Hernández, F. E., The Effect of the π-Electron Delocalization Curvature on the Two-Photon Circular Dichroism of Molecules with Axial Chirality. *J. Phys. Chem. Lett.* **2012,** *3*, 1808-1813.

3. Rizzo, A.; Jansík, B.; Pedersen, T. B.; Agren, H., Origin Invariant Approaches to the Calculation of Two-Photon Circular Dichroism. *J. Chem. Phys.* **2006,** *125*, 64113.

4. Jansík, B.; Rizzo, A.; Agren, H., Ab Initio Study of the Two-Photon Circular Dichroism in Chiral Natural Amino Acids. *J. Phys. Chem. B* **2007,** *111*, 446-460.

5. Jansík, B.; Rizzo, A.; Ågren, H.; Champagne, B., Strong Two-Photon Circular Dichroism in Helicenes: A Theoretical Investigation. *J. Chem. Theory Comput.* **2008,** *4*, 457-467.

6. Rizzo, A.; Lin, N.; Ruud, K., Ab Initio Study of the One- and Two-Photon Circular Dichroism of R-(+)-3-Methyl-Cyclopentanone. *J. Chem. Phys.* **2008,** *128*, 164312.

7. Lin, N.; Santoro, F.; Rizzo, A.; Luo, Y.; Zhao, X.; Barone, V., Theory for Vibrationally Resolved Two-Photon Circular Dichroism Spectra. Application to (R)-(+)-3-Methylcyclopentanone. *J. Phys. Chem. A* **2009,** *113*, 4198-4207.

8. Guillaume, M.; Ruud, K.; Rizzo, A.; Monti, S.; Lin, Z.; Xu, X., Computational Study of the One- and Two-Photon Absorption and Circular Dichroism of (L)-Tryptophan. *J. Phys. Chem. B* **2010,** *114*, 6500-6512.

9. Runge, E.; Gross, E. K. U., Density-Functional Theory for Time-Dependent Systems. *Phys. Rev. Lett.* **1984,** *52*, 997-1000.

10. Dierksen, M.; Grimme, S., A Theoretical Study of the Chiroptical Properties of Molecules with Isotopically Engendered Chirality. *J. Chem. Phys.* **2006,** *124*, 174301.

11. Becke, A. D., Density-Functional Exchange-Energy Approximation with Correct Asymptotic Behavior. *Phys. Rev. A* **1988,** *38*, 3098-3100.

12. Becke, A. D., Density-Functional Thermochemistry. III. The Role of Exact Exchange. *J. Chem. Phys.* **1993,** *98*, 5648-5652.

13. Lee, C.; Yang, W.; Parr, R. G., Development of the Colle-Salvetti Correlation-Energy Formula into a Functional of the Electron Density. *Phys. Rev. B: Condens. Matter* **1988,** *37*, 785-789.

14. Rassolov, V. A.; Pople, J. A.; Ratner, M. A.; Windus, T. L., 6-31G* Basis Set for Atoms K through Zn. *J. Chem. Phys.* **1998,** *109*, 1223-1229.

15. Frisch, M. J.; Trucks, G. W.; Schlegel, H. B.; Scuseria, G. E.; Robb, M. A.; Cheeseman, J. R.; Scalmani, G.; Barone, V.; Mennucci, B.; Petersson, G. A., *et al.*, Gaussian 09, Revision A.1. Gaussian, Inc.: Wallingford CT, 2009.

16. DALTON *A Molecular Electronic Sstructure Program, Release Dalton 2011, see* *http://daltonprogram.org/*, 2011.

17. Lacour, J.; Londez, A.; Goujon-Ginglinger, C.; Buss, V.; Bernardinelli, G., Configurational Ordering of Cationic Chiral Dyes Using a Novel C 2-Symmetric Hexacoordinated Phosphate Anion. *Org. Lett.* **2000,** *2* (26), 4185-4188.

CHAPTER 4 : CONFORMATIONAL STUDY OF AN AXIALLY CHIRAL SALEN LIGAND IN SOLUTION USING TWO-PHOTON CIRCULAR DICHROISM AND THE FRAGMENT-RECOMBINATION APPROACH

Reproduced with permission of the American Chemical Society from: C. Díaz, L. Echevarria, F.E. Hernández, J. Phys. Chem. A ***2013****, 117, 8416-8426.*

Through the development of a novel conditional fragmentation recombination approach in Chapter II, we demonstrated the capabilities of FRA-TPCD to perform conformational analysis in large, highly conjugated, chiral molecules. This approach is anticipated to become a complementary methodology for the study of biological macromolcecules in a spectral region that is obscure for standard ECD. However, testing experimentally its full potential is crucial before asserting its capacity to predict, accurately, the TPCD spectra of complex molecules.

In order to test the feasibility of this innovative approach, in this chapter we present the calculation and analysis of the TPCD spectrum of an axially chiral Salen ligand (AXF-155) using FRA. The investigation shown in this chapter reveals the capabilities of FRA for the theoretical calculation of the TPCD spectra of large and complex molecules.

4.1 Introduction

It is know that the spectroscopic application of TPCD yet requires access to the theoretical spectrum of the molecular structure of interest. However, the typical computational cost in large systems can become prohibited as the molecular structure becomes more complex. In order to overcome these barriers we have recently developed a fragment recombination approach that allows overcoming the computational limitations found in first principle calculations of the TPCD spectra of large optically active molecules [1]. We have demonstrated, theoretically (Chapter II), that the additive property of TPCD allows to reconstructing the spectrum of an entire molecule from those calculated on its corresponding segments, and permits performing the recognition of specific spectral features and identify the origin of spectral fingerprints on the TPCD spectrum of large chiral molecules.

With the aim of uncovering the full potential of TPCD and FRA for the determination of the structural conformation of large chiral molecules, we became engaged in the nonlinear optical study of a recently synthesized, highly conjugated, axially-chiral binaphthyl fluorene based Salen ligand in solution, AFX-155 [2,2'-(1E,1'E)-(R)-1,1'-binaphthyl-2,2'-diylbis(azan-1-yl-1-ylidene)bis(methan-1-yl-1-ylidene)bis(4-((7-(diphenylamino)-9,9-dihexyl-9H-fluoren-2-l)ethynyl)phenol)] [2]. The comparative theoretical-experimental analysis of the TPA and TPCD spectra of the four primary conformers of AXF-155 and its corresponding halves (AXF-169') shows that the TPA of AXF-155 is mainly determined by AXF-169', and validates the presence of only the Trans_R-*Intra*(NHB)//Trans_R-*Extra*(HB) and Trans_R-*Intra*(NHB)//Trans_R-*Extra*(NHB) conformers in THF solution. AXF-155 is expected to find potential applications in homogeneous catalysis, biophotonics and sensing.

4.2 Experimental Section

AXF-155 was synthesized as previously reported in reference 2. The TPA and TPCD measurements were performed in a 7.5 mM solution of AXF-155/THF employing the double-L scan technique [3]. Two-photon excitation was induced with a computer-controlled femtosecond optical parametric amplifier (OPerA Solo) pumped by an amplified laser system from COHERENT. The whole systems is capable of generating 90 fs (FWHM) pulses over a wavelength range that spans from 240 nm to 2.6 μm, and with pulse energies up to 4 mJ at a 1-kHz repetition rate. Experiments were performed at a 40 Hz repetition rate to avoid any contribution from accumulative effects. The pulse width was determined using a single shot autocorrelator from Coherent Inc. and a frequency-resolved optical gaiting (FROG) from Swamp Optics LLC.

4.3 Computational Methods

The theoretical background involved in this research has been given in detail in references 4-9 and is also presented in sections 1.2 and 1.5 of the introduction to this dissertation. Therefore, in this part we only present the computational details relevant to the corresponding calculations.

The molecular structure of AXF-155 (Figure 4-1.c), the main conformers of AXF-169' [(E)-4-((7-(diphenylamino)-9,9-dihexyl-9H-fluoren-2-yl)ethynyl)-2-((naphthalen-2-ylimino-1-methyl) methyl)phenol] (Figure 4-1.a) and those of the core of AXF-155 (C-AXF-155) [2,2'-(1E,1'E)-1,1'-binaphthyl-2,2'-diylbis(azan-1-yl-1-ylidene)bis(methan-1-yl-1-ylidene)bis(4-ethynyl)phenol)] (Figure 4-1.b) were optimized using Density Functional Theory (DFT) [10, 11] in Gaussian 09 [12], employing the Becke's three-parameter exchange, Lee, Yang and Parr

correlation (B3LYP) hybrid functional [13-15], and the 6-31G* basis set [16]. The TPA and TPCD response for the lowest 50 electronic excited states of all optimized structures were calculated with Dalton 2011 [17], under Time-Dependent DFT (TD-DFT) [10, 11], at the same level of theory as for the geometry optimizations. All the calculations were carried out *in vacuo* because the relatively large size of AXF-155 and AXF-169' proved to be a challenge to our computational resources when including solvent effects through the polarizable continuum model (PCM), consequently, the theoretical spectra where slightly red shifted (~ 0.1-0.2 eV) with respect to the experimental. The convolution of the TPA and TPCD spectra were obtained employing Equations 1-18 and 1-37 (see dissertation introduction), respectively, using a normalized Lorentzian lineshape (See Equation 1-15 in dissertation introduction) with $\Gamma = 0.20$ eV (FWHM).

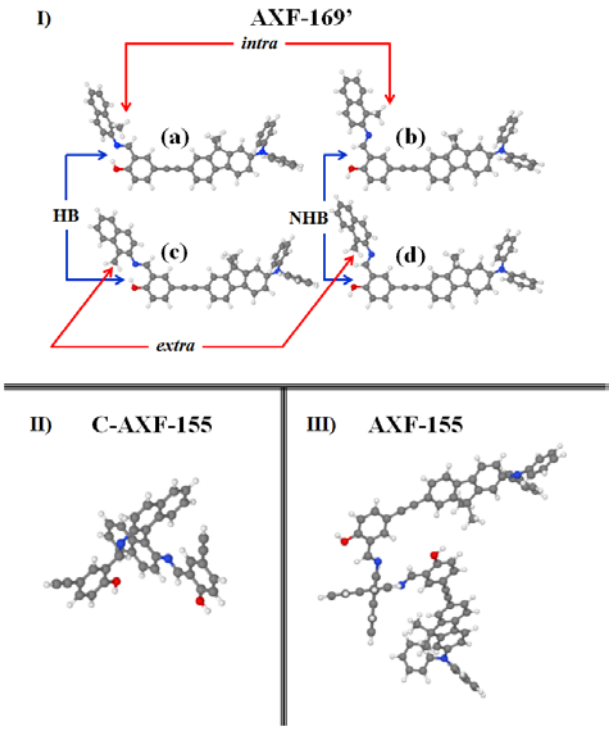

Figure 4-1. I) Molecular structures of AXF-169' conformers (i) trans_R-Intra(HB), (ii) trans_R-Intra(NHB), (iii) trans_R-Extra(HB), (iv) trans_R-Extra(NHB) (arrows show the specific features corresponding to HB or NHB and intra or extra. **II)** Molecular Structure of C-AXF-155. **III)** Molecular structure of trans_R-Intra(NHB)//trans_R-Extra(NHB).

4.4 Results and discussion

In order to show the existent complementarity between the linear and the nonlinear circular dichroism techniques for the structural analysis of large, highly conjugated chiral molecules, we measured the TPA spectra of AXF-155/THF using linearly polarized light (LPL) and circularly polarized light of both handedness, assessed its TPCD spectrum, and compared them with their corresponding linear counterparts (OPA and ECD spectra) [2].

In Figure 4-2.a, we show the comparison between the OPA and the TPA spectra measured with LPL.

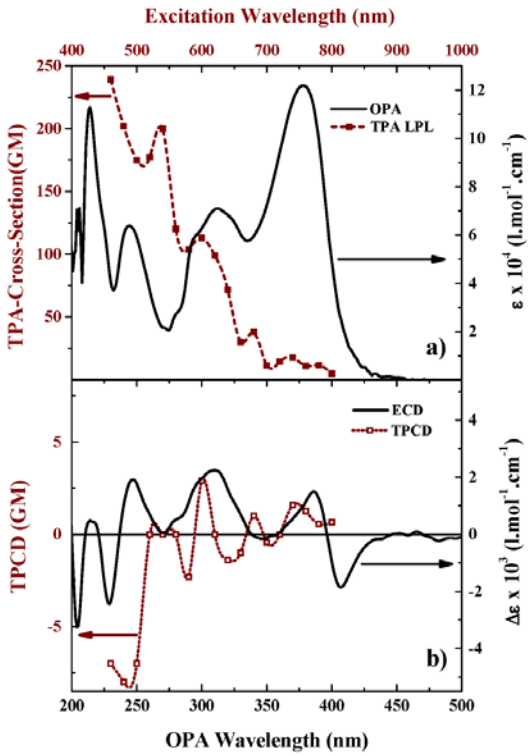

Figure 4-2. a) Experimental OPA (black solid line) and TPA spectra using LPL (■) of AXF-155. **b)** Experimental ECD (black solid line) and TPCD spectra (□) of AXF-155. All spectra are plotted with respect to the OPA (bottom) and TPA (top) excitation wavelength.

It can be observed that for the most part of the spectral range, the maxima and minima in the OPA spectrum do not correspond to those in the TPA spectrum (plotted in the OPA scale). This feature was anticipated based on the differences in parity selection rules that govern these

two processes [18]. However, because this particular molecule is not centrosymmetric, the already mentioned selection rules are relaxed, thus leading to a slight spectral overlap between approximately 300 nm and 350 nm. One should highlight the fact that TPA measurements were only performed between 460 nm to 800 nm, the region for which TPA was large enough to be measured and two-photon resonance enhancement effect is absent for the most part of the spectrum [19]. However, it can be observed, through the large increase in $\delta^{TPA}(\lambda)$, that as the TPA excitation wavelength gets closer to the tail of the linear absorption spectrum ($\lambda_{TPA} \leq 500$ nm) the two-photon resonance enhancement effect becomes very important [19]. Figure 4-2.b show the ECD and TPCD experimental spectra of AXF-155/THF. It is remarkable that the alternating positive and negative bands that define the shape of the TPCD spectrum of AXF-155 in THF solution have no substantial correlation with those observed in its ECD spectrum. These results evidence the complementarity of the two techniques [20].

With the aim of extracting the desired structural information of AXF-155 using multi-photon absorption, we attempted to calculate the theoretical TPA spectrum of this molecule at the B3LYP/6-31G* level of theory over the first 50 electronic excited states in gas phase. The level of complexity of the molecular structure of AXF-155, along with the requirement of a basis set with at least one polarization function (6-31G*) to yield reliable results, proved to be overly-demanding on our computational resources. In order to overcome this obstacle we took a similar approach to that employed by our group during the linear characterization of AXF-155 using OPA and ECD [2] but this time we made it systematically using FRA [1]. Briefly, FRA consists on building the structure of the molecule of interest and optimizing the molecular structure of the whole system, then a conditional fragmentation of the optimized molecular structure is performed respecting the following four fundamental points [1]: i) the original π-electron

delocalization should not be broken; ii) the relative position of the moieties, as well as the original dihedral angles between fragments should remain intact in each segment after fragmentation has been completed (no further re-optimization); iii) the existent overall and partial chirality in the full molecule must continue in the corresponding fragments; and iv) the removed segments should be replaced by functional groups that are passive to the overall electronic properties of the residual fragment subject to study.

It is important to stress that the application of FRA is only possible in systems with moieties which are expected to be relatively weakly interacting. [1] This is indeed the case in AXF-155, as shown next. First we proceeded to optimize the different conformers of the molecule because they present small but important conformational differences - relative orientation, dihedral angles, intramolecular hydrogen bonding and partial chirality - that can indeed affect the shape, magnitude and position of their corresponding TPCD spectra. Next, we divided the molecule at its very center where the two naphtyl rings are bonded together. Through this procedure two equivalent fragments were generated. To keep track of the relative orientation of the detached portion we replaced the removed fragment by a methyl group, the resultant structure is the so called AXF-169' (see Figure 4-1.a). Since AXF-169' does not consider the axial chirality coming from the binaphthyl moiety, right at the center of the molecule, we chopped apart the core of the molecule from each optimized conformer (C-AXF-155) (see Figure 4-1.b). The structure optimization and full characterization of AXF-169' (Figure 4-1.a) has already been done in our group and it can be found in reference 2. Despite the initial 16 possible different conformations for AXF-169', in reference 2 it was demonstrated that only four conformers were relevant for the molecular structure of AXF-155/THF, i.e. the *trans_R-intra* and *trans_R-extra* configurations with and without hydrogen bonding, HB and NHB,

respectively (see Figure 4-1.a). As a result of those findings, our analysis in this chapter focuses only on these main conformers of AXF-155/THF, which through the direct theoretical-experimental comparison of their TPA and TPCD spectra, allows to identifying the very dominant conformers of the entire molecule in solution, as shown next.

Figures 4-3 and 4-4 show the theoretical TPA spectra of the AXF-169'conformers calculated at the B3LYP/6-31G* level of theory for the first 50 electronic excited states in gas phase, as well as the experimental TPA spectrum of AXF-155, measured with LPL. First thing to notice is the relative similarity between all four theoretical TPA spectra and their spectral correspondence with the experimental TPA spectrum of AXF-155 (bands centered at ca. 750 nm, 680 nm, 610 nm and 510 nm). This result is not surprising considering the fact that the ~ 90^0 dihedral angle between the naphtyl rings at the center of AXF-155, restricts the π-electronic delocalization to half of the molecule, and that the small structural changes between all four conformers of AXF-169' (the fragments contributing to the TPA of AXF-155) have a minor impact on the charge transfer along the short AXF-169' structure. However, the observed differences between the TPA spectra of all conformers are clearly more related to the formation or not of intramolecular hydrogen bond, where the former presents a stronger transition at ~ 610 nm (HB: Figures 4-3.a, 4-3.c, 4-4.a and 4-4.d – NHB: Figures 4-3.b, 4-3.d, 4-4.b and 4-4.c). The direct comparison of the TPA spectra of AXF-169' with and without HB seems to indicate that the most dominant conformer of AXF-155 should present a combination of HB on one arm and NHB on the other.

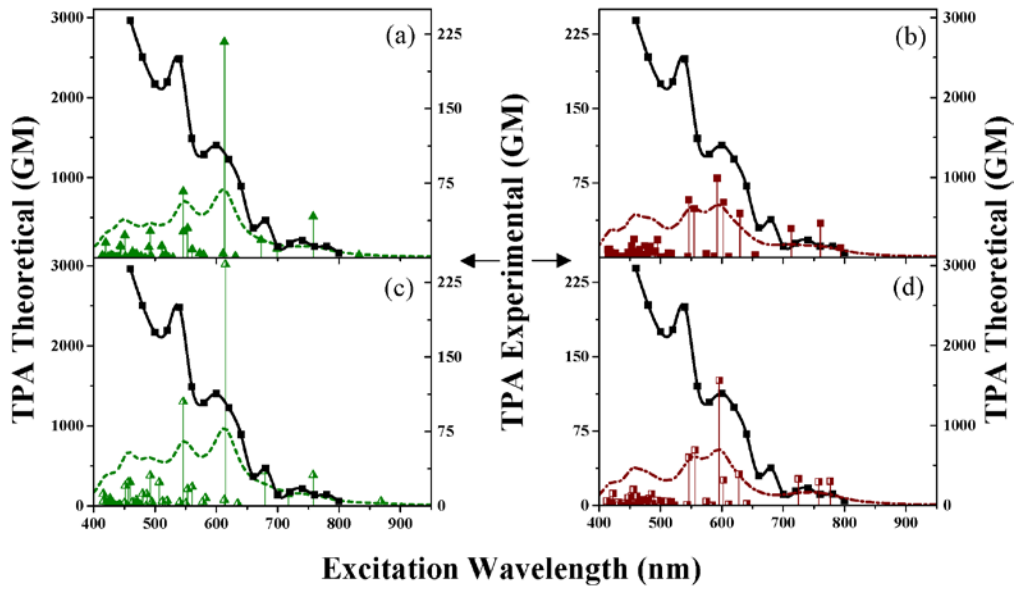

Figure 4-3. Theoretical TPA stick (scattered symbols with vertical lines) and convoluted spectra (broken lines) for AXF-169'conformers (a) trans_R-*Intra*(HB) from HB//HB, (b) trans_R-*Intra*(NHB) from NHB//NHB, (c) trans_R-*Extra*(HB) from HB//HB, (d) trans_R-*Extra*(NHB) from NHB//NHB. Experimental TPA spectrum of AXF-155 (black squares and solid line). Theoretical spectra are displayed with a spectral shift of -50 nm.

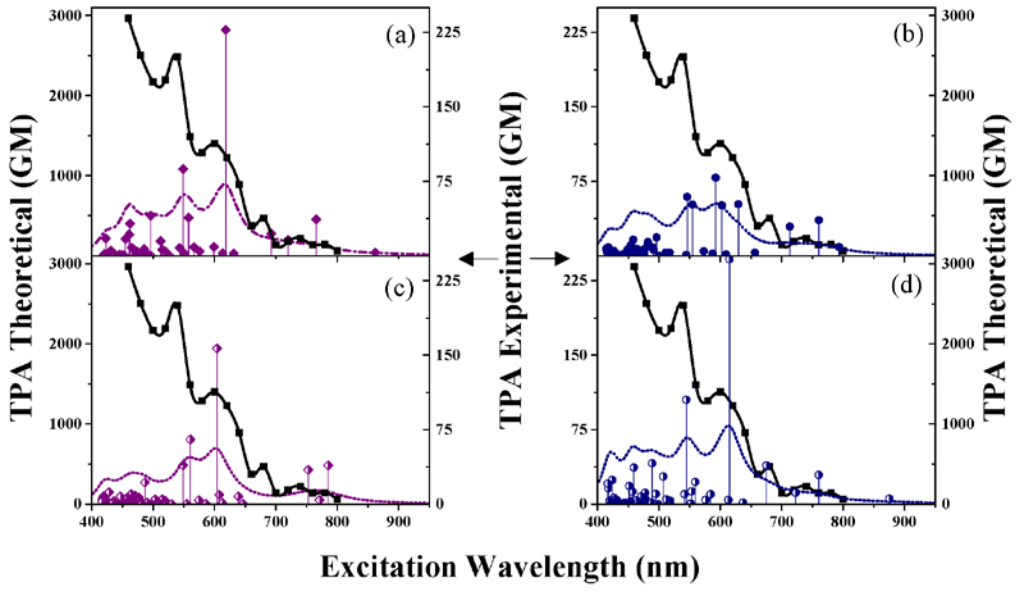

Figure 4-4. Theoretical TPA stick (scattered symbols with vertical lines) and convoluted spectra (broken lines) for AXF-169'conformers (a) trans_R-*Intra*(HB) from HB//NHB, (b) trans_R-*Intra*(NHB) from NHB//HB, (c) trans_R-*Extra*(NHB) from HB//NHB, (d) trans_R-*Extra*(NHB) from NHB//HB. Experimental TPA spectrum of AXF-155 (black squares and solid line). Theoretical spectra are displayed with a spectral shift of -50 nm.

Figure 4-5 display the TPA-FRA spectra of all four conformers of AXF-155, obtained by adding the corresponding AXF-169' fragments for each configuration. The theoretical TPA cross-section of AXF-169' is approximately half that of the TPA-FRA of the entire molecule which demonstrates that the TPA amplitude of AXF-155 is the result of having two, non-conjugated, AXF-169'. Comparable results were found throughout the linear optical characterization of AXF-155 [2]. Also, it can be observed that the conformer with HB/HB on both sides is the one that resemble the least to the experimental. However, the observed differences in TPA are not enough to discard any of the four arrangements.

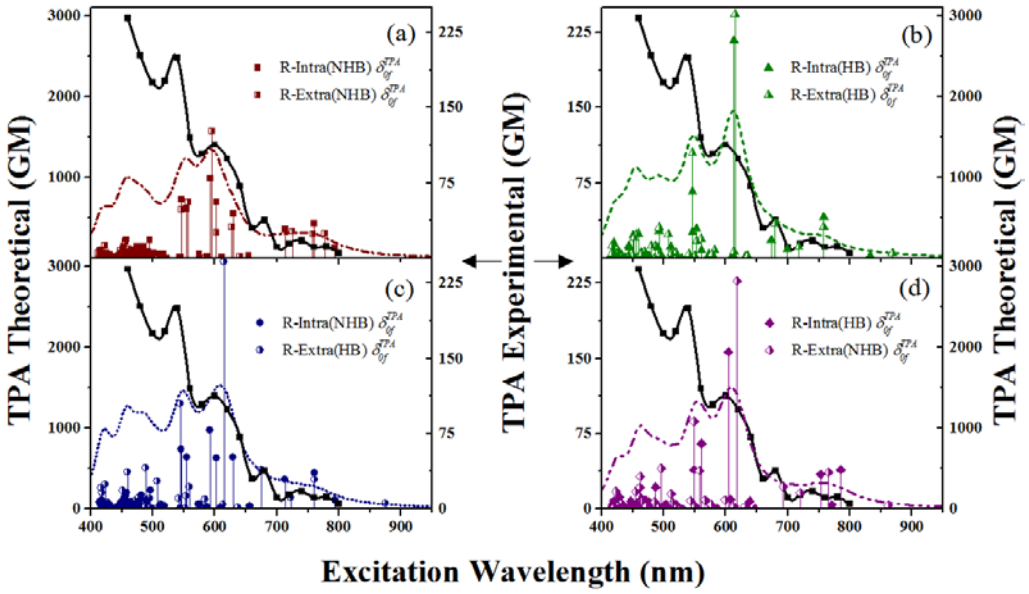

Figure 4-5. Theoretical TPA-FRA stick (scattered symbols with vertical lines) and convoluted spectra (broken lines) for AXF-169'conformers (a) trans_R-*Intra*(NHB)//trans_R-*Extra*(NHB), (b) trans_R-*Intra*(HB)//trans_R-*Extra*(HB), (c) trans_R-*Intra*(NHB)//trans_R-*Extra*(HB), (d) trans_R-*Intra*(HB)//trans_R-*Extra*(NHB). Experimental TPA spectrum of AXF-155 (black squares and solid line). Theoretical spectra are displayed with a spectral shift of -50 nm.

In order to determine the most dominant conformer of AXF-155/THF using our existent computational capabilities, we assessed the theoretical TPCD spectrum of the large molecule

using FRA. Because AXF-155 meets the necessary structural requirements for TPCD to be treated as an additive property,[1] and TPCD is very sensitive to conformational changes, the establishment of the most dominant conformer of AXF-155/THF was performed by adding the TPCD spectra of the two AXF-169' and that of C-AXF-155 obtained from each possible conformer. Figures 4-6 to 4-9 shows the resultant TPCD spectra of AXF-155 on Trans_R-*Intra*(HB)//Trans_R-*Extra*(HB), Trans_R-*Intra*(HB)//Trans_R-*Extra*(NHB), Trans_R-*Intra*(NHB)//Trans_R-*Extra*(HB) and Trans_R-*Intra*(NHB)//Trans_R-*Extra*(NHB), respectively using FRA as well as its experimental TPCD spectrum. One can notice in all these figures that each plot has four subtle conformational differences (ΔΔ, ΛΛ, ΔΛ, ΛΔ) corresponding to a permanent propeller chirality, apparently present on the diphenylamine moieties at the end of each AXF-169' (Δ or Λ - see Figure 4-10). These features were not specifically considered using standard ECD [2] because of the typical fast Δ↔Λ interconversion [21] in similar moieties. However, we have found in this work, using TPCD-FRA, that AXF-155 presents a preferential propeller arrangement. This interesting point will be expanded more in depth at the end of the discussion.

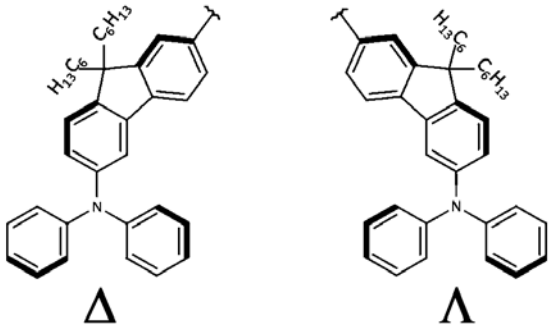

Figure 4-6. Fragment from AXF-155 exhibiting propeller chirality at the diphenylanmine moiety. Δ (left) and Λ (right) conformers.

The first observation is the large discrepancy between the TPCD-FRA spectra of Trans_R-*Intra*(HB)//Trans_R-*Extra*(HB) and Trans_R-*Intra*(HB)//Trans_R-*Extra*(NHB) and the experimental TPCD spectrum of AXF-155 (see Figures 4-6 and 4-7). The spectral region where

the utmost differences between the theoretical and experimental spectra displayed in Figures 4-6 and 4-7, are stressed by the use of red crossed-squares (☒). Perhaps, the most notorious distinction is the computed opposite band (positive peak) between 450 nm and 500 nm. This obvious disagreement allowed us to totally discard the presence of these two conformers in solution.

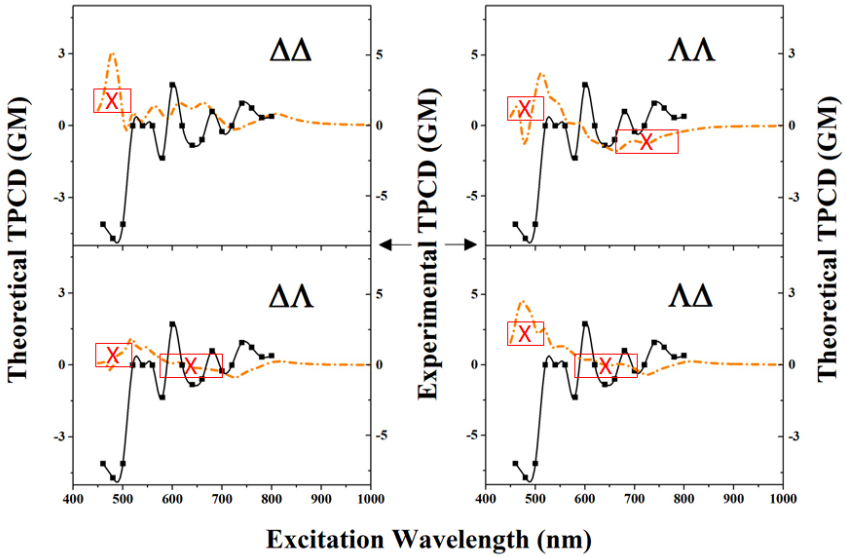

Figure 4-7. Theoretical TPCD-FRA spectra (broken lines) for trans_R-*Intra*(HB)//trans_R-*Extra*(HB) conformers: (a) ΔΔ, (b) ΛΛ, (c) ΔΛ, (d) ΛΔ. Key theoretical-experimental spectral mismatch are highlighted with (☒). AXF-155 experimental TPCD (black squares and solid line).

Next, in Figure 4-8 and 4-9 we present the TPCD-FRA spectra of Trans_R-*Intra*(NHB)//Trans_R-*Extra*(HB) and Trans_R-*Intra*(NHB)//Trans_R-*Extra*(NHB), and the experimental TPCD spectrum of AXF-155. In the former, one can discard the ΛΔ based on the computed opposite band (positive peak) between 450 nm and 500 nm. A close inspection of the remaining three plots in Figure 4-8 enables to discard ΔΛ and ΛΛ, based on the lack of specific spectral structure in the electromagnetic region corresponding to 550 nm < λ < 750 nm which are highlighted with red crossed-squares (☒). Therefore, the only lasting candidate from the

Trans_R-*Intra*(NHB)//Trans_R-*Extra*(HB) is the ΔΔ which TPCD-FRA spectrum presents the most remarkable features observed in the experimental TPCD spectrum, i.e. the four positive peaks at approximately 550 nm, 610 nm, 680 nm and one slightly red shifted at 800 nm; and the four negative bands at approximately 490 nm, 560 nm, and two slightly red shifted at 640 nm and 720 nm (arrows indicate the corresponding spectral match).

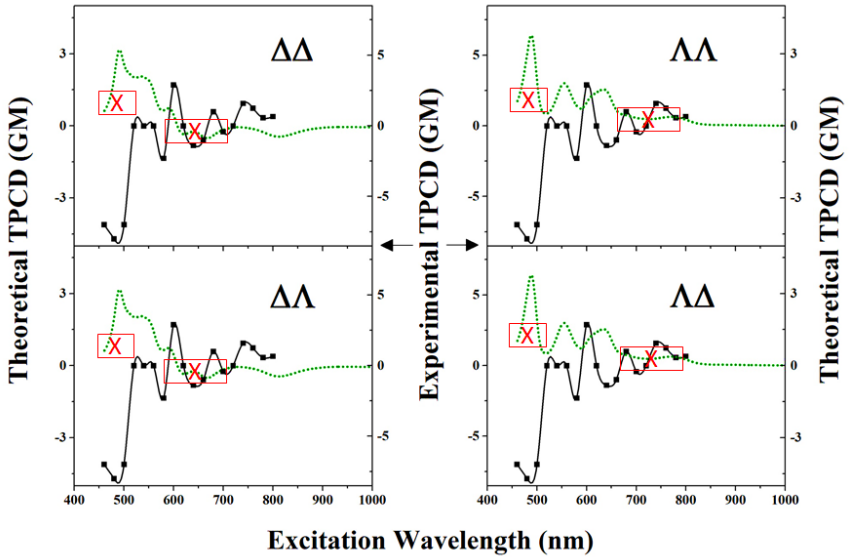

Figure 4-8. Theoretical FRA-TPCD spectra (broken lines) for trans_R-*Intra*(HB)//trans_R-*Extra*(NHB) conformers: (a) ΔΔ, (b) ΛΛ, (c) ΔΛ, (d) ΛΔ. Key spectral theoretical-experimental mismatch are highlighted with (☒). AXF-155 experimental TPCD (black squares and solid line).

Before arriving to any conclusions one needs to examine the four possibilities on the Trans_R-*Intra* (NHB)//Trans_R-*Extra*(NHB). From Figure 4-9 one can immediately discard the ΛΔ, ΔΛ and ΛΛ based also on the computed opposite band (positive peak) between 450 nm and 500 nm and the lack of other specific spectral features in the electromagnetic region highlighted with red crossed-squares (☒). Again, the only lasting candidate from the Trans_R-*Intra* (NHB)//Trans_R-*Extra*(NHB) is the ΔΔ which TPCD-FRA spectrum show the same spectral features observed in the experimental spectrum, i.e. the same four positive and negative bands previously identified in Trans_R-*Intra* (NHB)//Trans_R-*Extra*(HB).

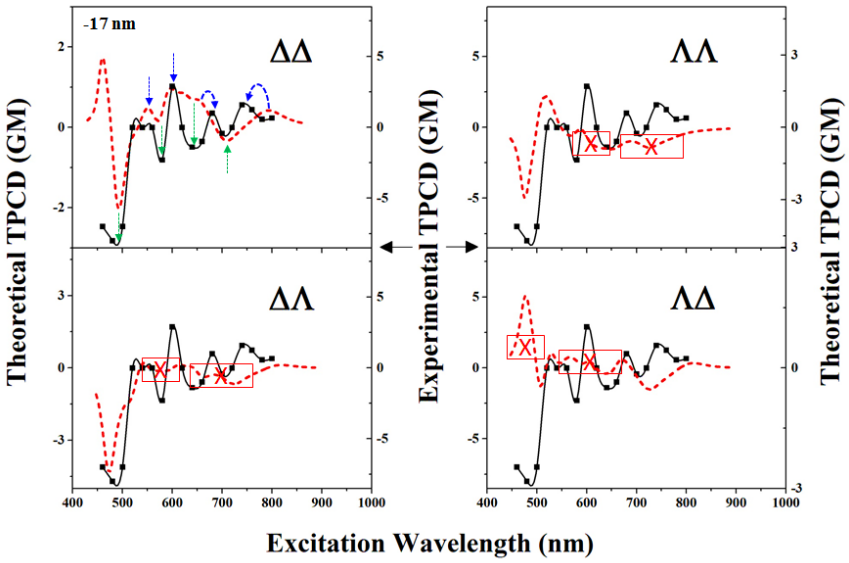

Figure 4-9. Theoretical FRA-TPCD spectra (broken lines) for trans_R-*Intra*(NHB)//trans_R-*Extra*(HB) conformers: (a) ΔΔ (A spectral shift of -17 nm was applied) - Arrows show main spectral theoretical-experimental matching; (b) ΛΛ, (c) ΔΛ, (d) ΛΔ. Key theoretical-experimental spectral mismatch are highlighted with (☒). AXF-155 experimental TPCD (black squares and solid line).

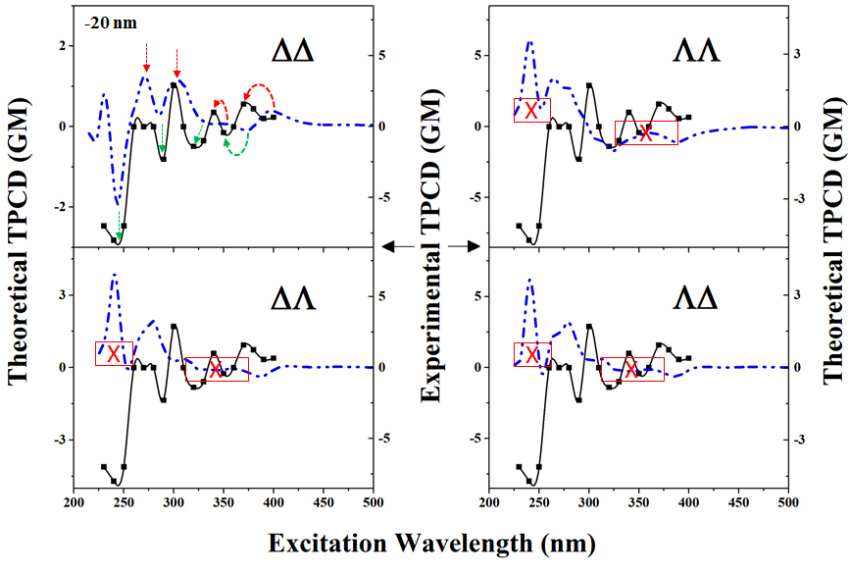

Figure 4-10. FRA-TPCD spectra (broken lines) for trans_R-*Intra*(NHB) // trans_R-*Extra*(NHB) conformers of AXF-155. (a) ΔΔ (A spectral shift of -20 nm was applied) - Arrows show main spectral theoretical-experimental matching; (b) ΛΛ, (c) ΔΛ, (d) ΛΔ. Key spectral theoretical-experimental mismatch are highlighted with (☒). AXF-155 experimental TPCD (black squares and solid line).

Now that the number of possible conformers has been reduced to only two, one can proceed to perform the identification of specific spectral fingerprints and their origin looking at the computed TPCD spectra of the fragments.

Figure 4-11 and 4-12 display the TPCD spectra of the three fragments in Trans_R-*Intra* (NHB)//Trans_R-*Extra*(HB) and Trans_R-*Intra* (NHB)//Trans_R-*Extra*(NHB), respectively, and the TPCD-FRA for the entire molecules. The direct comparison between the computed TPCD-FRA spectra of these two conformers, generated on their corresponding AXF-169' and C-AXF-155, and the experimental spectrum of AXF-155 allows to allocate contributions from the specific fragments in each molecule (Figure 4-11.d and Figure 4-12.d). In Table 4-1 and 4-2 we present the assignment of the most important transitions originated in the different fragments which contribute to the overall TPCD spectra of the entire molecules. The main difference between the TPCD-FRA spectra of Trans_R-*Intra* (NHB)//Trans_R-*Extra*(HB) and Trans_R-*Intra* (NHB)//Trans_R-*Extra*(NHB) comes from small distortions adopted by the center (C-AXF-155) which produces a larger positive contribution on the blue side of the spectrum in the latter and a negative contribution in the former. These structural variations are mainly produced by the presence or absence of intramolecular hydrogen bonding on one or both arms. In fact, we found (data not showed) that the strong positive band observed between 450 nm and 500 nm, in the Trans_R-*Intra*(HB)//Trans_R-*Extra*(HB) (Figure 4-6) and Trans_R-*Intra*(HB)//Trans_R-*Extra*(NHB) (Figure 4-7), which certainly allowed us to eliminated those two basic conformers from the potential candidates of AXF-155 prevailing in THF solution, were basically shaped by the small modification of C-AXF-155 in those conformers after the optimization of the corresponding arrangements of AXF-155. Similar type of contribution were responsible for the distorted TPCD-FRA spectra in three of the four conformers of Trans_R-*Intra*(HB)//Trans_R-*Extra*(NHB) (Figure 4-9), i.e. those with a positive peak in the blue side of the spectrum (ΛΔ, ΔΛ and ΛΛ). Beside, one can observe significant differences between the TPCD spectra of the Trans_R-*Extra*(HB) and the Trans_R-*Extra*(NHB) fragments at $\lambda_{TPA} < 500$ nm.

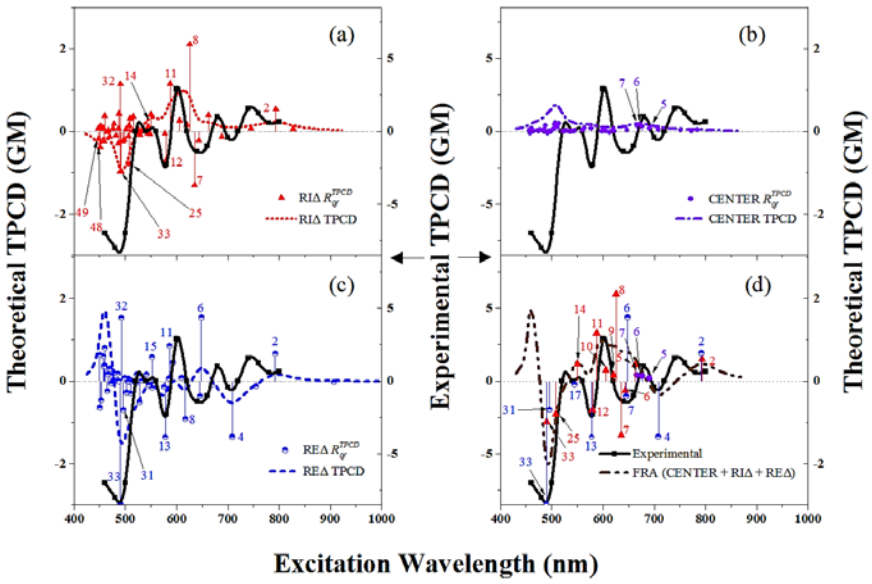

Figure 4-11. Theoretical TPCD stick (scattered symbols with vertical lines) and convoluted (broken lines) spectra of (a) trans_R-*Intra*(NHB) - Δ conformer [RIΔ], (b) C-AXF-155 [CENTER], (c) trans_R-*Extra*(HB) - Δ conformer [REΔ]; (d) RIΔ + REΔ + CENTER. Experimental TPCD spectrum of AXF-155 (black squares and solid line). The most relevant TPCD transitions from all fragments are specified in (d). All theoretical spectra are shifted -17 nm.

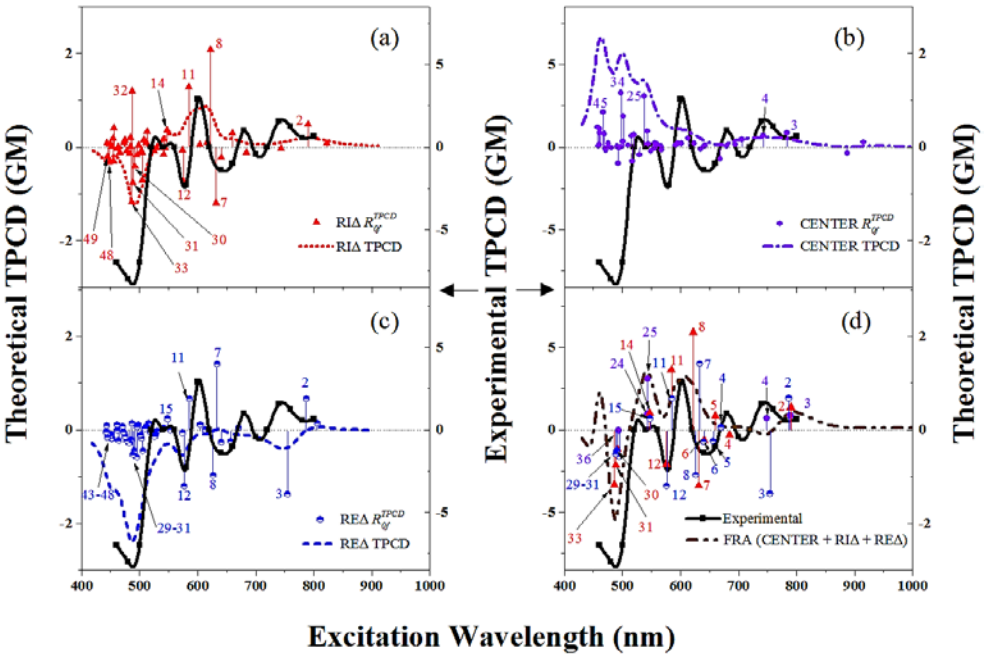

Figure 4-12. Theoretical TPCD stick (scattered symbols with vertical lines) and convoluted (broken lines) spectra of (a) trans_R-*Intra*(NHB) - Δ conformer [RIΔ], (b) C-AXF-155 [CENTER], (c) trans_R-*Extra*(NHB) - Δ conformer [REΔ], (d) RIΔ + REΔ + CENTER. Experimental TPCD spectrum of AXF-155 (black squares and solid line). The most relevant TPCD transitions from all fragments are specified in (d). All theoretical spectra are shifted -20 nm.

Something that needs special attention is the fact that the two remaining conformers, Trans_R-*Intra*(NHB)//Trans_R-*Extra*(HB) and Trans_R-*Intra*(NHB)//Trans_R-*Extra*(NHB), present NHB on the Trans_R-*Intra* side while on the other side both options, HB and NHB, are likely. In an effort to discern between the four possible structures of Trans_R-*Intra*//Trans_R-*Extra* (NHB/NHB, NHB/HB, HB/NHB, HB/HB), during the linear characterization of this molecule using ECD (see reference 2), we calculated the energies and entropies of these four structures. While the energy of the structure with HB only on the Trans_R-*Intra* was slightly lower, the entropy of that with NHB on the same side overwhelmed the previous, and that with NHB/NHB presented the largest entropy value. The preferential formation of these two species was supported by the examination of solvation effects throughout the two-step mechanism of reaction proposed. Of course, with ECD we were not able to totally discard the other two conformers as we have been able to do using TPCD. At this point, one can be certain of the exclusive presence of AXF-155 in its Trans_R-*Intra*(NHB)//Trans_R-*Extra*(HB) and Trans_R-*Intra*(NHB)//Trans_R-*Extra*(NHB) in THF solution.

Table 4-1. Assignment of the predominant transitions that define the main positive and negative TPCD bands in the two AXF-169' fragments and C-AXF-155, with a direct correspondence with those obtained for the ΔΔ conformer of Trans_R-Intra (NHB)//Trans_R-Extra(HB).

	AXF-155 Excitation Wavelength (nm)	Excited States from Fragments		
		AXF-169' Trans_R-*Intra* (NHB)	AXF-169' Trans_R-*Extra*(HB)	C-AXF-155
Positive Bands	550	14	17	-
	600	8,9,10,11	-	-
	680	5	6	5,6,7
	750	2	2	-
Negative Bands	480	25,33	33,31	-
	560	12	13	-
	640	6,7	7	-
	720	-	4	-

TPCD-FRA results undeniably reduced the number of possible conformers of AXF-155, thought to be present in THF solution after the linear characterization of this molecule using ECD [2]. However, there is again an open question: why are the conformers with the preferred ΔΔ propeller chirality motif on both diphenylamine moieties, at the end of each AXF-169', the apparently only species of AXF-155 present in THF solution and not just a mixture of all different possibilities on both sides? In order to attempt to answer this question one needs to remember first the proposed mechanisms for interconversion in the source moiety (triphenylamine like molecule). According to theoretical-experimental studies done by Reva and co-workers, [21] on the conformational flexibility of triphenylamine monomer scanning the potential energy hypersurface of the system and performing FTIR spectroscopy analysis, the favored minimal energy pathway between the left-hand rotating and right-hand rotating symmetry is that through a route that conserves a C_2 symmetry axis (energy barrier is ~20 kJ mol^{-1}) rather than the concerted twist of all the phenyl rings route in the same direction with conservation of a C_3 symmetry axis (energy barrier of ~54 kJ mol^{-1}). The preferential interconversion in this type of molecule, through the least energetic route (C_2 symmetry axis conserved), requires the synchronized rotation, in the same direction, of two phenyl rings around the N–C bond while the third one rotates in the opposite direction. Since in AXF-155 one of the phenyl rings is replaced by a fluorenyl moiety (see Figure 4-10) bound to a very long chain, one can foresee how much more difficult, in terms of the energy barrier, will be for this molecule to interconvert ones it is in a specific configuration. This explanation is reasonable, but it does not answer why should it stay with a ΔΔ motif? On this point we can only speculate that because throughout the synthesis of AXF-155 we used an asymmetric catalyst ((R)-(+)-2,2'-diamino-1,1'-binapthalene) [2] to produce the chiral Salen ligand, the presence of this reagent in solution induces

the preferential Δ propeller chirality motif on both diphenylamine moieties, at the end of each AXF-169'. This hypothesis is reinforced by the experimental results obtained during the characterization of the synthesized AXF-169 (half AXF-155) which was prepared in the absence of an asymmetric catalyst. AXF-169 did not present any optical activity and ECD [2], suggesting this outcome the presence of a racemic mixture, thus no preferential propeller chirality is present on the diphenylamine moieties. In addition, computed ECD spectra of AXF-155, considering different Λ-Δ configurations, did not lead to different results from what was reported in reference 2.

Table 4-2. Assignment of the predominant transitions that define the main positive and negative TPCD bands in the two AXF-169' fragments and C-AXF-155, with a direct correspondence with those obtained for the ΔΔ conformer of Trans_R-Intra (NHB)//Trans_R-Extra(NHB).

	AXF-155 Excitation Wavelength (nm)	Excited States from Fragments		
		AXF-169' Trans_R-*Intra* (NHB)	AXF-169' Trans_R-*Extra*(NHB)	C-AXF-155
Positive Bands	550	14	15	24,25
	600	8,11	7,11	12
	680	5	4	-
	750	2	2	3,4
Negative Bands	480	30,31,33	29,30,31	36
	560	12	12	-
	640	6,7	5,6	9
	720	4	-	-

4.5 Conclusions

TPCD is a powerful nonlinear optical technique for the structural identification of large and conjugated optically active molecules. The obtained theoretical-experimental matching of TPCD spectra led to the identification of only two dominant conformer of AXF-155 in THF solution, the Trans_R-*intra*(NHB)//Trans_R-*extra*(HB) and Trans_R-*intra*(NHB)//Trans_R-*extra*(NHB). The sensitivity to structural and conformational changes of this nonlinear approach

helped refine the identification of the preferred ΔΔ propeller chirality motif on the AXF-169' fragments. TPCD and ECD are indeed complementary spectroscopic techniques for the structural analysis of chiral molecules and structures. The validation of the use of FRA for the theoretical determination of TPCD spectrum of large, highly conjugated, chiral molecules can find potential applications in the conformational study and characterization of large biological molecules such as peptides, polypeptides and proteins in a spectral region that is obscure for standard ECD.

4.6 References

1. Diaz, C.; Echevarria, L.; Hernández, F. E., Overcoming the Existent Computational Challenges in the Ab Initio Calculations of the Two-Photon Circular Dichroism Spectra of Large Molecules using a Fragment-Recombination Approach. *Chem. Phys. Lett.* **2013,** *568-569,* 176-183.

2. Diaz, C.; Frazer, A.; Morales, A.; Belfield, K. D.; Ray, S.; Hernández, F. E., Structural identification of a novel axially chiral binaphthyl fluorene based salen ligand in solution using electronic circular dichroism: a theoretical-experimental analysis. *J. Phys. Chem. A* **2012,** *116,* 2453-2465.

3. De Boni, L.; Toro, C.; Hernandez, F. E., Synchronized Double L-Scan Technique for the Simultaneous Measurement of Polarization-Dependent Two-Photon Absorption in Chiral Molecules. *Opt. Lett.* **2008,** *33,* 2958-2960.

4. Rizzo, A.; Jansík, B.; Pedersen, T. B.; Agren, H., Origin Invariant Approaches to the Calculation of Two-Photon Circular Dichroism. *J. Chem. Phys.* **2006,** *125,* 64113.

5. Jansík, B.; Rizzo, A.; Agren, H., Ab Initio Study of the Two-Photon Circular Dichroism in Chiral Natural Amino Acids. *J. Phys. Chem. B* **2007,** *111,* 446-460.

6. Jansík, B.; Rizzo, A.; Ågren, H.; Champagne, B., Strong Two-Photon Circular Dichroism in Helicenes: A Theoretical Investigation. *J. Chem. Theory Comput.* **2008,** *4,* 457-467.

7. Rizzo, A.; Lin, N.; Ruud, K., Ab Initio Study of the One- and Two-Photon Circular Dichroism of R-(+)-3-Methyl-Cyclopentanone. *J. Chem. Phys.* **2008,** *128,* 164312.

8. Lin, N.; Santoro, F.; Rizzo, A.; Luo, Y.; Zhao, X.; Barone, V., Theory for Vibrationally Resolved Two-Photon Circular Dichroism Spectra. Application to (R)-(+)-3-Methylcyclopentanone. *J. Phys. Chem. A* **2009,** *113,* 4198-4207.

9. Guillaume, M.; Ruud, K.; Rizzo, A.; Monti, S.; Lin, Z.; Xu, X., Computational Study of the One- and Two-Photon Absorption and Circular Dichroism of (L)-Tryptophan. *J. Phys. Chem. B* **2010,** *114*, 6500-6512.

10. Runge, E.; Gross, E. K. U., Density-Functional Theory for Time-Dependent Systems. *Phys. Rev. Lett.* **1984,** *52*, 997-1000.

11. Dierksen, M.; Grimme, S., A Theoretical Study of the Chiroptical Properties of Molecules with Isotopically Engendered Chirality. *J. Chem. Phys.* **2006,** *124*, 174301.

12. Frisch, M. J.; Trucks, G. W.; Schlegel, H. B.; Scuseria, G. E.; Robb, M. A.; Cheeseman, J. R.; Scalmani, G.; Barone, V.; Mennucci, B.; Petersson, G. A., *et al.*, Gaussian 09, Revision A.1. Gaussian, Inc.: Wallingford CT, 2009.

13. Becke, A. D., Density-Functional Exchange-Energy Approximation with Correct Asymptotic Behavior. *Phys. Rev. A* **1988,** *38*, 3098-3100.

14. Becke, A. D., Density-Functional Thermochemistry. III. The Role of Exact Exchange. *J. Chem. Phys.* **1993,** *98*, 5648-5652.

15. Lee, C.; Yang, W.; Parr, R. G., Development of the Colle-Salvetti Correlation-Energy Formula into a Functional of the Electron Density. *Phys. Rev. B: Condens. Matter* **1988,** *37*, 785-789.

16. Rassolov, V. A.; Pople, J. A.; Ratner, M. A.; Windus, T. L., 6-31G* Basis Set for Atoms K through Zn. *J. Chem. Phys.* **1998,** *109*, 1223-1229.

17. DALTON *A Molecular Electronic Sstructure Program, Release Dalton 2011, see* *http://daltonprogram.org/*, 2011.

18. Bonin, K. D.; McIlrath, T. J., Two-Photon Electric-Dipole Selection Rules. *J. Opt. Soc. Am. B* **1984,** *1*, 52-55.

19. Day, P. N.; Nguyen, K. A.; Pachter, R., TDDFT Study of One- and Two-Photon Absorption Properties: Donor-π-Acceptor Chromophores. *J. Phys. Chem. B* **2005,** *109*, 1803-1814.

20. Toro, C.; De Boni, L.; Lin, N.; Santoro, F.; Rizzo, A.; Hernandez, F. E., Two-Photon Absorption Circular Dichroism: A New Twist in Nonlinear Spectroscopy. *Chem. Eur. J.* **2010,** *16*, 3504-3509.

21. Reva, I.; Lapinski, L.; Chattopadhyay, N.; Fausto, R., Vibrational spectrum and molecular structure of triphenylamine monomer: A combined matrix-isolation FTIR and theoretical study. *Phys. Chem. Chem. Phys.* **2003,** *5*, 3844-3850.

CHAPTER 5 : TWO-PHOTON CIRCULAR DICHROISM OF AN AXIALLY DISSYMETRIC DIPHOSPHINE LIGAND WITH STRONG INTRAMOLECULAR CHARGE TRANSFER

*Reproduced with permission of the American Chemical Society from: C. Díaz, L. Echevarria, A. Rizzo, F.E. Hernández, J. Phys. Chem. A **2014**, 118, 940-946.*

So far we have: i) studied the effect of the relative positioning of the biaryl moieties in axially chiral BINOL derivatives on the magnitude of the TPCD signal of biaryl derivatives, ii) developed a Fragment Recombination Approach (FRA) for the calculation of the TPCD spectra of large molecules, and iii) demonstrated the full capability of FRA-TPCD on a large, highly conjugated, axially chiral Salen ligand (AXF-155). However, we have not addressed yet the important effect of intramolecular charge transfer (ICT) onto the TPCD signal of conjugated molecules.

In this chapter we present the study of ICT in S-BINAP, a well-known axially chiral dissymmetric phosphine that exhibits strong intramolecular charge transfer due to the donating nature of the phosphine substituents attached to the biaryl core. The theoretical analysis of the TPCD spectrum of this molecule was performed using time-dependent density functional theory (TD-DFT) calculations at two different levels of theory: B3LYP/6-31G* and CAM–B3LYP/6-31G*. Through the comparative examination of these two exchange correlation functionals we demonstrate the higher reliability of CAM–B3LYP for the accurate reproduction of the experimental TPCD spectrum of S-BINAP. Additionally, we prove necessary to extend the TPCD calculations to the maximum number of electronic excited states possible for the correct assignment of the experimental bands.

5.1 Introduction

Despite all the recent advancement in TPCD, more needs to be investigated on the selection criteria of the most appropriate exchange-correlation functional (XCF) that would produce the best theoretical-experimental match, mainly in chiral molecules with a strong intramolecular charge-transfer (ICT). During the last two decades, the most popular XCF for the calculation of the nonlinear optical properties of organic molecules has been the Becke's three-parameter exchange and the Lee–Yang–Parr (B3LYP), [1-3] mainly because of its success in a wide range of applications.[4] However, more recently its Coulomb attenuated method variant (CAM-B3LYP) has gained some popularity because it accounts for long-range corrections. [5] For instance, while the latter seemed to yield better TPCD results for R-(+)-3-methylcyclopentanone [6] the former performed better for R-(+)-1,1'-bis(2-naphthol) (R-BINOL). [7] Although, it is well known that common XCF are unable of providing accurate excitation energies for charge-transfer (CT) states and excitations into Rydberg states, CAM-B3LYP appears to better account for the non-local nature of CT states and correct for the asymptotic limit of many XCF in Rydberg states. However, because of the modest TPA cross-section of R-(+)-3-methylcyclopentanone [6], proving this point experimentally was impossible on this molecule.

In order to expand knowledge on this subject, in this chapter we present the theoretical-experimental study of the polarization dependent TPA of (S)-(+)-(1,1′-Binaphthalene-2,2′-diyl)bis(diphenylphosphine) (S-BINAP) in solution, a well-known axially dissymmetric diphosphine ligand extensively used as an asymmetric chiral catalyst in industry, see Figure 5-1. [8, 9] The theoretical-experimental analysis of its TPCD spectrum and the comparative examination of B3LYP and CAM-B3LYP, using the 6-31G* basis set, shows that the latter is more reliable than the former in molecules such as S-BINAP, i.e. a heteroaromatic diphosphine chiral ligand

with strong ICT. We performed extended calculations over more electronic excited states *in vacuo* for the verification of the correct assignment of the experimental bands in relatively large molecules.

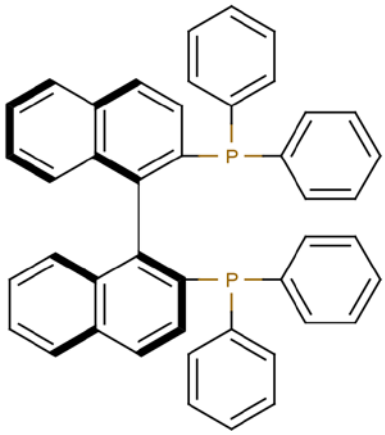

Figure 5-1. Molecular structure of S-BINAP

5.2 Experimental Section

S-BINAP (97%) in high enantiomeric excess (enantiomeric ratio *S*:*R* ≥ 99:1) was purchased from Sigma-Aldrich Co. and used as received. The TPA and TPCD measurements were performed in a 66 mM solution of S-BINAP/THF in a 1 mm thick quartz cuvette, employing the double-L scan technique. [10] Two-photon excitation was induced with a computer-controlled femtosecond optical parametric amplifier (OPerA Solo) pumped by an amplified laser system from COHERENT. The whole systems is capable of generating 90 fs (FWHM) pulses over a wavelength range that spans from 240 nm to 2.6 μm, and with pulse energies up to 3 mJ at a 1-kHz repetition rate. Experiments were performed between 410 nm to 600 nm, using pulse energies ranging from 0.2 to 0.8 μJ, and at 50Hz repetition rate to prevent accumulative effects. The pulse width was determined using a single shot autocorrelator from Coherent Inc. and a frequency-resolved optical gaiting (FROG) from Swamp Optics LLC.

5.3 Computational Methods

The theoretical background involved in this research has been given in detail in references 6, 11-15 and is also presented in sections 1.2 and 1.5 of the introduction to this dissertation. Therefore, in this part we only present the computational details relevant to the corresponding calculations.

The molecular structure of S-BINAP was optimized using Density Functional Theory (DFT) [16, 17], employing B3LYP hybrid functional [1-3], and the 6-31G* basis set [18] under C_2 geometry restrictions. The OPA spectrum was calculated using the optimized molecular structure employing time-dependent DFT (TD-DFT). [16, 17] Two different XCF were used, B3LYP and CAM-B3LYP, [5] with the 6-31G* basis set. The first 180 electronic excited states were calculated with the former XCF, while 80 were computed with the later. Solvent effects for THF were considered under the polarizable continuum model (PCM). [19, 20] The TPA and TPCD spectra were calculated for the first 40 electronic excited states at the B3LYP/6-31G*/THF and CAM-B3LYP/6-31G*/THF levels of theory. The convolution of the OPA, TPA and TPCD spectra were obtained employing Equations 1-13, 1-18 and 1-37 (see dissertation introduction), respectively, using a normalized Lorentzian lineshape (See Equation 1-15 in dissertation introduction) with a linewidth (Γ) of 0.38 eV (FWHM) for the linear spectra and 0.25 eV (FWHM) for the nonlinear spectra. In addition, the TPA and TPCD spectra of S-BINAP were obtained for the first 80 electronic excited states using the same combination of XCF and basis set but *in vacuo*. The use of PCM for these last set of calculations proved to be a challenge to our computational resources. The geometry optimization and OPA calculation were carried out in Gaussian 09 [21] and the TPA and TPCD spectra were obtained using DALTON 2011. [22]

5.4 Results and discussion

The experimental and the theoretical absorption spectra of S-BINAP are shown in Figure 5-2. One can notice a very good agreement between the experimental spectrum and the theoretical using both methods. On the one hand, the strong band centered at ~220 nm is clearly reproduced by both methods with only small variations in the overall band shape. On the other hand, the broader band at ~285 nm is better reproduced by B3LYP than CAM-B3LYP. Nevertheless, transition 2 in CAM-B3LYP would better account for this band by adjusting the linewidth. Finally, it should be emphasized that B3LYP required twice as many excited states than CAM-B3LYP to fully reproduce the experimental UV-vis spectrum.

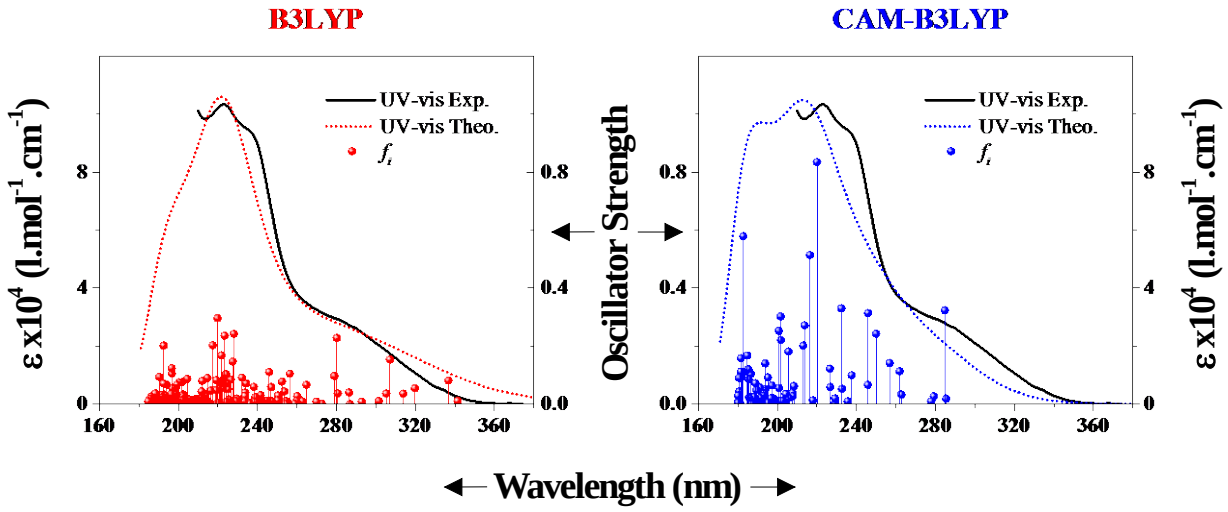

Figure 5-2. Experimental (solid black line) and theoretical (colored dotted lines) UV-vis spectra. Colored spheres display the oscillator strengths. B3LYP (left) and CAM-B3LYP (right).

Next, in Figure 5-3, we show the experimental TPA and TPCD spectra of S-BINAP measured between 410 nm to 600 nm. Measurements at shorter or longer wavelengths were not possible due to experimental limitations. Because S-BINAP/THF does not present OPA above ~360 nm (see Figure 5-2), the presence of resonance enhanced TPA [23] was discarded. Next, we

would like to comment on the approximately 20 fold decrease in the measured TPA cross-sections obtained in S-BINAP compared to previously reported values in similar molecules (BINOL, VANOL, VAPOL) [24, 25] using picosecond pulses. This apparent but not unpredictable discrepancy is mainly attributed to the pulse duration of the excitation source employed in each case – it is known that in the picosecond regime TPA cross-sections can be enhanced by the contribution of excited-state absorption (ESA) [26]. The first observation in Figure 5-3 is the presence of four intense TPA bands centered at approximately 420, 470, 540 and 580 nm, and with larger TPA cross-section on the shorter excitation wavelength region.

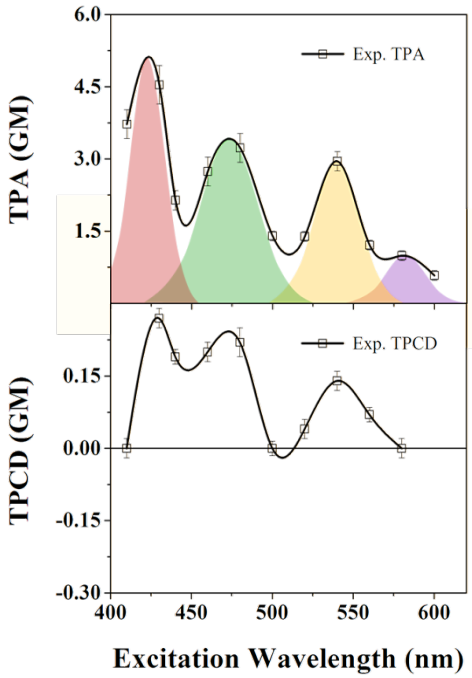

Figure 5-3. Experimental TPA (a) and TPCD (b) spectra of S-BINAP in THF. Solid black lines connecting the TPA and TPCD scattered squares are shown as a guidance only.

Because no study has specifically addressed the nature of S-BINAP electronic transitions – to the best of our knowledge – the assignment of the bands was made based on spectroscopic data available for β-naphtyldiphenylphosphine (hereafter h-BINAP) [27], a molecule that

corresponds to half of S-BINAP. This approach is justified considering the nearly perpendicular (86.9º) dihedral angle between the two h-BINAP in S-BINAP which breaks the electronic conjugation at the center of the molecule. [28, 29] According to Schindlbauer *et. al.* [27], there are three main bands in the UV-vis spectrum of h-BINAP (228 nm, 262 nm and 326 nm) which correspond to π-π* transitions and a small shoulder at around 295 nm whose nature is not disclosed. While the two higher energy bands can be associated to those observed in the TPA spectrum at 470 nm and 540 nm, respectively, the longer wavelength TPA band seems to match with that at around 295 nm. The slight spectral shift noticed between the position of the corresponding bands in the linear and the nonlinear spectra (plotted at half of the excitation wavelength) is primarily attributed to solvent effects (ethanol *vs.* THF). Next, the additional band observed on the blue side of the spectrum (420 nm) is known to correspond to contributions coming from the tails of two adjacent bands, i.e. that of the π-π* transitions of the C=C centered at about 180 nm (360 nm in the TPA scale) and that of ring resonance of benzene located at approximately 230 nm (460 nm in the TPA scale) [24]. Next, it can be noticed that the TPCD spectrum is positive throughout the measured region and exhibits a splitted band with two peaks centered at ca. 430 and 470 nm, and a well-defined band at approximately 540 nm.

In order to perform the comparative examination of XCF, we first computed the theoretical TPA and TPCD spectra of S-BINAP in THF solution over the first 40 electronic excited states, at B3LYP/6-31G* and CAM-B3LYP/6-31G* levels of theory including solvent effects using PCM. Figure 5-4.a and 5-4.b display the theoretical and experimental TPA spectra of S-BINAP/THF. First, both XCF yield four different clusters of transitions (see colored half-filled circles) corresponding to each experimental band – the colored arrows placed on the top of the each band indicate the bundle of transitions contributing to it. Second, there is a notable

spectral red-shift of ca. 100 nm in B3LYP (Figure 5-4.a) and a small blue-shift of less than 10 nm in CAM-B3LYP (Figure 5-4.b). In addition, when comparing the theoretical Lorentzian convolutions with the experimental spectrum (Figures 5-4.a and 5-4.b) one can notice a difference in magnitude on the TPA cross-sections for both XCF and the experiment.

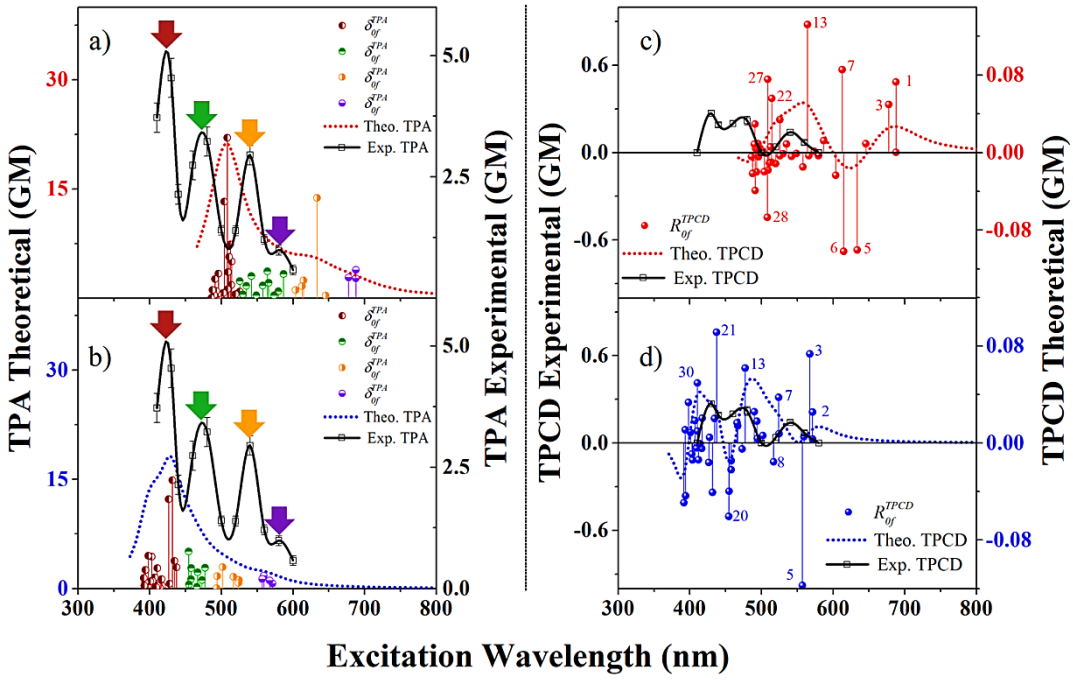

Figure 5-4. Experimental TPA (left) and TPCD (right) spectra (black scattered squares) of S-BINAP and its theoretical TPA (a, b) and TPCD (c, d) spectra (colored dotted lines) calculated with B3LYP/6-31G*/PCM (top) and CAM-B3LYP/6-31G*/PCM (bottom), over the first 40 electronic excited states (scattered colored half-filled circles). The convoluted spectra were obtained using normalized Lorentzian lineshape functions with a linewidth (Γ) of 0.2 eV (FWHM). Arrows flagging the experimental TPA bands indicate the color of the bundle of electronic transitions associated to those bands.

The spectral shift is ascribed to limitations of the methods and the fact that PCM does not consider specific solute−solvent interactions (See Section 2.3.1 in the introduction of this dissertation). The difference in the TPA cross-sections can be partially attributed to the linewidth employed for the Lorentzian lineshape function. Γ = 0.25 eV (FWHM) was intentionally chosen to compute the best TPCD spectrum of S-BINAP/THF. However, a better theoretical–

experimental match in TPA cross-sections could be achieved employing an unusually large linewidth Γ = 2.5 eV. Therefore, the observed difference in magnitude should be regarded as a partial theoretical-experimental divergence whose origin still remains unclear to us. In brief, the better agreement obtained for CAM-B3LYP was not totally unexpected since it has been shown that it accounts for long-range corrections in molecules with strong ICT [5, 7, 14, 30]. Therefore, this XCF was predicted to be more reliable for calculating the TPA spectrum of S-BINAP. Finally, besides the remarkable difference in spectral shift between the two XCF, there is also a difference in relative contribution of excited state 5 (~630 nm), being significantly larger for B3LYP than in CAM-B3LYP.

In order to elucidate the origin of these differences we performed a thorough molecular orbitals (MOs) analysis of the electronic excited states. MOs were calculated using TD-DFT at the B3LYP/6-31G* and CAM- B3LYP/6-31G* levels of theory in THF using PCM. All calculations were performed in Gaussian 09. The direct comparison between the MOs computed with both XCF reveal remarkable similarities for most them. Nevertheless, the following important differences are noticed (See Figure 5-5):

a) LUMO+6 in B3LYP correspond to LUMO+7 in CAM-B3LYP and vice-versa.

b) HOMO-7 in B3LYP corresponds to HOMO-8 in CAM-B3LYP and vice-versa.

This observation is supported by a similar cross-correspondence in symmetry and closeness in MO energy in both cases (See Table 5-1). Another remarkable difference that can be observed in Figure 5-5 is the complete inversion in LUMO and LUMO+8 and the significant changes in electronic density seen in HOMO-1, HOMO-2, and HOMO-10. In order to assess the

influence of these variations onto the calculated electronic transitions, an analysis of their contribution to each excited state is required.

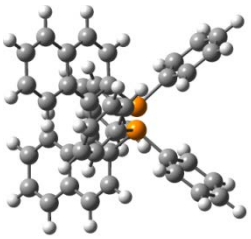

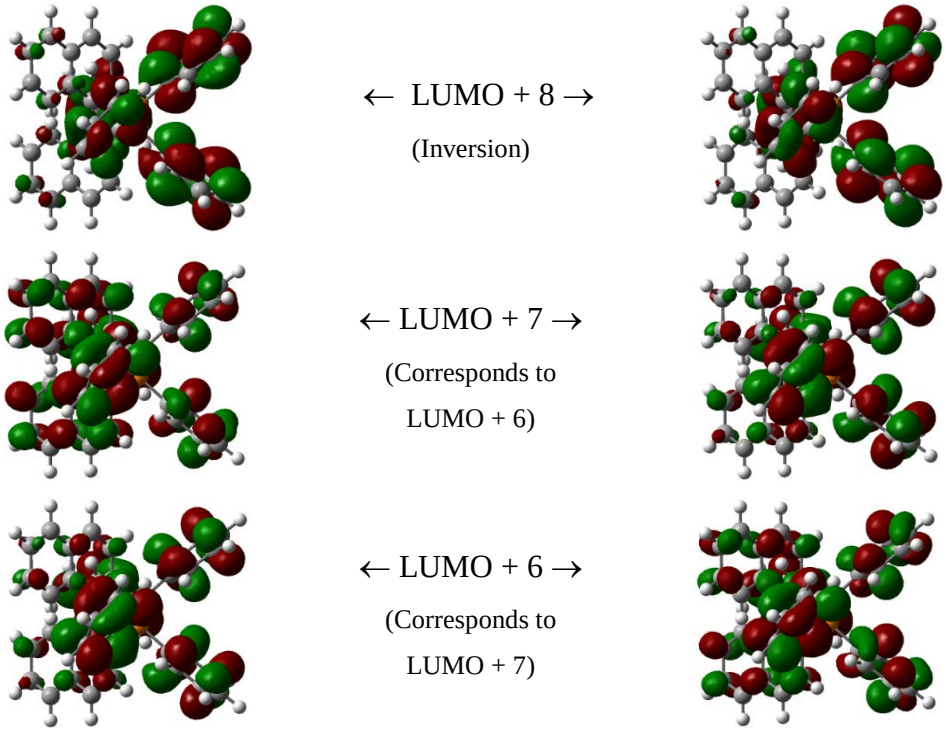

Figure 5-5. Molecular orbitals calculated using TD-DFT at the B3LYP/6-31G* and CAM- B3LYP/6-31G* levels of theory in THF using PCM. Only MOs presenting differences between methods are shown.

B3LYP	Molecular Orbital (observation)	CAM-B3LYP
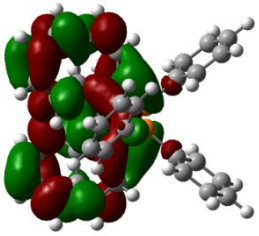	← LUMO → (Inversion)	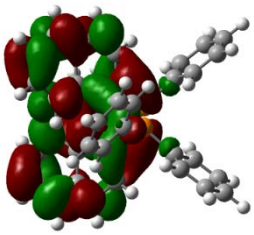
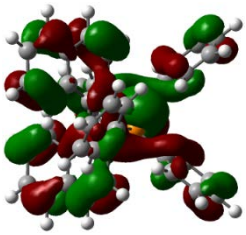	← HOMO - 1 → (Distribution of electronic density)	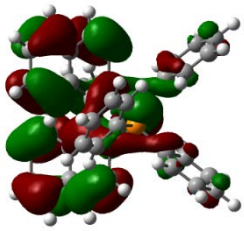
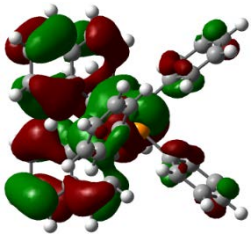	← HOMO - 2 → (Distribution of electronic density)	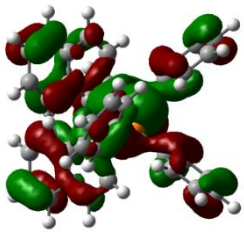
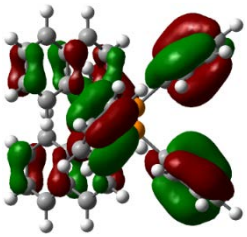	← HOMO - 7 → (Corresponds to HOMO - 8)	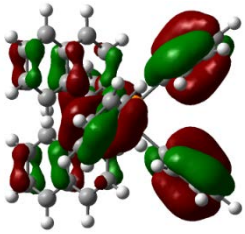
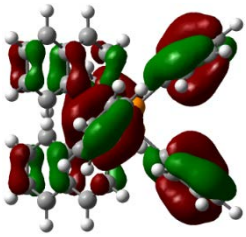	← HOMO - 8 → (Corresponds to HOMO - 7)	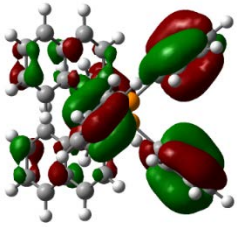
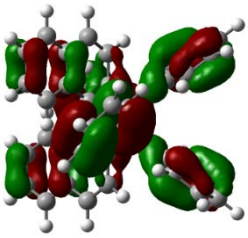	← HOMO - 10 → (Distribution of electronic density)	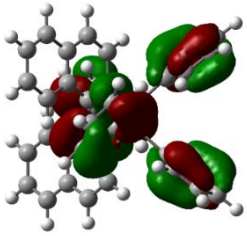

Figure 5-5. (continued).

Table 5-1. B3LYP and CAM-B3LYP energies and symmetries of HOMO and LUMO and the MOs presenting differences in symmetry between methods. Calculations were performed using TD-DFT at the B3LYP/6-31G* and CAM- B3LYP/6-31G* levels of theory in THF using PCM.

	B3LYP		CAM-B3LYP	
MO	*E* (eV)	Symm.	*E* (eV)	Symm.
LUMO+7	-0.18	B	1.12	A
LUMO+6	-0.19	A	1.11	B
LUMO	-1.34	A	-0.17	A
HOMO	-5.60	A	-6.91	A
HOMO-7	-6.89	B	-8.34	A
HOMO-8	-6.89	A	-8.34	B

The excitations contributing to the first 40 electronic excited states of S-BINAP/THF were calculated at the B3LYP/6-31G* and CAM-B3LYP/6-31G* levels of theory using PCM (See Appendix E). The analysis of this data revealed that the first three electronic transitions yield very similar results with both XCF. Then, in transition four, one can observe some differences in contribution from excitations between different MOs. However, it is not until transition five that truly remarkable differences in excitations for the different XCF become obvious. In addition, above this excited state the vast majority of the electronic transitions exhibit differences in symmetry.

Interesting to remark is the fact that in most transitions (3-25) HOMO-2 has a strong contribution in at least in one of the XCF. This result proves that changes in electronic density on HOMO-2 play a decisive role in the observed differences between the theoretical TPA spectra of both XCF.

The energy data presented in Table 5-1 helps to identify the origin of the observed differences in spectral position for the electronic transitions calculated using both XCF. The HOMO-LUMO band gap is 4.26 eV and 6.74 eV for B3LYP and CAM-B3LYP, respectively. The larger energy difference for the latter explains why CAM-B3LYP spectra are consistently blue shifted with respect to those calculated using the former.

Next, in Figure 5-4.c and 5-4.d we show the comparative plots of the experimental TPCD spectrum of S-BINAP and, the corresponding theoretical spectra computed with the two XCF under study. In Figure 5-4.c (B3LYP), it seems that the two main positive bands observed in the theoretical TPCD spectrum, the one centered at 550 nm and that at 690 nm ought to correspond to the experimental splitted band observed at around 450 nm (with two peaks at 430 and 470 nm) and that at approximately 540 nm, respectively. Respecting this spectral assignment, the negative feature at 620 nm should correlate to the experimental minimum at 510 nm while the small negative band at 480 nm could be related to the experimental decreasing tendency observed on the spectrum below 420 nm. In Figure 5-4.d (CAM-B3LYP), the theoretical-experimental correspondence between all the positive bands lead to the following tentative assignment: the two peaks at approximately 410 and 490 nm should correspond to the splitted band with maxima at 430 and 470 nm, and that at 580 nm should correspond to the less intense band at around 540 nm. From the two negative bands, observed at approximately 450 nm and 390 nm, the latter seems to follow the experimental decreasing tendency observed below 420 nm while the former is tentatively assigned to the positive minimum centered at approximately the same wavelength. The experimental minimum seen at ca. 510 nm is assigned to the theoretical minimum observed at 550 nm. Yet the agreement between all the spectral features observed in Figure 5-4.d is reasonably good, the relative position of the bands is not perfectly reproduced. Therefore, before

drawing any definite conclusions, it is important to recall the theoretical-experimental study of TPCD on R-BINOL [7] where Hernandez and co-workers demonstrated the importance of carefully checking that the necessary number of excited states needed to fully reproduce the experimental spectrum has been achieved.

In S-BINAP, it seems that a full reproduction of the measured spectral region is attained with both XCF, with only 40 electronic excited states. However, since TPCD is the result of a series of complex positive and negative $R_{0f}^{TPCD}\left(\omega_{0f}\right)$ contributions, [31] the addition of more excited states can significantly change the overall shape of the envelop, mainly on the blue end of the TPCD spectra. Unfortunately, performing similar type of calculations (B3LYP/6-31G*/PCM and CAM-B3LYP/6-31G*/PCM) over a larger number of excited states and including solvent effects proved to be overdemanding to our computational resources. In an effort to assess whether or not 40 electronic excited states was indeed enough to fully reproduce the experimental spectrum, we extended our analysis to the first 80 electronic excited states removing the inclusion of solvent effects *via* PCM. Although, this approach has been proven to substantially reduce the complexity of the task, [7] it could in principle also significantly affect the outcome.

In Figure 5-6 we show the theoretical TPA and TPCD spectra of S-BINAP *in vacuo*, calculated over the first 80 electronic excited states with B3LYP (top) and CAM-B3LYP (bottom). It can be noticed that the position and intensities of most of the transitions shown in the previous TPA spectra (Figure 5-4.a and 5-4.b) are virtually unchanged when going from 40 to 80 electronic excited states. The main difference is the number of additional electronic transitions at shorter wavelengths which enhances the overall intensity of the strongest TPA band on the blue (see Figure 5-6.a and 5-6.b). These results indicate that not including PCM in S-BINAP

calculations should not significantly affect the accuracy on the computed TPA and TPCD spectra. Therefore, one can view these calculations as a valid extension of those including solvent effects.

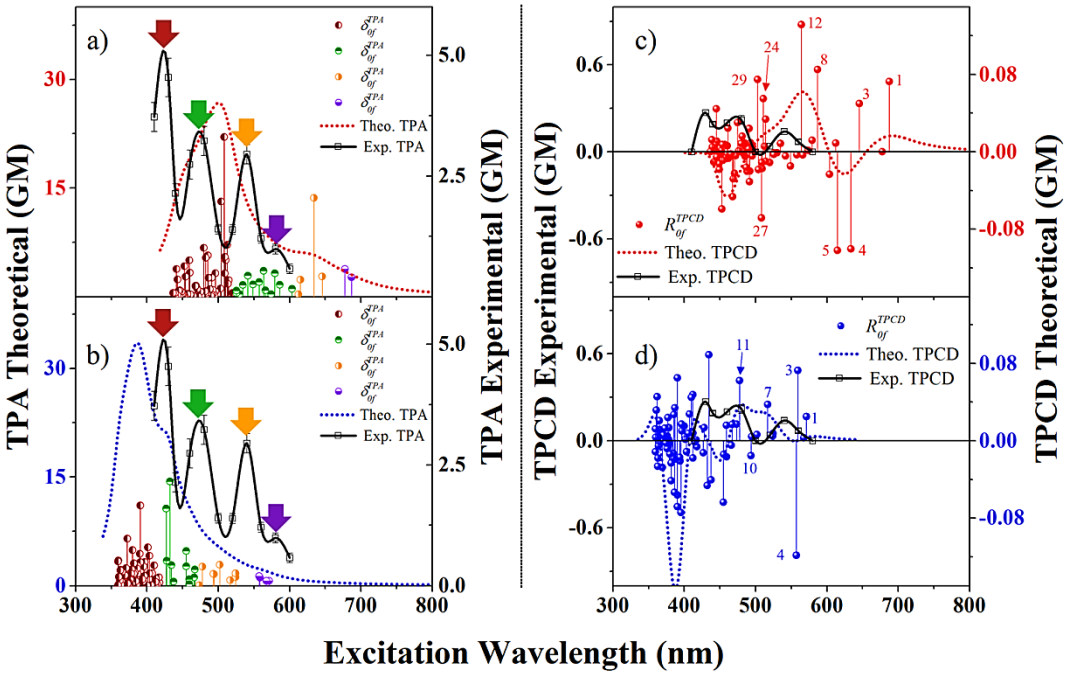

Figure 5-6. Experimental TPA (left) and TPCD (right) spectra (black scattered squares) of S-BINAP and its theoretical TPA (a, b) and TPCD (c, d) spectra (colored dotted lines) calculated with B3LYP/6-31G*/vacuo (top) and CAM-B3LYP/6-31G*/vacuo (bottom), over the first 80 electronic excited states (scattered colored half-filled circles). The convoluted spectra were obtained using normalized Lorentzian lineshape functions with a linewidth (Γ) of 0.2 eV (FWHM). Arrows flagging the experimental TPA bands indicate the color of the bundle of electronic transitions associated to those bands.

In Figure 5-6.c and 5-6.d we present the experimental TPCD spectrum of S-BINAP and the corresponding theoretical TPCD spectra computed using the same XCF *in vacuo*. On the one hand, one can notice that the calculations using the B3LYP functional now yield a well-defined negative band centered at approximately 450 nm which is mostly caused by the sum of contributions originated from the additional higher energy transitions. Additionally, the relatively small change in the spectral shape is attributed to the spectral shift of certain transitions and their

corresponding contribution to $R_{0f}^{TPCD}\left(\omega_{0f}\right)$. This effect is primarily produced by the removal of PCM from the calculation. Nevertheless, the two positive bands can still be associated with those on the experimental TPCD spectrum but with a rather large spectral red-shift of ~120 nm (virtually the same spectral shift obtained using PCM). On the other hand, the TPCD spectrum obtained with CAM-B3LYP is greatly affected by the additional 40 electronic excited states. The cluster of negative transitions at around 385 nm has a significant effect on decreasing, by more than two folds, the intensity of the positive band that used to be located at 410 nm on the PCM calculation. The summation over all $R_{0f}^{TPCD}\left(\omega_{0f}\right)$ makes of the negative band at approximately 450 nm a more prominent spectral feature. These obvious spectral changes indicate that the PCM calculation over only the first 40 electronic excited states did not include the necessary number of excited states needed to fully reproduce the experimental spectrum. To confirm this statement, in Figure 5-7 we present the experimental and same theoretical TPCD spectrum (CAM-B3LYP/6-31G*, in *vacuo* and over the first 80 electronic excited states) shifted by 40 nm to the blue. Now, the outstanding theoretical-experimental spectral match permits to perform a one-to-one assignment of the electronic transition contributing to the different bands: transition 1, 3 and 4 reproduce the positive band centered at 540 nm with a weaker relative intensity due to the negative contribution from transition 4 and the minimum at 510 nm; the two overlying bands with peaks at 430 and 470 nm are primary determined by the presence of transitions 11 and 7, respectively; finally transition 10 is accountable for the small valley observed at 450 nm.

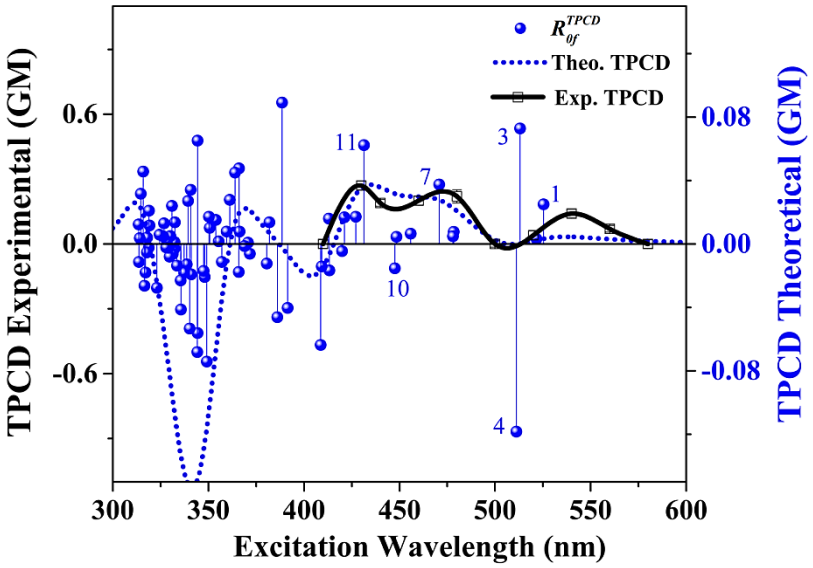

Figure 5-7. Experimental TPCD spectrum of S-BINAP (scattered squares) and the theoretical TPCD spectrum calculated *in vacuo* over the first 80 electronic excited states (scattered spheres) at the CAM-B3LYP/6-31G* level of theory (Theoretical spectrum is blue shifted 40nm). The convoluted spectra were obtained using normalized Lorentzian lineshape functions with a linewidth (Γ) of 0.2 eV (FWHM).

In an effort to enlighten the better performance of CAM-B3LYP in predicting the TPCD spectrum of S-BINAP we completed a molecular orbital (MOs) analysis on the states involved in the most important transitions defining the TPCD spectrum of this molecule. The calculation of the molecular orbitals were carried out in Gaussian 09 [21] using TD-DFT at the CAM-B3LYP/6-31G* level of theory *in vacuo* for the first 80 excited states. Figure 5-8 display the molecular orbitals involved in transitions 1, 3, 4, 7, 10, 11 (see Figure 5-7).

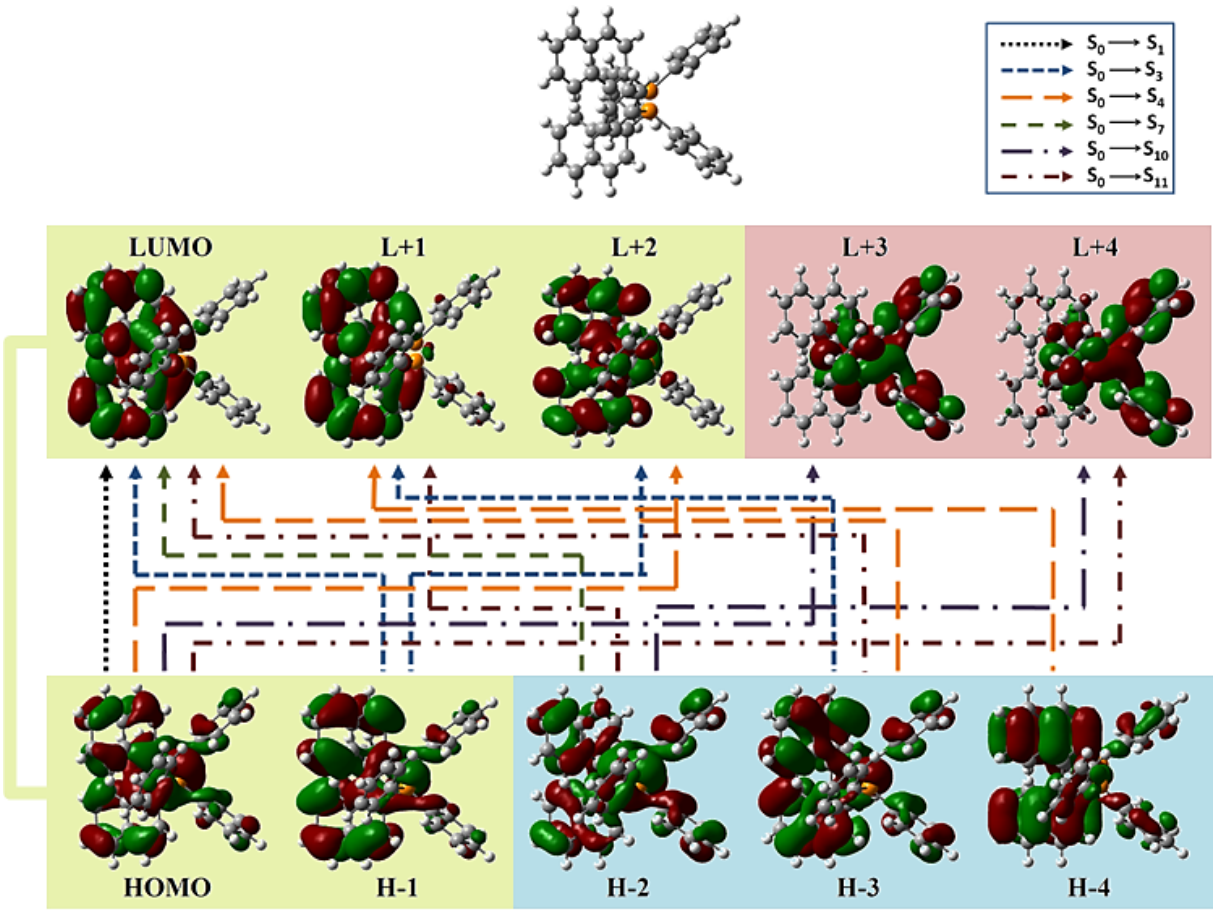

Figure 5-8. Molecular orbitals of S-BINAP (HOMO – 4 to LUMO +4) calculated with CAM-B3LYP/6-31G* TD-DFT calculation in vacuo. Different types of lines (see legend) indicate [HOMO – x] → [LUMO + y] excitations that belong to a specific S0 → Sn electronic transition.

First, it can be noticed the presence of localized MOs, i.e. electron density mostly on the two naphthyl rings in HOMO and H-1 as well as in LUMO, L+1 and L+2, and charge distribution shifted primarily to the opposite side of the molecule (on the phenyl rings) in LUMO+3 and LUMO+4. In H-2, H-3 and H-4 the electron density is distributed more evenly along the whole molecule. Interesting to highlight is the existence of diffuse MOs around the two phosphorus atoms located at the center of the molecule in most HOMOs and in LUMO+3 and LUMO+4. These three descriptions on electron density redistribution in S-BINAP evidences the significant charge transfer (CT) component present in this molecule and therefore support the

observed improved performance on TPCD calculations using CAM-B3LYP, an XCF that corrects the existent deficiencies of the popular B3LYP regarding the treatment of CT states [5, 7, 14, 30].

5.5 Conclusions

The study of TPCD response of S-BINAP demonstrated that CAM-B3LYP outperformed the popular B3LYP due to the presence of ICT states in this heteroaromatic diphosphine chiral ligand. We showed that substantially extending the manifold of states included in the TD-DFT calculation is crucial for the proper assignment of theoretical electronic transitions to experimental bands. The inclusion of additional electronic excited states in the calculation has a stronger effect on the shape of the theoretical spectra at shorter wavelengths. Having completed this part of our study, the question to answer next is if the nature of the ICT also has an effect on the TPCD signal of conjugated molecules.

5. 6 References

1. Becke, A. D., Density-Functional Exchange-Energy Approximation with Correct Asymptotic Behavior. *Phys. Rev. A* **1988,** *38*, 3098-3100.

2. Becke, A. D., Density-Functional Thermochemistry. III. The Role of Exact Exchange. *J. Chem. Phys.* **1993,** *98*, 5648-5652.

3. Lee, C.; Yang, W.; Parr, R. G., Development of the Colle-Salvetti Correlation-Energy Formula into a Functional of the Electron Density. *Phys. Rev. B: Condens. Matter* **1988,** *37*, 785-789.

4. Sousa, S. F.; Fernandes, P. A.; Ramos, M. J., General Performance of Density Functionals. *J. Phys. Chem. A* **2007,** *111*, 10439-10452.

5. Yanai, T.; Tew, D. P.; Handy, N. C., A new Hybrid Exchange-Correlation Functional using the Coulomb-Attenuating Method (CAM-B3LYP). *Chem. Phys. Lett.* **2004,** *393*, 51-57.

6. Rizzo, A.; Lin, N.; Ruud, K., Ab Initio Study of the One- and Two-Photon Circular Dichroism of R-(+)-3-Methyl-Cyclopentanone. *J. Chem. Phys.* **2008,** *128*, 164312.

7. Lin, N.; Santoro, F.; Zhao, X.; Toro, C.; De Boni, L.; Hernández, F. E.; Rizzo, A., Computational Challenges in Simulating and Analyzing Experimental Linear and Nonlinear Circular Dichroism Spectra. R-(+)-1,1'-bis(2-naphthol) as a Prototype Case. *J. Phys. Chem. B* **2011,** *115*, 811-824.

8. Noyori, R.; Takaya, H., BINAP: an Efficient Chiral Element for Asymmetric Catalysis. *Acc. Chem. Res.* **1990,** *23* (10), 345-350.

9. Akutagawa, S., Asymmetric Synthesis by Metal BINAP Catalysts. *Applied Catalysis A: General* **1995,** *128* (2), 171-207.

10. De Boni, L.; Toro, C.; Hernandez, F. E., Synchronized Double L-Scan Technique for the Simultaneous Measurement of Polarization-Dependent Two-Photon Absorption in Chiral Molecules. *Opt. Lett.* **2008,** *33*, 2958-2960.

11. Rizzo, A.; Jansík, B.; Pedersen, T. B.; Agren, H., Origin Invariant Approaches to the Calculation of Two-Photon Circular Dichroism. *J. Chem. Phys.* **2006,** *125*, 64113.

12. Jansík, B.; Rizzo, A.; Agren, H., Ab Initio Study of the Two-Photon Circular Dichroism in Chiral Natural Amino Acids. *J. Phys. Chem. B* **2007,** *111*, 446-460.

13. Jansík, B.; Rizzo, A.; Ågren, H.; Champagne, B., Strong Two-Photon Circular Dichroism in Helicenes: A Theoretical Investigation. *J. Chem. Theory Comput.* **2008,** *4*, 457-467.

14. Lin, N.; Santoro, F.; Rizzo, A.; Luo, Y.; Zhao, X.; Barone, V., Theory for Vibrationally Resolved Two-Photon Circular Dichroism Spectra. Application to (R)-(+)-3-Methylcyclopentanone. *J. Phys. Chem. A* **2009,** *113*, 4198-4207.

15. Guillaume, M.; Ruud, K.; Rizzo, A.; Monti, S.; Lin, Z.; Xu, X., Computational Study of the One- and Two-Photon Absorption and Circular Dichroism of (L)-Tryptophan. *J. Phys. Chem. B* **2010,** *114*, 6500-6512.

16. Runge, E.; Gross, E. K. U., Density-Functional Theory for Time-Dependent Systems. *Phys. Rev. Lett.* **1984,** *52*, 997-1000.

17. Dierksen, M.; Grimme, S., A Theoretical Study of the Chiroptical Properties of Molecules with Isotopically Engendered Chirality. *J. Chem. Phys.* **2006,** *124*, 174301.

18. Rassolov, V. A.; Pople, J. A.; Ratner, M. A.; Windus, T. L., 6-31G* Basis Set for Atoms K through Zn. *J. Chem. Phys.* **1998,** *109*, 1223-1229.

19. Mennucci, B.; Tomasi, J.; Cammi, R.; Cheeseman, J. R.; Frisch, M. J.; Devlin, F. J.; Gabriel, S.; Stephens, P. J., Polarizable Continuum Model (PCM) Calculations of Solvent Effects on Optical Rotations of Chiral Molecules. *J. Phys. Chem. A* **2002,** *106*, 6102-6113.

20. Tomasi, J.; Mennucci, B.; Cammi, R., Quantum Mechanical Continuum Solvation Models. *Chem. Rev.* **2005,** *105*, 2999-3093.

21. Frisch, M. J.; Trucks, G. W.; Schlegel, H. B.; Scuseria, G. E.; Robb, M. A.; Cheeseman, J. R.; Scalmani, G.; Barone, V.; Mennucci, B.; Petersson, G. A., *et al.*, Gaussian 09, Revision A.1. Gaussian, Inc.: Wallingford CT, 2009.

22. DALTON *A Molecular Electronic Sstructure Program, Release Dalton 2011, see* *http://daltonprogram.org/*, 2011.

23. Day, P. N.; Nguyen, K. A.; Pachter, R., TDDFT Study of One- and Two-Photon Absorption Properties: Donor-π-Acceptor Chromophores. *J. Phys. Chem. B* **2005,** *109*, 1803-1814.

24. Toro, C.; De Boni, L.; Lin, N.; Santoro, F.; Rizzo, A.; Hernandez, F. E., Two-Photon Absorption Circular Dichroism: A New Twist in Nonlinear Spectroscopy. *Chem. Eur. J.* **2010,** *16*, 3504-3509.

25. Diaz, C.; Lin, N.; Toro, C.; Passier, R.; Rizzo, A.; Hernández, F. E., The Effect of the π-Electron Delocalization Curvature on the Two-Photon Circular Dichroism of Molecules with Axial Chirality. *J. Phys. Chem. Lett.* **2012,** *3*, 1808-1813.

26. Belfield, K. D.; Bondar, M. V.; Hernandez, F. E.; Przhonska, O. V.; Yao, S., Two-photon absorption cross section determination for fluorene derivatives: analysis of the methodology and elucidation of the origin of the absorption processes. *J. Phys. Chem. B* **2007,** *111*, 12723-12729.

27. Schindlbauer, H.; Hagen, H., Die Ultraviolettspektren einiger Phosphine und Phosphinoxide, die den Benzol-, Naphthalin- und Anthracenkern enthalten. *Monatshefte für Chemie und verwandte Teile anderer Wissenschaften* **1965,** *96*, 285-299.

28. Diaz, C.; Echevarria, L.; Hernández, F. E., Overcoming the Existent Computational Challenges in the Ab Initio Calculations of the Two-Photon Circular Dichroism Spectra of Large Molecules using a Fragment-Recombination Approach. *Chem. Phys. Lett.* **2013,** *568-569*, 176-183.

29. Díaz, C.; Echevarria, L.; Hernández, F. E., Conformational Study of an Axially Chiral Salen Ligand in Solution using Two-Photon Circular Dichroism and the Fragment-Recombination Approach. *J. Phys. Chem. A* **2013,** *117*, 8416–8426.

30. Rizzo, A.; Coriani, S.; Ruud, K., Response Function Theory Computational Approaches to Linear and Nonlinear Optical Spectroscopy. In *Computational Strategies for Spectroscopy*, John Wiley & Sons, Inc.: 2011; pp 77-135.

31. Hernández, F. E.; Rizzo, A., Two-Photon Polarization Dependent Spectroscopy in Chirality: a Novel Experimental-Theoretical Approach to Study Optically Active Systems. *Molecules (Basel, Switzerland)* **2011,** *16*, 3315-3337.

CHAPTER 6 : TWO-PHOTON ABSORPTION AND TWO-PHOTON CIRCULAR DICHROISM OF HEXAHELICENE DERIVATIVES: A STUDY OF THE EFFECT OF THE NATURE OF INTRAMOLECULAR CHARGE TRANSFER

Reproduced with permission of the American Chemical Society from: C. Díaz, Y. Vesga, L. Echevarria, I. Stará, I. Starỳ, E. Anger, C. Shen, M. El Sayed Moussa, N, Vanthuyne, J. Crassous, A. Rizzo, F.E. Hernández, RSC Adv. ***2015****, 5, 17429–17437*

Having arrived to general conclusions on the effect of ICT onto the TPCD signal of conjugated chiral molecules in Chapter IV, we decided to embark on a new investigation on the effect of the nature of ICT on the TPCD signal of systems with helical chirality.

Herein, we present the theoretical-experimental analysis of the ECD and TPCD spectra of two hexahelicene derivatives exhibiting intramolecular charge transfer (ICT). The primary outcomes of our investigation demonstrate that the TPA cross-section and the amplitude of the TPCD signal of this type of helicenes are not strongly affected by the strength of the ICT but by the nature of the extension of the electronic delocalization, i.e. beyond (EXO-ICT) or within (ENDO-ICT) the helicene core. In order to corroborate our results we performed a comparative theoretical analysis of the corresponding contributions of the magnetic dipole transition moment and the electric quadrupole transition moment to the TPCD rotatory strength on a series of five similar helicene derivatives with different molecular electron delocalization disposition.

6.1 Introduction

Seeking for a better understanding of TPCD and its structure-property relationship we have been working on the theoretical-experimental analysis of the TPCD response of several systems. [1-7] Although all these studies have contributed to the expanded knowledge of TPCD in organic molecules, more molecular systems need to be studied to better understand this nonlinear optical property and its potential applications. To help accomplish this goal, herein we present the results from our most recent work which was primarily focused on the first theoretical-experimental analysis of the TPA and TPCD spectra of two interesting aromatic molecules - hexahelicene derivatives - with helical chirality and intramolecular charge transfer (ICT) (see Figure 1.a for their chemical structures). One should remark that helicenes are very popular chiral systems employed in applications involving chiroptical photoswitches, [8] enantioselective fluorescence detectors, [9] circularly polarized luminescence for back-lighting in liquid crystals displays, [10, 11] and nonlinear optical (NLO) devices. [12, 13]

Next, we present evidence that show that the TPA cross-section and the amplitude of the TPCD signal in helicenes are strongly affected by the strength and nature of the ICT. We demonstrate that the extension of the electronic delocalization beyond the helicene core (EXO-ICT) has a stronger effect of the nonlinear optical responses of this family of molecules than the extension of the electronic delocalization within the aromatic cluster (ENDO-ICT). This effect is directly correlated, as shown below in a series of helicene derivatives with different electron delocalization disposition (Figure 1.b), with the contributions of the magnetic dipole transition moment and the electric quadrupole transition moment to the TPCD rotatory strength of the molecules.

6.2 Experimental Section

P-(+)-1-aza[6]helicene (hereafter A6 - Figure 6-1.a) was synthesized as previously reported by Stará and co-workers. [14] Briefly, A6 (Figure 6-1.a) was prepared by using the cobalt-catalyzed intramolecular [2+2+2] cycloaddition of a pyridine-linked triyne followed by dehydrogenation with MnO_2. [14]

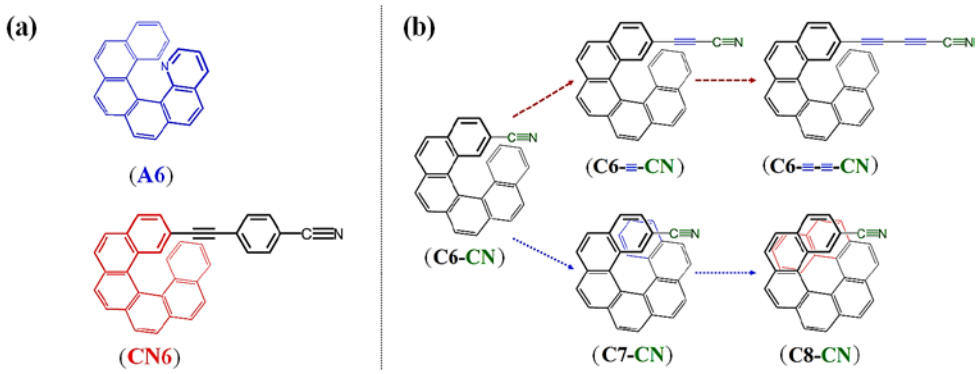

Figure 6-1. (a) Chemical structures of *P*-(+)-1-aza[6]helicene (A6)**,** and M-(-)-2-[(4-cyanophenyl)-1-ethynyl]carbo[6]helicene (CN6). **(b)** Chemical structures of CN6-like helicenes (#CN). C6–CN is the base #CN. Derivatives with increasing EXO-ICT and ENDO-ICT are in the upper row and are in the lower row, respectively.

M-(-) and *P*-(+)-2-[4-(cyanophenyl)-1-ethynyl]carbo[6]helicene (Figure 6-1.b) were obtained from racemic 2-ethynyl-[6]carbohelicene and commercially available 4-bromobenzonitrile through a Sonogashira coupling reaction followed by chiral HPLC separation. [15] Although both the *P* and *M* enantiomers were obtained for this derivative, only the *M* enantiomer (henceforth CN6) was used for the spectroscopic measurements due to impurities that could not be removed from the solution containing the *P* enantiomer.

OPA measurements were performed using a single-beam spectrophotometer (Agilent 8453 Diode Array Uv-Vis) from 190 to 600 nm in a 0.1 cm quartz cell in 0.2×10^{-4} - 2.0×10^{-4} M

solutions in THF. ECD spectra were completed on a J-815 CD spectropolarimeter (Jasco Corp., Tokyo, Japan) following these conditions: concentration 1.0 x 10^{-5} M in THF; temperature 25 ºC; quartz cuvette length 4 mm; wavelength range 190-600 nm; 1 nm step and scan speed 50 nm/min.

TPA and TPCD measurements were carried out in solutions with concentrations ranging from 3.0×10^{-2} M to 5.3×10^{-2} M, employing the double-L scan technique. [16] All samples were dissolved in THF. Two-photon excitation was induced with a computer-controlled femtosecond optical parametric amplifier (OPerA Solo) pumped by an amplified laser system from COHERENT. The whole system is capable of generating 90 fs (FWHM) pulses over a wavelength range spanning from 240 nm to 2.6 μm, and with pulse energies of up to 350 μJ. Experiments were performed at a repetition rate between 2 and 50 Hz to avoid any contribution from cumulative effects. The pulse width was measured using a single-shot autocorrelator from Coherent Inc. and a frequency-resolved optical gaiting (FROG) from Swamp Optics LLC.

6.3 Computational Methods

The theoretical background involved in this research has been given in detail in references 17-22 and is also presented in sections 1.2 and 1.5 of the introduction of this dissertation. Therefore, in this part we only present the computational details relevant to the corresponding calculations.

The molecular structures of A6 and CN6 (see Figure 6-1.a), as well as those of five CN6-like helicenes (#CN) (see Figure 6-1.b) were optimized using Density Functional Theory (DFT), [23] employing the Becke's three-parameter exchange, Lee, Yang and Parr correlation (B3LYP) hybrid functional [24-26] in combination with the 6-311++G(d,p) basis set, [27, 28]

employing Gaussian 09. [29] Solvent effects (THF) were considered as implemented in the polarizable continuum model (PCM). [30] Calculations of excited states of all helicenes, in the linear (OPA and ECD) and nonlinear (TPA and TPCD) instance, were performed employing Time-Dependent DFT (TD-DFT), [23] with two different exchange correlation functionals (XCF), i.e. B3LYP and the Coulomb attenuating method-B3LYP (CAM-B3LYP) [31]. Because it is well-known that the latter is a more reliable XCF than the former in molecules with ICT, [2, 31, 32] in this chapter we only present results obtained with CAM-B3LYP.

At this point, we would like to comment on the limitations of an inherently single-excitation based model as TD-DFT when dealing with electronic excited states dominated by double excitations. [33, 34] It is well known that in some cases, for example for polyenes or polyacenes, the TPA response can be particular intense for states with this character. [34, 35] Although, we recognize the challenges present when resorting to the computational protocol employed in this study for the study of linear and, in particular, nonlinear spectroscopies, this subject has been the theme of detailed studies within our group, cf. for instance Ref. 6. Double excitations, in the definition given usually in ab initio quantum chemistry, are somehow taken care even within standard adiabatic TD-DFT approaches using approximate functionals. [34, 36] Nevertheless, it is a fact that, when double or higher excitation character of the excited state is dominant, this model is bound to fail. Although alternative approaches to adiabatic TD-DFT, able in principle to deal with double excitations, have been proposed and developed (as the use of frequency dependent or non adibatic kernels), [33] the debate and the current development has been mostly concerned with excitation energies and linear response properties, and we are not aware of extensions to analytical nonlinear response. On the other hand the importance of multiple excitations for two-photon spectra, has been discussed also within the ab initio quantum

chemistry community, [35] and besides the well-known multiconfigurational time dependent Hartree-Fock approaches to nonlinear response [37] available in DALTON [38] now for decades -but not suitable in its current status, for the treatment of molecules of the size of those studied here - the algebraic-diagrammatic construction polarization propagator approach developed within the group of Drew and applied to octatetraene in Refs. 37, 39 and 40, appears to be a particularly promising suitable tool to treat non-linear absorption when multiple excitation are of particular importance for sizeable molecules.

Next, we computed the oscillator strengths (f_{0f}) and velocity rotatory strengths (R_{0f}^{ECD}) for the first 60 electronic excited states for all the helicene derivatives using TD-DFT at the CAM-B3LYP/6-31G(d) [41] level of theory including solvent effects (THF) *via* PCM, in Gaussian 09. [29] The convoluted theoretical UV-vis and ECD spectra were obtained using Equations 1-13 and 1-33 (see dissertation introduction), respectively, using a normalized Lorentzian lineshape (See Equation 1-15 in dissertation introduction) with a linewidth (Γ) of 0.5 eV (FWHM). **Note:** In order to certify the reliability of the selected basis set, we performed additional TD-DFT calculations over a smaller number of excited states (first 30 electronic excited states) using a larger basis set, i.e. 6-311++G(d,p). No significant differences, compared to the linear spectra computed with 6-31G(d) were obtained.

TPA probabilities $\left(\overline{\delta}_{0f}^{TPA}\left(\omega_{0f}\right)\right)$ and TPCD rotatory strength $\left(R_{0f}^{TPCD}\left(\omega_{0f}\right)\right)$ for all the helicene derivatives were calculated employing TD-DFT in DALTON 2011, [38] using CAM-B3LYP/aug-cc-pVDZ [42] for A6, and employing CAM-B3LYP/6-311++G(d,p) for the rest of the helicene derivatives. For TPA and TPCD, the number of electronic excited states selected for A6 (60 & 48) and CN6 (60 & 40), were determined by the experimental spectral range (200 nm –

450 nm) covered during the measurements. In #CN derivatives the number of electronic excited states to be considered in the calculations were established by the measured experimental spectral range for CN6 (see captions for Figures 6-4 and 6-5 for the accurate number of electronic excited states employed for each derivative). No solvent effects were considered in the nonlinear calculations due to the high computational costs. The convoluted theoretical TPA and TPCD spectra were obtained employing Equations 1-18 and 1-37 (see dissertation introduction), respectively, using a normalized Lorentzian lineshape (See Equation 1-15 in dissertation introduction) with a linewidth (Γ) of 0.15 eV (FWHM).

6.4 Results and discussion

In order to start with the analysis, in Figure 6-2 we present the experimental OPA and ECD spectra of A6 (Top) and CN6 (Bottom) in THF solution, and their corresponding convoluted CAM-B3LYP stick spectra, calculated in THF using PCM and basis set 6-31G(d) (Assignment of theoretical excited states to experimental bands can be found in Tables 6-1.a and 6-1.b). To obtain a better match with the experiment, the theoretical spectra were spectrally shifted by an amount reported in the caption of the figure (this is common practice in theoretical-experimental works). [2, 3, 5-7] One should mention that the theoretical curves are consistently blue shifted with respect to the experimental. This result is not surprising since, as it has been previously reported,[6, 7, 21, 22] in all calculations most of the depicted states are basically valence states with a significant contribution form $\pi \rightarrow \pi^*$, and because CAM-B3LYP tends to overestimate the excitation energies. [6]

The primary observation in Figure 6-2 is the noteworthy theoretical reproduction of the experimental OPA and ECD spectra (spectral shape, position of the bands, and the fano-type

shape profile) of A6 and CN6 using CAM-B3LYP. The remarkably good performance of this particular XCF is attributed to the existent intramolecular charge transfer (ICT) in both molecules, being ICT unequivocally stronger in CN6. In this particular molecule, the cyano (–C≡N) group, a well-known moderate electron-withdrawing group, located beyond the helicene core on one extreme of the molecule, causes not only a strong ICT effect but it increases the range of the electronic delocalization beyond the helicene core.

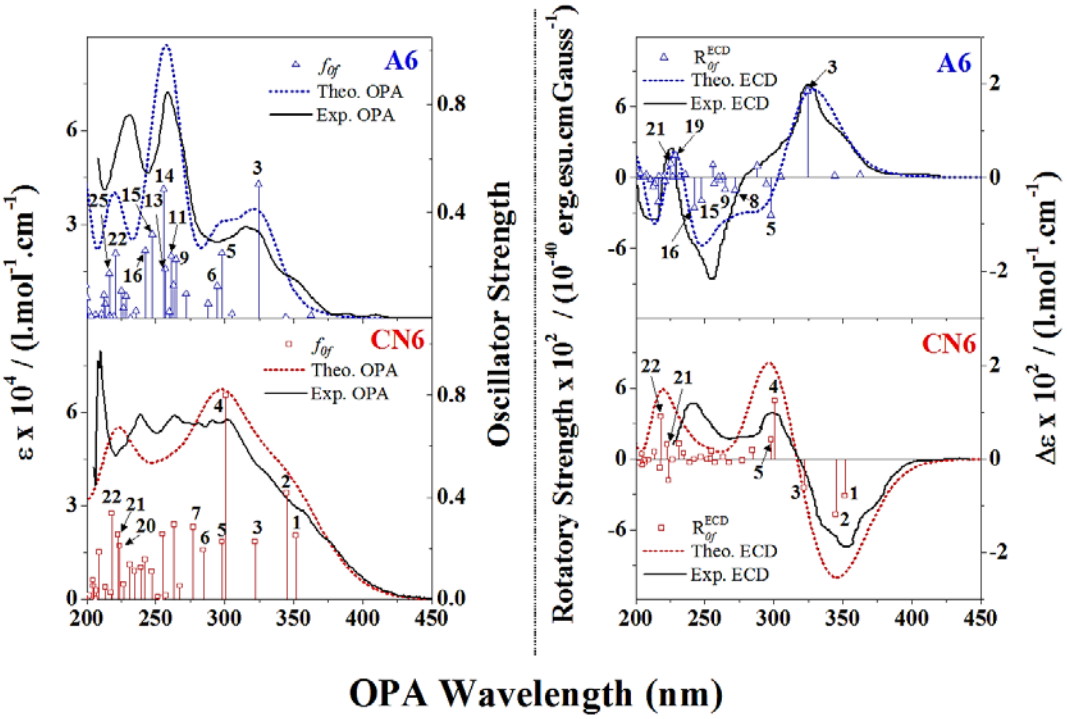

Figure 6-2. Experimental (black solid line) and theoretical (colored dotted lines) UV-*vis* (left column) and ECD (right column) spectra of A6 and CN6. Colored empty symbols display the oscillator strengths for each molecule. OPA for the lowest 60 electronic excited states were computed at the CAM-B3LYP/6-31G(d) level of theory using Gaussian 09 in THF and employing PCM. The theoretical spectra are only shown within the measurable spectral range (200 nm through 450 nm) with spectral shifts: A6 (+20 nm) and CN6 (0 nm). Γ = 0.5 eV (FWHM) was used for all the spectra. Excited states contributing to 20 % or more of the total intensity of prominent spectral features observed in the theory and the experiment are highlighted. All the experimental spectra were taken in THF solutions.

This last point can be confirmed even further by the analysis presented in Figure 6-3, which show the molecular orbitals involved in the transitions to excited state #3 and #2 for A6 and CN6, respectively, i.e. the most important excitations on the red side of the OPA and ECD

theoretical spectra calculated with CAM-B3LYP (see Figure 6-2 and Tables 6-1.a and 6-1.b). The observed ICT in all three excitations involved in the CN6 transition is indeed extremely important. Similar evidences have already been reported by Rizzo and co-workers in other molecular systems [2, 6, 21, 22] and, are in accordance with previous calculations performed in CN6. [15]

Table 6-1. Assignment of theoretical (CAM-B3LYP) excited states (E.S.) to experimental (Exp.) bands. Only E.S. contributing to 20 % or more of the total intensity of the corresponding bands are shown. Tables for A6 and CN6 are labeled **6-1.a** and **6-1.b**, respectively. Each table contains data for the OPA, ECD, TPA and TPCD spectra of the corresponding helicenes. The theoretical OPA wavelengths are shown with the corresponding spectral shift (see figure captions of the corresponding spectra for the exact value of the spectral shifts) (λ^{MAX} = OPA wavelength of the corresponding band for its maximum amplitude, ***E.S*** = Excited State Number, ε = molar absorptivity in $l.mol^{-1}.cm^{-1}$, $\Delta\varepsilon$ = difference in molar absorptivity in $l.mol^{-1}.cm^{-1}$, f = oscillator strength, R^{ECD} = rotatory strength in 10^{-40} erg.esu.cm.Gauss^{-1}, ***TPA*** = two-photon absorption cross-section in GM, ***TPCD*** = two-photon circular dichroism in GM, δ^{TPA} = two-photon probability in GM, R^{TPCD} = two-photon circular dichroism rotatory strength in GM)

6-1.a (A6)	**Exp.**	**CAM-B3LYP**			**Exp.**	**CAM-B3LYP**	
	λ^{MAX} (ε)	λ^{MAX} (ε)	*E.S. (f)*		λ^{MAX} ($\Delta\varepsilon$)	λ^{MAX} ($\Delta\varepsilon$)	*E.S. (R^{ECD})*
OPA Bands	321 (28,310)	310 (32,040)	3 (0.50) 5 (0.25) 6 (0.13)	**ECD (+) Bands**	325 (207)	328 (188)	3 (7.35)
	259 (72,160)	257 (87,390)	9 (0.23) 11 (0.24) 13 (0.19) 14 (0.48) 15 (0.32) 16 (0.26)		225 (70)	227 (52)	19 (1.88) 21 (1.22)
	230 (64,780)	220 (40,160)	22 (0.25) 25 (0.18)	**ECD (-) Bands**	256 (-225)	247 (-144)	8 (-1.07) 9 (-1.03) 15 (-1.95) 16 (-2.60)
	Exp.	**CAM-B3LYP**			**Exp.**	**CAM-B3LYP**	
	λ^{MAX} (*TPA*)	λ^{MAX} (*TPA*)	*E.S. (δ^{TPA})*		λ^{MAX} (*TPCD*)	λ^{MAX} (*TPCD*)	*E.S. (R^{TPCD})*
TPA Bands	280 (6.50)	292 (42.6)	9 (16.16) 12 (9.17) 13 (10.46) 14 (9.13)	**TPCD (+) Bands**	235 (0.76)	237 (0.13)	44 (0.07) 48 (0.03)
	235 (7.13)	234 (93.2)	26 (3.97) 28 (6.04) 29 (5.44) 35 (4.43) 45 (14.03) 55 (10.02)	**TPCD (-) Bands**	295 (-0.41)	293 (-0.43)	9 (-0.18) 12 (-0.12) 13 (-0.11)
	215 (13.4)	-	-		250 (-0.20)	249 (-0.10)	33 (-0.06) 34 (-0.08)

Table 6-1 (continued)

6-1.b (CN6)	Exp.	CAM-B3LYP			Exp.	CAM-B3LYP	
	λ^{MAX} (ε)	λ^{MAX} (ε)	E.S. (*f*)		λ^{MAX} (Δε)	λ^{MAX} (Δε)	E.S. (R^{ECD})
OPA Bands	333 (39,127)	345 (40,810)	1 (0.25) 2 (0.42)	ECD (+) Bands	305 (103)	296 (206)	4 (4.94) 5 (1.65)
	280 (56,205)	297 (67,290)	3 (0.23) 4 (0.80) 5 (0.23) 6 (0.19) 7 (0.28)		246 (130)	220 (148)	21 (1.23) 22 (3.59)
	210 (76,345)	222 (55,016)	20 (0.21) 21 (0.25) 22 (0.33)	ECD (-) Bands	353 (-180)	345 (-254)	1 (-3.13) 2 (-4.73) 3 (-2.47)

	Exp.	CAM-B3LYP			Exp.	CAM-B3LYP	
	λ^{MAX} (TPA)	λ^{MAX} (TPA)	E.S. (δ^{TPA})		λ^{MAX} (TPCD)	λ^{MAX} (TPCD)	E.S. (R^{TPCD})
TPA Bands	306 (14.9)	298 (196.8)	8 (155.34)	TPCD (+) Bands	300 (1.80)	297 (1.35)	8 (1.13)
	280 (20.5)	-	-		265 (0.70)	257 (3.51)	18 (1.80) 20 (1.20) 21 (1.08)
	237 (62.5)	256 (1208.8)	19 (699.0)		230 (1.20)	237 (2.62)	32 (0.55) 33 (0.97)

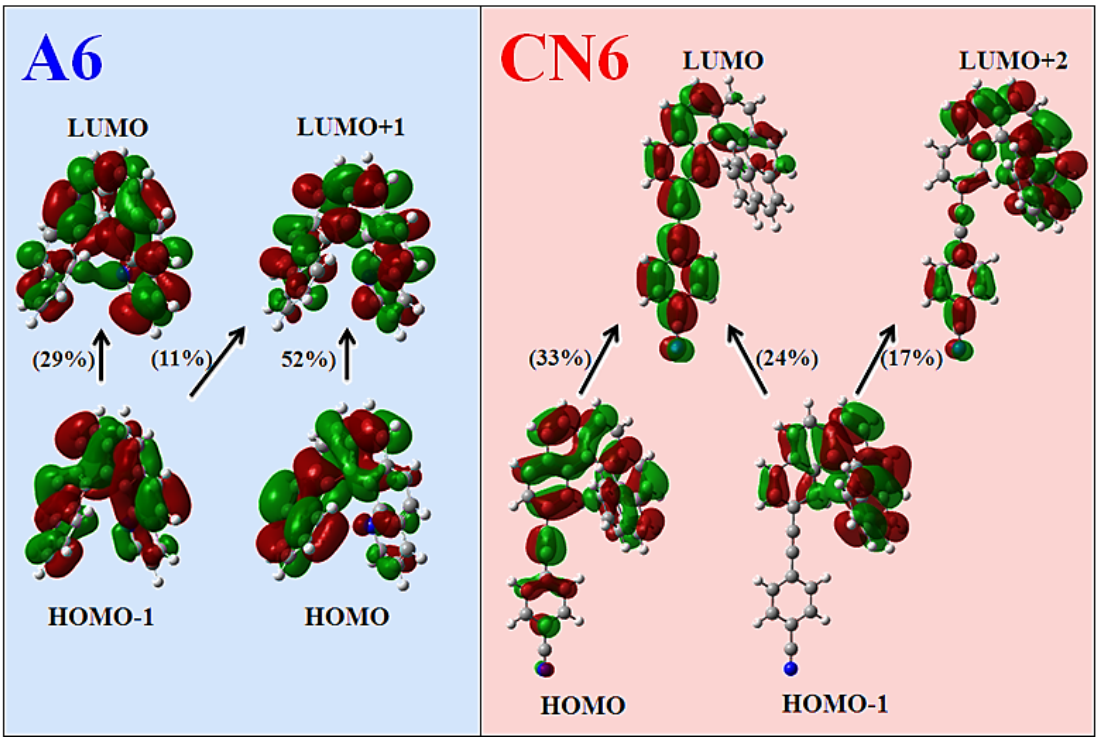

Figure 6-3. Molecular orbitals (MOs) involved in the 3rd and 2nd electronic excited state of A6 and CN6, respectively. The MOs were obtained from CAM-B3LYP/6-31G* TD-DFT calculations in THF using PCM in Gaussian 09. The percent contribution from single excitations ([HOMO – x] → [LUMO + y]) to the excited state is indicated in parenthesis for each case.

Next, one should highlight the fact that the amplitudes of the OPA and ECD signals in both molecules are virtually identical, though there is an obvious difference in ICT between the two. This observation shall be explained more in detail after completing the theoretical-experimental analysis of the nonlinear spectra of A6 and CN6 presented next.

In Figure 6-4 we show the TPA and TPCD spectra (theoretical and experimental), respectively, plotted at half the excitation wavelengths, i.e. in the OPA scale.

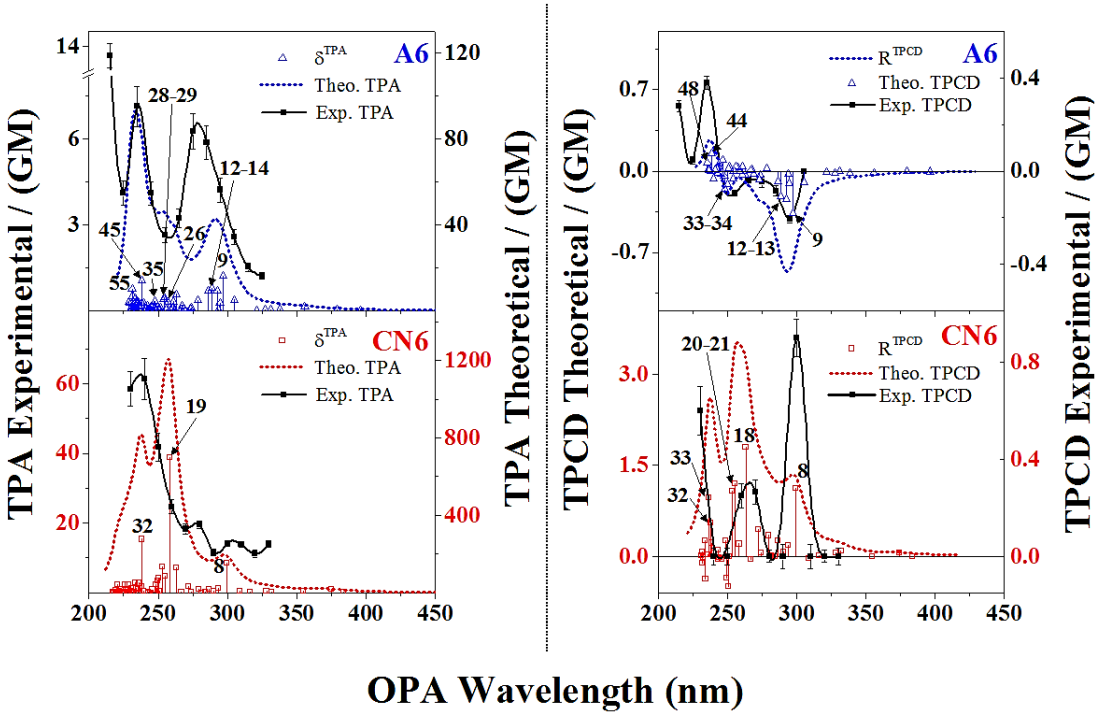

Figure 6-4. Experimental (black scattered squares) and theoretical TPA (left column) and TPCD (right column) spectra of A6 and CN6 calculated *in vacuo* using Dalton 2011. TPA was computed for the first 60 electronic excited states (colored scattered symbols) for both molecules. TPCD was computed for the first 48 and 40 electronic excited states (colored scattered symbols) for A6 and CN6, respectively. The Lorentzian convolution (colored dotted lines) was obtained using a linewidth Γ = 0.15 eV (FWHM). The theoretical spectra were calculated with CAM-B3LYP/ aug-cc-pVDZ for A6, and CAM-B3LYP/ 6-311++G(d,p) for CN6. The theoretical spectral shifts are: A6 (+22 nm) and CN6 (+26 nm). Excited states contributing to 20 % or more of the total intensity of prominent spectral features observed in the theory and the experiment are highlighted. All the experimental spectra were taken in THF solutions.

The spectra of both compounds were taken in THF solution. The theoretical spectra of A6 were obtained with the CAM-B3LYP/aug-cc-pVDZ computed profiles obtained by convoluting the stick spectra (The latter simulates isolated non interacting molecules). To optimize the balance between accuracy and computational cost, calculations in CN6 were performed using the 6-311++G(d,p) basis set, which is a slightly smaller basis set than aug-cc-pVDZ. As for the one-photon spectra a shift has been applied to the computed TPA and TPCD spectra (see figure caption of Figure 6-4). Since the spectroscopic region of relevance is different when comparing one- and two-photon absorption profiles, the shifts applied to the spectra shown in Figure 6-4, chosen to improve the comparison between theory and experiment, are different from those applied to the spectra displayed in Figure 6-2 (assignment of theoretical CAM-B3LYP excited states to experimental bands of A6 and CN6 can be found in Tables 6-1.a and 6-1.b). Also, because strong two-photon absorber states are in most cases weak one-photon absorber, the differences in spectral shift obtained for OPA and TPA are easily explained by considering that OPA and TPA are dominated (see Figure 6-2 and 6-4) by different molecular states. [43, 44]

First, it can be noticed that the theoretical calculations reproduce remarkably the main TPA spectral features of both helicene derivatives. However, the predicted TPA cross-sections are, in most cases, larger than the experimental. It is hard to explain this difference in amplitude considering that all experiments were performed in the femtosecond regime where excited state absorption is negligible. [45, 46] Nevertheless, the chosen XCF reproduces very well the relative intensities between the main TPA bands, and it yields a suitable bandwidth and separation between the peaks.

Second, the intense peak observed at 215 nm in the TPA experimental spectrum of A6, that lead to a strong increasing band in the blue side of the TPA spectrum of this molecule is not well reproduced by the theory. This outcome could be a consequence of the limited number of electronic excited states included in the theoretical calculation of the TPA spectrum or, even more probable, due to the presence of strong TPA resonance enhancement effect found when the measurements are performed in the close vicinity of linear absorption states (see Figure 6-2). [47, 48] In any case, this region would be better analysed with the damped approach to TPA discussed in references 67 and 68.

Next, moving onto TPCD, in Figure 6-4 we display the experimental (in THF solution) and theoretical (isolated molecules) spectra of A6 and CN6, obtained using CAM-B3LYP. One can notice that the theoretical TPCD spectra of A6 and CN6 reproduces notably the shape, sign, and relative intensities of the main three bands in A6 (one positive at 240 nm and two negative at 250 and 290 nm) and the three positive bands in CN6 (280, 300 and 330 nm) - see Tables 1.a and 1.b.

Finally and perhaps the most interesting outcome of the nonlinear characterization of these two molecules is the obviously larger TPA cross-section (approximately ten times) and TPCD signal (ca. two-fold) of CN6 compared to that of A6 (see Figure 6-4). This interesting result can be explained by considering two cooperative effects: a) the strong ICT character of a well-known moderate electron-withdrawing group (–C≡N) on one end of CN6, and b) the extended electron delocalization over the (4-Cyanophenyl)-1-ethynyl substituent outside the helical core in this helicene derivative. In A6, however, a relatively mild ICT is effective only within the hexahelicene core due to the presence of the aza (–N=) group at one end of the molecule. Although, the difference in ICT between A6 and CN6 was discussed earlier in the

linear characterization of these two molecules (see Figure 6-4), the actual implications were not elucidated.

In order to gain more insight about the two effects mentioned above, we performed calculations of OPA, ECD, TPA and TPCD on five CN6-like helicenes (#CN) with different ICT conjugation length outside the [6]carbohelicene core (EXO-ICT), i.e. C6–CN, C6–≡–CN and C6–≡–≡–CN, and within the aromatic cluster (ENDO-ICT), i.e. carbohelicene derivatives with six (C6–CN), seven (C7–CN) and eight (C8–CN) aromatic rings extending the helical arrangement. Molecular structures of #CN were introduced in Figure 6-1.b.

In Figure 6-5 we show the comparative plot of the OPA and ECD, and the TPA and TPCD theoretical spectra of all five #CN.

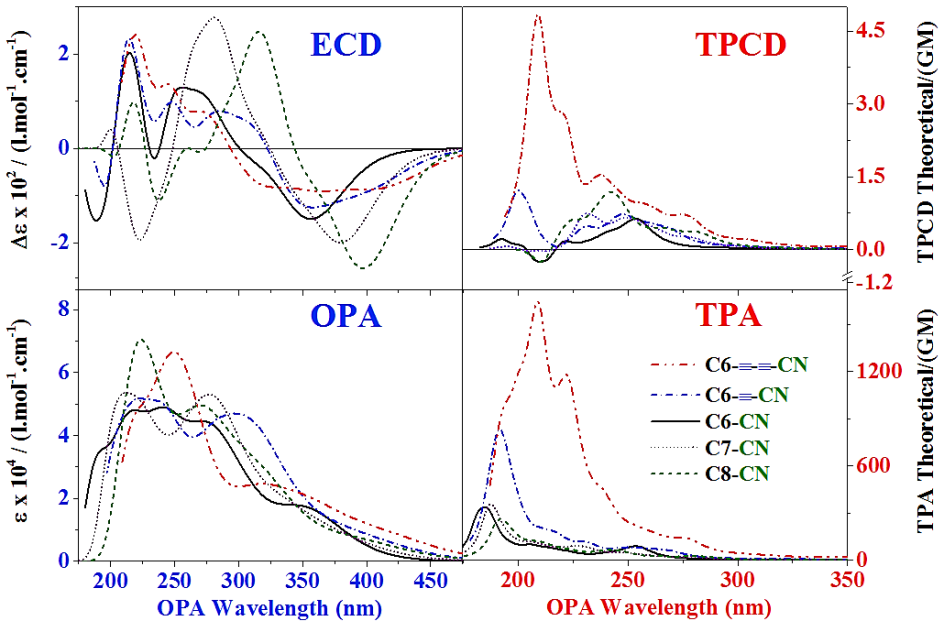

Figure 6-5. OPA, ECD, TPA and TPCD theoretical spectra of all five #CN. OPA and ECD spectra were obtained from the Lorentzian convolution (Γ = 0.5 eV FWHM) of the first 60 excited states excited states of the optimized structures of all five #CN calculated at the CAM-B3LYP/6-31G(d) level of theory in THF using PCM and employing Gaussian 09. TPA spectra of the optimized structures of all five #CN derivatives were obtained from the Lorentzian convolution (Γ = 0.15 eV FWHM) of the first 60 excited states excited states except for C7–CN (67 states) and C8–CN (73 states). TPCD spectra of the optimized structures of all five #CN derivatives were obtained from the Lorentzian convolution (Γ = 0.15 eV FWHM) of the first 40 excited states except for C7–CN (45 states). TPA and TPCD calculations were performed at the CAM-B3LYP/ 6-311++G(d,p) level of theory *in vacuo* using Dalton 2011.

As expected from the linear analysis of A6 and CN6, the OPA and ECD signals are not strongly affected by the nature of ICT, i.e. EXO-ICT *vs.* ENDO-ICT. In this figure one can only observe a small increase in the amplitude of the ECD signal and a consistent red shift of the position of the fano-type bands of #CN as the conjugation length of the aromatic cluster increases from C6 → C8. However, EXO-ICT seems to have no significant effect on the linear spectra of these molecules. This interesting result suggests the generation of stronger molecular circular currents as the spiral length of the ENDO-ICT increase in helical molecules. These currents can in turn generate molecular magnetic fields that couple with the magnetic dipole transition moment of #CN, [5, 50, 51] thus increasing the ECD response as follow: C6–CN < C7–CN < C8–CN.

In the nonlinear optical response instance it is obvious that the effect of EXO-ICT is much stronger than ENDO-ICT. In Figure 6-5, one can notice that while the maximum TPA cross-sections of C6–≡–CN and C6–≡–≡–CN are approximately 2.4 and 4.9 times that of C6–CN, respectively, the difference in TPA between C6–CN, C7–CN and C8–CN is nearly negligible - the small difference noticed between C6–CN, C7–CN and C8–CN, on the blue side of the spectra, is mainly attributed to the limitations of our computational resources to calculate the required number of excited states in the larger molecules (C7–CN and C8–CN) to cover the same spectral region obtained for C6–CN. In TPCD one can also remark a stronger EXO-ICT effect, i.e. the integrated area of the TPCD spectra of C6–≡–CN and C6–≡–≡–CN are approximately 2.5 and 7.9 folds that of C6–CN, respectively. The difference in TPCD between C7–CN and C8–CN, and C6–CN is ca. 1.7 and 2.2, respectively, i.e. less significant than in the previous series of #CN but comparable to the small differences observed in ECD. These results strongly suggest that: (1) the electric dipole transition moment, which directly affect the TPA

response of conjugated molecules, [52, 53] is enhanced by increasing the electronic conjugation length beyond the helicene core, (2) the magnetic dipole transition moment could enhance the TPCD response of helical molecules *via* its coupling with the induced molecular magnetic field resultant from the generation of molecular circular currents within the helical core, [5, 50, 51] and (3) the contribution of the electric quadrupole transition moment to the TPCD signal of helical molecules with strong EXO-ICT - the extended electronic conjugation beyond the helicene core significantly enhances the nonlinear response of this type of molecular structures. While points (2) and (3) are crucial for TPCD in the series of molecules with greater EXO-ICT (C6–CN, C6–≡–CN and C6–≡–≡–CN), in the other series of molecules (C6–CN, and C7–CN and C8–CN) point (2) becomes more critical.

With the intention of supporting even further these results, in Figure 6-6 we present the integrated TPCD spectra, and the sum of the absolute values of molecular parameters B_1+B_3 and B_2 that define the contributions of the magnetic dipole transition moment and the electric quadrupole transition moment, respectively, to the TPCD rotatory strength [54-56] (See Section 5 in the introduction of this dissertation for further detail on molecular parameters B_i). The clear tendencies observed in this plot, *viz.* i) $\Sigma|B_1+B_3|$ (Figure 6-6.b) following the same trend observed in TPCD (Figure 6-6.a) within the whole series of #CN, and ii) $\Sigma|B_2|$ (Figure 6-6.c) matching only the EXO-ICT series (C6–CN, C6–≡–CN and C6–≡–≡–CN) confirm our initial thoughts.

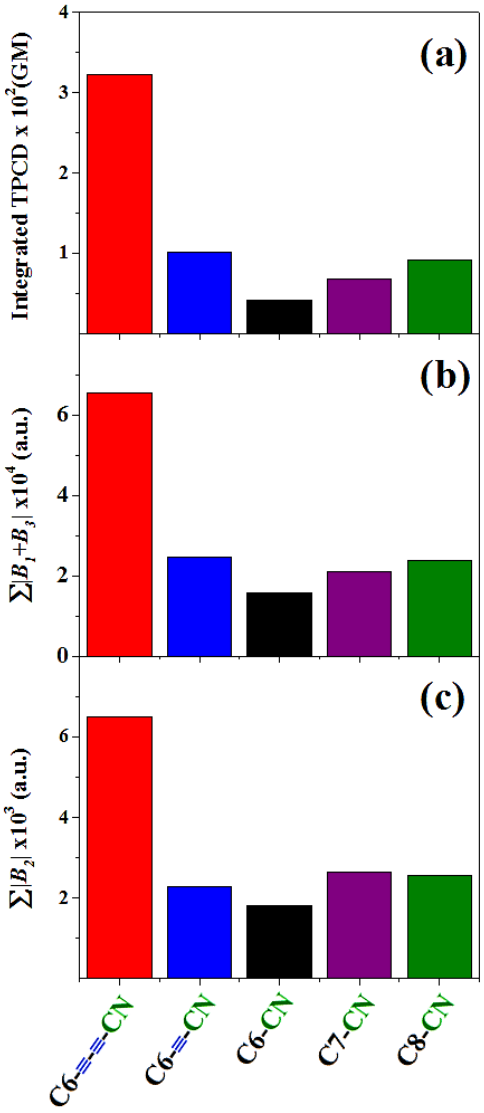

Figure 6-6. Comparative bar graph of **a)** integrated TPCD spectra, **b)** $\Sigma|B_1+B_3|$ and **c)** $\Sigma|B_2|$, for all five #CN.

6.5 Conclusions

In summary, we have demonstrated that the TPA cross-section and the amplitude of the TPCD signal in helicenes are strongly affected not only by the strength of the ICT but by its nature. The molecular orbital analysis of A6 and CN6, and the theoretical analysis of these effects on a series of CN6-like helicenes validated our hypothesis. Through this research we were able to show that while the extension of the electronic delocalization beyond the helicene core (EXO-ICT) enhances the contribution of the electric quadrupole and magnetic transition moments to the TPCD rotatory strength ($R_{0f}^{TPCD}\left(\omega_{0f}\right)$), the electronic delocalization within the arrangement of aromatic rings (ENDO-ICT) primarily increases the contribution of the magnetic dipole transition moment to $R_{0f}^{TPCD}\left(\omega_{0f}\right)$.

6.6 References

1. Vesga, Y.; Diaz, C.; Higgs, M.; Hernandez, F. E., Two-Photon Circular Dichroism of Molecular Structures Simulating L-tryptophan Residues in Proteins with Secondary Structures. *Chem. Phys. Lett.* **2014,** *601* (0), 6-12.

2. Díaz, C.; Echevarria, L.; Rizzo, A.; Hernández, F. E., Two-Photon Circular Dichroism of an Axially Dissymmetric Diphosphine Ligand with Strong Intramolecular Charge Transfer. *J. Phys. Chem. A* **2014,** *118* (5), 940-946.

3. Díaz, C.; Echevarria, L.; Hernández, F. E., Conformational Study of an Axially Chiral Salen Ligand in Solution using Two-Photon Circular Dichroism and the Fragment-Recombination Approach. *J. Phys. Chem. A* **2013,** *117*, 8416–8426.

4. Diaz, C.; Echevarria, L.; Hernández, F. E., Overcoming the Existent Computational Challenges in the Ab Initio Calculations of the Two-Photon Circular Dichroism Spectra of Large Molecules using a Fragment-Recombination Approach. *Chem. Phys. Lett.* **2013,** *568-569*, 176-183.

5. Diaz, C.; Lin, N.; Toro, C.; Passier, R.; Rizzo, A.; Hernández, F. E., The Effect of the π-Electron Delocalization Curvature on the Two-Photon Circular Dichroism of Molecules with Axial Chirality. *J. Phys. Chem. Lett.* **2012,** *3*, 1808-1813.

6. Lin, N.; Santoro, F.; Zhao, X.; Toro, C.; De Boni, L.; Hernández, F. E.; Rizzo, A., Computational Challenges in Simulating and Analyzing Experimental Linear and Nonlinear Circular Dichroism Spectra. R-(+)-1,1'-bis(2-naphthol) as a Prototype Case. *J. Phys. Chem. B* **2011,** *115*, 811-824.

7. Toro, C.; De Boni, L.; Lin, N.; Santoro, F.; Rizzo, A.; Hernandez, F. E., Two-Photon Absorption Circular Dichroism: A New Twist in Nonlinear Spectroscopy. *Chem. Eur. J.* **2010,** *16*, 3504-3509.

8. Wigglesworth, T. J.; Sud, D.; Norsten, T. B.; Lekhi, V. S.; Branda, N. R., Chiral Discrimination in Photochromic Helicenes. *J. Am. Chem. Soc.* **2005,** *127* (20), 7272-7273.

9. Reetz, M. T.; Sostmann, S., 2,15-Dihydroxy-hexahelicene (HELIXOL): Synthesis and use as an Enantioselective Fluorescent Sensor. *Tetrahedron* **2001,** *57* (13), 2515-2520.

10. Field, J. E.; Muller, G.; Riehl, J. P.; Venkataraman, D., Circularly Polarized Luminescence from Bridged Triarylamine Helicenes. *J. Am. Chem. Soc.* **2003,** *125* (39), 11808-11809.

11. Hassey, R.; Swain, E. J.; Hammer, N. I.; Venkataraman, D.; Barnes, M. D., Probing the Chiroptical Response of a Single Molecule. *Science* **2006,** *314* (5804), 1437-1439.

12. Verbiest, T.; Elshocht, S. V.; Kauranen, M.; Hellemans, L.; Snauwaert, J.; Nuckolls, C.; Katz, T. J.; Persoons, A., Strong Enhancement of Nonlinear Optical Properties Through Supramolecular Chirality. *Science* **1998,** *282* (5390), 913-915.

13. Verbiest, T.; Sioncke, S.; Persoons, A.; Vyklicky, L.; Katz, T. J., Electric-Field-Modulated Circular-Difference Effects in Second-Harmonic Generation from a Chiral Liquid Crystal. *Angew. Chem. Int. Ed. Engl.* **2002,** *41* (20), 3882-3884.

14. Míšek, J.; Teplý, F.; Stará, I. G.; Tichý, M.; Šaman, D.; Císařová, I.; Vojtíšek, P.; Starý, I., A Straightforward Route to Helically Chiral N-Heteroaromatic Compounds: Practical Synthesis of Racemic 1,14-Diaza[5]helicene and Optically Pure 1- and 2-Aza[6]helicenes. *Angew. Chem. Int. Ed.* **2008,** *47* (17), 3188-3191.

15. Moussa, M. E. S.; Srebro, M.; Anger, E.; Vanthuyne, N.; Roussel, C.; Lescop, C.; Autschbach, J.; Crassous, J., Chiroptical Properties of Carbo[6]Helicene Derivatives Bearing Extended π-Conjugated Cyano Substituents. *Chirality* **2013,** *25* (8), 455-465.

16. De Boni, L.; Toro, C.; Hernandez, F. E., Synchronized Double L-Scan Technique for the Simultaneous Measurement of Polarization-Dependent Two-Photon Absorption in Chiral Molecules. *Opt. Lett.* **2008,** *33*, 2958-2960.

17. Rizzo, A.; Jansík, B.; Pedersen, T. B.; Agren, H., Origin Invariant Approaches to the Calculation of Two-Photon Circular Dichroism. *J. Chem. Phys.* **2006,** *125*, 64113.

18. Jansík, B.; Rizzo, A.; Agren, H., Ab Initio Study of the Two-Photon Circular Dichroism in Chiral Natural Amino Acids. *J. Phys. Chem. B* **2007,** *111*, 446-460.

19. Jansík, B.; Rizzo, A.; Ågren, H.; Champagne, B., Strong Two-Photon Circular Dichroism in Helicenes: A Theoretical Investigation. *J. Chem. Theory Comput.* **2008,** *4*, 457-467.

20. Rizzo, A.; Lin, N.; Ruud, K., Ab Initio Study of the One- and Two-Photon Circular Dichroism of R-(+)-3-Methyl-Cyclopentanone. *J. Chem. Phys.* **2008,** *128*, 164312.

21. Lin, N.; Santoro, F.; Rizzo, A.; Luo, Y.; Zhao, X.; Barone, V., Theory for Vibrationally Resolved Two-Photon Circular Dichroism Spectra. Application to (R)-(+)-3-Methylcyclopentanone. *J. Phys. Chem. A* **2009,** *113*, 4198-4207.

22. Guillaume, M.; Ruud, K.; Rizzo, A.; Monti, S.; Lin, Z.; Xu, X., Computational Study of the One- and Two-Photon Absorption and Circular Dichroism of (L)-Tryptophan. *J. Phys. Chem. B* **2010,** *114*, 6500-6512.

23. Runge, E.; Gross, E. K. U., Density-Functional Theory for Time-Dependent Systems. *Phys. Rev. Lett.* **1984,** *52*, 997-1000.

24. Becke, A. D., Density-Functional Exchange-Energy Approximation with Correct Asymptotic Behavior. *Phys. Rev. A* **1988,** *38*, 3098-3100.

25. Becke, A. D., Density-Functional Thermochemistry. III. The Role of Exact Exchange. *J. Chem. Phys.* **1993,** *98*, 5648-5652.

26. Lee, C.; Yang, W.; Parr, R. G., Development of the Colle-Salvetti Correlation-Energy Formula into a Functional of the Electron Density. *Phys. Rev. B: Condens. Matter* **1988,** *37*, 785-789.

27. Krishnan, R.; Binkley, J. S.; Seeger, R.; Pople, J. A., Self-Consistent Molecular Orbital Methods. XX. A Basis Set for Correlated Wave Functions. *J. Chem. Phys.* **1980,** *72* (1), 650-654.

28. Clark, T.; Chandrasekhar, J.; Spitznagel, G. W.; Schleyer, P. V. R., Efficient Diffuse Function-Augmented Basis Sets for Anion Calculations. III. The 3-21+G Basis Set for First-Row Elements, Li–F. *J. Comput. Chem.* **1983,** *4* (3), 294-301.

29. Frisch, M. J.; Trucks, G. W.; Schlegel, H. B.; Scuseria, G. E.; Robb, M. A.; Cheeseman, J. R.; Scalmani, G.; Barone, V.; Mennucci, B.; Petersson, G. A., *et al.*, Gaussian 09, Revision A.1. Gaussian, Inc.: Wallingford CT, 2009.

30. Tomasi, J.; Mennucci, B.; Cammi, R., Quantum Mechanical Continuum Solvation Models. *Chem. Rev.* **2005,** *105*, 2999-3093.

31. Yanai, T.; Tew, D. P.; Handy, N. C., A new Hybrid Exchange-Correlation Functional using the Coulomb-Attenuating Method (CAM-B3LYP). *Chem. Phys. Lett.* **2004,** *393*, 51-57.

32. Lin, N.; Santoro, F.; Zhao, X.; Rizzo, A.; Barone, V., Vibronically Resolved Electronic Circular Dichroism Spectra of (R)-(+)-3-Methylcyclopentanone: A Theoretical Study. *J. Phys. Chem. A* **2008,** *112*, 12401-12411.

33. Marques, M. A.; Maitra, N. T.; Nogueira, F. M.; Gross, E. K.; Rubio, A., *Fundamentals of time-dependent density functional theory*. Springer: 2012; Vol. 837.

34. Ullrich, C. A., *Time-dependent density-functional theory: concepts and applications*. Oxford University Press: 2011.

35. Aryanpour, K.; Roberts, A.; Sandhu, A.; Rathore, R.; Shukla, A.; Mazumdar, S., Subgap Two-Photon States in Polycyclic Aromatic Hydrocarbons: Evidence for Strong Electron Correlations. *J. Phys. Chem. C* **2014,** *118* (6), 3331-3339.

36. Hirata, S.; Head-Gordon, M., Time-dependent density functional theory for radicals: An improved description of excited states with substantial double excitation character. *Chem. Phys. Lett.* **1999,** *302* (5), 375-382.

37. Olsen, J.; Jo, P., Linear and nonlinear response functions for an exact state and for an MCSCF state. *J. Chem. Phys.* **1985,** *82* (7), 3235-3264.

38. Aidas, K.; Angeli, C.; Bak, K. L.; Bakken, V.; Bast, R.; Boman, L.; Christiansen, O.; Cimiraglia, R.; Coriani, S.; Dahle, P., *et al.*, The Dalton Quantum Chemistry Program System. *WIREs Comput. Mol. Sci.* **2014,** *4* (3), 269-284.

39. Knippenberg, S.; Rehn, D. R.; Wormit, M.; Starcke, J. H.; Rusakova, I. L.; Trofimov, A. B.; Dreuw, A., Calculations of nonlinear response properties using the intermediate state representation and the algebraic-diagrammatic construction polarization propagator approach: Two-photon absorption spectra. *J. Chem. Phys.* **2012,** *136* (6), 064107.

40. Knippenberg, S.; Starcke, J. H.; Wormit, M.; Dreuw, A., The low-lying excited states of neutral polyacenes and their radical cations: a quantum chemical study employing the algebraic diagrammatic construction scheme of second order. *Mol. Phys.* **2010,** *108* (19-20), 2801-2813.

41. Rassolov, V. A.; Pople, J. A.; Ratner, M. A.; Windus, T. L., 6-31G* Basis Set for Atoms K through Zn. *J. Chem. Phys.* **1998,** *109*, 1223-1229.

42. Kendall, R. A.; Dunning, T. H.; Harrison, R. J., Electron affinities of the first-row atoms revisited. Systematic basis sets and wave functions. *J. Chem. Phys.* **1992,** *96* (9), 6796-6806.

43. Birge, R. R.; Pierce, B. M., A Theoretical Analysis of the Two-Photon Properties of Linear Polyenes and the Visual Chromophores. *J. Chem. Phys.* **1979,** *70* (1), 165-178.

44. Bonin, K. D.; McIlrath, T. J., Two-Photon Electric-Dipole Selection Rules. *J. Opt. Soc. Am. B* **1984,** *1*, 52-55.

45. Wu, F.; Zhang, G.; Tian, W.; Chen, W.; Zhao, G.; Cao, S.; Xie, W., Two-Photon Absorption and Two-Thoton Assisted Excited-State Absorption in $CdSe_{0.3}S_{0.7}$ quantum dots. *J. Opt. A: Pure Appl. Opt.* **2009,** *11* (6), 0652061-0652065.

46. Hernandez, F. E.; Belfield, K. D.; Cohanoschi, I.; Balu, M.; Schafer, K. J., Three- and Four-Photon Absorption of a Multiphoton Absorbing Fluorescent Probe. *Appl. Opt.* **2004,** *43*, 5394-5398.

47. Nascimento, M. A. C., The Polarization Dependence of Two-Photon Absorption Rates for Randomly Oriented Molecules. *Chem. Phys.* **1983,** *74*, 51-66.

48. Alam, M. M.; Chattopadhyaya, M.; Chakrabarti, S.; Rizzo, A., On the Origin of the Very Strong Two-Photon Activity of Squaraine Dyes - A Standard/Damped Response Theory Study. *Phys. Chem. Chem. Phys.* **2014,** *16* (17), 8030-8035.

49. Kristensen, K.; Kauczor, J.; Thorvaldsen, A. J.; Jørgensen, P.; Kjærgaard, T.; Rizzo, A., Damped Response Theory Description of Two-Photon Absorption. *J. Chem. Phys.* **2011,** *134* (21), 214104.

50. Nobusada, K.; Yabana, K., Photoinduced Eelectric Currents in Ring-Shaped Molecules by Circularly Polarized Laser Pulses. *Phys. Rev. A* **2007,** *75* (3), 032518.

51. Skourtis, S.; Beratan, D.; Naaman, R.; Nitzan, A.; Waldeck, D., Chiral Control of Electron Transmission through Molecules. *Phys. Rev. Lett.* **2008,** *101* (23), 238103.

52. Marder, S. R.; Gorman, C. B.; Meyers, F.; Perry, J. W.; Bourhill, G.; Brédas, J. L.; Pierce, B. M., A unified description of linear and nonlinear polarization in organic polymethine dyes. *Science* **1994,** *265*, 632-635.

53. Albota, M. B., D.; Bredas, J. L.; Ehrlich, J. E.; Fu, J. Y.; Heikal, A. A.; Hess, S. E.; Kogej, T.; Levin, M. D.; Marder, S. R.; McCord-Maughon, D.; Perry, J. W.; Rockel, H.; Rumi, M.; Subramaniam, C.; Webb, W. W.; Wu, X. L.; Xu, C., Design of Organic Molecules with Large Two-Photon Absorption Cross Sections. *Science* **1998,** *281*, 1653-1656.

54. Tinoco, I., Two-Photon Circular Dichroism. *J. Chem. Phys.* **1975,** *62*, 1006-1009.

55. Jansik, B.; Rizzo, A.; Agren, H., Response Theory Calculations of Two-Photon Circular Dichroism. *Chem. Phys. Lett.* **2005,** *414*, 461-467.

56. Hernández, F. E.; Rizzo, A., Two-Photon Polarization Dependent Spectroscopy in Chirality: a Novel Experimental-Theoretical Approach to Study Optically Active Systems. *Molecules (Basel, Switzerland)* **2011,** *16*, 3315-3337.

CHAPTER 7 : FUTURE WORK

The research presented in this dissertation constitutes the first comprehensive and systematic theoretical-experimental study of the structure-property relationship of TPCD. The focus of the research presented in this manuscript was primarily on: i) the study of the effect of the "twist" in the π-electron delocalization of chiral biaryl derivatives on TPCD, ii) the development of a fragment recombination approach for the calculation of the TPCD spectra of large molecules and the demonstration of its direct application for the conformational analysis of a complex axially chiral Salen ligand, and iii) the study of the effect of the strength and nature of intramolecular charge transfer onto the TPCD of compounds with axial and helical chirality.

Although we have already made great progress in the understanding of the structure-property relationship of TPCD, much more need to be explored before truly realizing its full potential and unique applications. With this in mind we propose to continue the study of the structure-property relationship of TPCD by embarking on the following investigations:

1) Complete the study of the effect of ICT on the TPCD signal on chiral systems with different molecular configurations of donor (*D*) and acceptor (*A*) groups around the molecular core (*C*), e.g. *D-C-D, D-C-A, and A-C-A, & D-π-C-π-D, D-π-C-π-A, and A-π-C-π-A.*
2) Extend the application of TPCD to the Far UV (FUV, 122 nm – 200nm) and perform conformational analysis of chiral biomolecules in a spectral region never attempted before.
3) Start conformational studies, using TPCD, on relatively small peptides known to participate in specific diseases by modeling aminoacid residues present in the chain.

APPENDIX A :
PUBLICATIONS FROM DISSERTATION WORK

1. Passier, R.; Ritchie, J. P.; Toro, C.; Diaz, C.; Masunov, A. E.; Belfield, K. D.; Hernandez, F. E., "Thermally controlled preferential molecular aggregation state in a thiacarbocyanine dye", J. Chem. Phys. **2010**, *133*, 134508-1−134508-7.
2. Toro, C.; Passier, R.; Diaz, C.; Tuuttila, T.; Rissanen, K.; Huuskonen, J.; Hernandez, F. E., "Unveiling electronic transitions in three novel chiral azo-compounds using linear and nonlinear circular dichroism: A theoretical-experimental study", J. Phys. Chem. A **2011**, *115*, 1186−1193.
3. Diaz, C.; Frazer, A.; Morales, A.; Belfield, K. D.; Ray, S.; Hernández, F. E., "Structural identification of a novel axially-chiral binaphthyl fluorene based Salen ligand in solution using ECD: A Theoretical-experimental analysis". J. Phys. Chem. A **2012**, *166*, 2453−2465.
4. Diaz, C.; Lin, N.; Toro, C.; Passier, R.; Rizzo, A.; Hernández, F. E., "The effect of the π-electron delocalization curvature on the two-photon circular dichroism of molecules with axial chirality", J. Phys. Chem. Lett. **2012**, *3*, 1808−1813.
5. Vivas, M. G.; Diaz, C.; Echevarria, L.; Mendonca, C. R.; Hernández, F. E.; De Boni, L., "Two-Photon Circular-Linear Dichroism of Perylene in Solution: A Theoretical-Experimental Study", J. Phys. Chem. B **2013**, *117*, 2742−2747.
6. Diaz, C.; Echevarria, L.; Hernández, F. E., "Overcoming the existent computational challenges in the ab-initio calculations of the two-photon circular dichroism spectra of large molecules using a fragment-recombination approach", Chem. Phys. Lett. **2013**, *568-569*, 176−183.
7. Tiburcio-Moreno, J. A.; Echevarria, L.; Diaz, C.; Alvarado Gil, J. J.; Hernandez, F. E., "Polarization dependent two-photon absorption spectroscopy on a naturally occurring biomarker (Curcumin) in solution: A Theoretical-experimental study", Chem. Phys. Lett. **2013**, *583*, 160−164.
8. Diaz, C.; Echevarria, L.; Hernández, F. E., "Conformational study of an axially-chiral Salen ligand in solution using two-photon circular dichroism and the fragment-recombination approach", J. Phys. Chem A. **2013**, *117*, 8416−8426.
9. Diaz, C.; Echevarria, L.; Rizzo, A.; Hernández, F. E., "Two-photon circular dichroism of an axially dissymmetric disphosphine ligand with strong intramolecular charge transfer", J. Phys. Chem. A **2014**, *118*, 940−946.
10. Vesga, Y.; Diaz, C.; Higgs, M.; Hernandez, F. E., "Two-photon circular dichroism of molecular structures simulating L-tryptophan residues in proteins with secondary structures", Chem. Phys. Lett. **2014**, *601*, 6−12.
11. Dezhahang, Z.; Poopari, M. R.; Hernández, F. E.; Diaz, C.; Xu, Y., "Diastereomeric Preference of a Triply Axial Chiral Binaphthyl Based Molecule: a Concentration Dependent Study by Chiroptical Spectroscopies", PCCP **2014**, *16*, 12959−12567.
12. Vesga, Y.; Diaz, C.; Hernandez, F. E., "Two-photon circular dichroism of molecular structures simulating L-Try, L-Phe and L-His residues in proteins with secondary structures", RSC Adv. **2014**, *4*, 60974–60986.
13. Diaz, C.; Llovera, L.; Echevarria, L.; Hernández, F. E., "Theoretical-Experimental Approach for the Tautomeric Population Assessment of Benzimidazole Derivatives in Solution via UV-vis Spectroscopy", J. Comput. Aided Mol. Des. **2015**, *29*, 143–154.
14. Diaz, C.; Vesga, Y.; Echevarria, L.; Stará, I. G.; Starỳ, I.; Anger, E.; Shen, C.; Moussa, M. E. S.; Vanthuyne, N.; Crassous, J.; Rizzo, A.; Hernández, F. E., "Two-photon absorption and two-photon circular dichroism of hexahelicene derivatives: a study of the effect of the nature of intramolecular charge transfer", RSC Adv. **2015**, *5*, 17429−17437.
15. Padula, D.; Lahoz, I. R.; Diaz, C.; Hernandez, F. E.; Di Bari, L.; Rizzo, A.; Santoro, F.; Cid M., "A combined experimental-computational investigation to uncover the puzzling behavior of chiral pydocyclophanes: chiroptical respose and one- and two-photon absorption", Chemistry: A European Journal, *Submitted.*
16. Donnelly, J.; Diaz, C.; Hernandez, F. E., "OCTET & BIOTEC: A Model of a Summer Intensive Designed to Cultivate the Future Generation of Young Leaders in STEM", J. Chem. Ed., *Submitted.*

APPENDIX B :

CONTRIBUTION TO CONFERENCES AND RESEARCH FORUMS FROM DISSERTATION WORK

1. Carlos Díaz, Alma Morales, Andrew Frazer, Kevin Belfield, Suren Tatulian, Supriyo Rey, Florencio E. Hernández (March 2011), *Experimental-theoretical characterization of a new optically active binaphthyl fluorene based Salen ligand*, 241st ACS National Meeting & Exposition. Anaheim, California. Oral Presentation
2. Carlos Díaz, Alma Morales, Andrew Frazer, Kevin Belfield, Supriyo Rey, Florencio E. Hernández (December 2011), *Structural identification of a novel axially-chiral binaphthyl fluorene based Salen ligand in solution using electronic circular dichroism: A Theoretical-experimental analysis,* UCF 2011 Biophysics Forum. Invited Oral Presentation.
3. Carlos Díaz, Na Lin, Leonardo De Boni, Remy Passier, Fabrizio Santoro, Antonio Rizzo, Florencio E. Hernández (April 2012), *Study of the effect of the π-electron delocalization curvature on the TPCD of molecules with axial chirality*, 9th UCF Graduate Research Forum. Orlando, Florida. Poster Session.
4. Carlos Díaz, Na Lin, Leonardo De Boni, Remy Passier, Fabrizio Santoro, Antonio Rizzo, Florencio E. Hernández (June 2012), *Study of the effect of the π-electron delocalization curvature on the TPCD of molecules with axial chirality*, 24th International Symposium on Chirality. Fort Worth, Texas. Oral Presentation.
5. Carlos Díaz, Alma Morales, Andrew Frazer, Kevin Belfield, Supriyo Rey, Florencio E. Hernández (March 2012), *Structural identification of a novel axially-chiral binaphthyl fluorene based Salen ligand in solution using electronic circular dichroism: A Theoretical-experimental analysis*, 25 Years of Excellence in Optics and Photonics Symposium at CREOL, The College of Optics and Photonics at UCF. Orlando, Florida. Poster Session.
6. Carlos Díaz, Lorenzo Echevarria, Florencio E. Hernández (March 2014), *Conformational study of an axially-chiral ligand in solution using two-photon circular dichroism and the fragment-recombination approach*, 247th ACS National Meeting & Exposition. Dallas, Texas. Oral Presentation.
7. Yuly Vesga, Carlos Diaz, Mary Higgs, Florencio E. Hernandez (April 2014), *Two-photon circular dichroism of molecular structures simulating L-tryptophan residues in proteins with secondary structures*, 11th UCF Graduate Research Forum. Orlando, Florida. Poster Session.
8. Carlos Díaz, Lorenzo Echevarria, Antonio Rizzo, Florencio E. Hernández (April 2014), *Two-Photon Circular Dichroism of an Axially Dissymmetric Diphosphine Ligand with Strong Intramolecular Charge Transfer*, 11th UCF Graduate Research Forum. Orlando, Florida. Poster Session.
9. Yuly Vesga, Carlos Diaz, Mary Higgs, Florencio E. Hernandez (March 2015), *Theoretical study of two-photon circular dichroism on molecular structures simulating aromatic amino acid residues in proteins with secondary structures*, 249th ACS National Meeting & Exposition. Denver, Colorado. Poster Session.

APPENDIX C :
GAUSSIAN BEAMS

GAUSSIAN BEAMS

One of the approximations that is made when third order nonlinearities are determined from Z-scan curves is that the excitation beam has a Gaussian spatial profile.[1] In this appendix a brief description of the main characteristics that describe these types of beams is presented. [2,3]

The transverse profile of a Gaussian beam (see Figure below) is described by,

$$I = I_0 e^{-2r^2/w^2},$$

where I_0 is the intensity at the propagation axis (maximum intensity), r is the distance measured from the propagation axis and w is the beam waist, that is defined as the value r for which the intensity drops to I_0 / e^2.

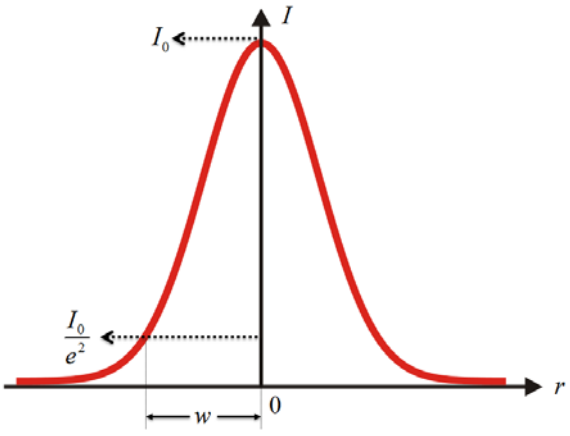

When the Gaussian beam is focused (see Figure below), the parameter w varies along the propagation axis according to:

$$w(z) = w_0 \left[1 + \left(\frac{\lambda z}{\pi w_0^2} \right)^2 \right]^{1/2},$$

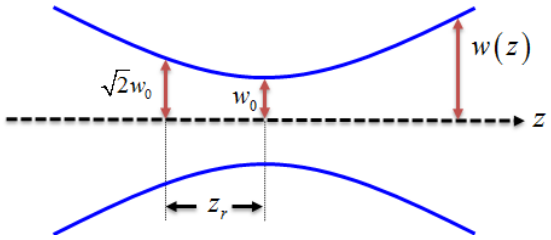

here, w_0 is the beam waist measured at the focal point (z = 0), λ is the wavelength of the light, and z is the position along the propagation axis. An important parameter that characterizes the focused Gaussian beam is the Rayleigh range (z_r) that is defined as the distance from the beam waist to the position where the cross-sectional area of the beam is doubled. This condition occurs when the beam waist is equal to $\sqrt{2}w_0$. The expression for the calculation of the Rayleigh range is,

$$z_R = \frac{\pi w_0^2}{\lambda}.$$

Finally, an important parameter that is used to describe the focused Gaussian beam is its radius of curvature as it propagates, which is given by,

$$R(z) = z\left[1+\left(\frac{z_R}{z}\right)^2\right].$$

References

1. Sheik-Bahae, M.; Said, A. A.; Wei, T. H.; Hagan, D. J.; Van Stryland, E. W., Sensitive measurement of optical nonlinearities using a single beam. *IEEE J. Quantum Electron.* **1990,** *26*, 760-769.
2. Hecht, E. *Optics*, Pearson Education, Inc., San Francisco, 2002.
3. Born, M.; Wolf, E. *Principles of Optics*, Cambridge University Press, Cambridge, 1999.

APPENDIX D :
DENSITY FUNCTIONAL THEORY

DENSITY FUNCTIONAL THEORY

One of the main issues for treating large molecular systems with Hartree-Fock (HF) and post HF methods is that these approaches deal with a large number of variables that result in a tremendous computational problem. This is due to the fact that these methods are based on complicated many-electron wavefunctions that are dependent on each of the three spatial coordinates of all the *n* electrons that comprise the system. In order to simplify this problem, in 1964 Hohenberg and Kohn [1] proposed that all the information from the system could be obtained from the ground state electron density that only depends on three spatial coordinates. They provided proof of two theorems that supported their approach:

> ***Theorem I:*** The ground state density $\rho_0(r)$ of any system of electrons is uniquely determined by the external potential $V_{ext}(r)$ and a constant.

Which means that once the electron density of the system is known, the external potential, and in consequence the Hamiltonian can be directly determined. Then from the Hamiltonian the wavefunction can be determined, thus making every quantum mechanical observable into a functional of the ground state density.

> ***Theorem II:*** There exists a universal functional for the energy E that can be defined in terms of $\rho(r)$. The global minimum value of this functional is equal to the exact ground state density $\rho_0(r)$.

In other words, the exact ground state density minimizes the energy as a functional of the density. These two theorems constitute the basis the so-called Density Functional Theory (DFT).

The Hohenberg-Kohn (HK) Hamiltonian for a many particle system can then be expressed in terms of the external potential as,

$$H = -\frac{1}{2}\sum_i \nabla_i^2 + \sum_i V_{ext}\left(r_i\right) + \frac{1}{2}\sum_{i\neq j}\frac{1}{\left|r_i - r_j\right|}$$

And the associated energy functional is,

$$E_{HK}\left[\rho\right] = T\left[\rho\right] + U\left[\rho\right] + \int d^3 r V_{ext}\left(r\right)\rho\left(r\right)$$

here, $U\left[\rho\right]$ is the potential energy of the interaction of the system and $T\left[\rho\right]$ is the kinetic energy of the system. Unfortunately, expressions for the calculation of the latter two quantities are unknown for the case of a system with interacting electrons, such as the one considered in the HK theory.

In 1965, Khon and Sham [2] proposed an elegant solution to this new problem. Instead of considering a system of interacting electrons their approach was to create a fictitious system composed by non-interacting electrons whose density would be identical to that of the system of interacting electrons. Using this approach the Khon-Sham (KS) equation was proposed,

$$\left(-\frac{1}{2}\nabla^2 + v_{ext}\left(r\right) + v_H\left(r\right) + v_{xc}\left(r\right)\right)\phi_i = \varepsilon_i\phi_i$$

here, $v_{ext}(r)$, $v_H(r)$ and $v_{xc}(r)$ are the external, the Hartree and the exchange correlation (XC) potentials, respectively. $v_{xc}(r)$ is a functional of the electron density that is known as the XC Functional (XCF).

In order to solve time-dependent problems, in 1984 Runge and Gross [3] proposed a time dependent analogue of the first HK theorem that set the basis for what is known today as Time Dependent DFT (TD-DFT). Using this formalism, the Time-Dependent (TD) KS equation can be expressed as,

$$\left(-\frac{1}{2}\nabla^2 + v_{ext}(r,t) + v_H(r,t) + v_{xc}(r,t)\right)\phi_i(r,t) = i\frac{\partial\phi_j(r,t)}{\partial t}$$

where $v_{ext}(r,t)$, $v_H(r,t)$ and $v_{xc}(r,t)$ are the TD external, the TD Hartree and the TD exchange correlation potentials. For the case of ground state DFT, the variation minimum principle is used for finding the total energy while in TD-DFT a stationary point of the action integral A needs to be found,

$$A = \int_{t_0}^{t_1} dt \left\langle \Psi(t) \left| i\frac{\partial}{\partial t} - H(t) \right| \Psi(t) \right\rangle$$

Exchange Correlation Functionals

The main disadvantage of the KS theory is that an exact XCF is only known for the free electron gas. Therefore, approximations need to be made for all the rest of the molecular systems. The first of these approximations to arise was the Local Density Approximation (LDA), which states that the system can be described by an electron gas whose density is equal to the local density of the molecular system. LDA performs well in systems with slow varying electron densities, like

metals. On the other hand, the rapid changes in electron density observed in molecules make this approximation fail. However, in this case the performance of LDA can be greatly improved through the use Generalized Gradient Approximations (GGA), that contemplate not only the electron density but also its gradient. In addition to these two approximations, in the 1990s Becke [4, 5] proposed to incorporate HF exchange into the XCF, and developed the first series of hybrid functionals. After Becke's initial work, many different hybrid functionals have been developed in order to satisfy the needs of different molecular systems. Throughout this dissertation only two hybrid functionals were used. First, the popular Becke three-parameter Lee Yang Parr (B3LYP) [4-6] and then its Coulomb Attenuated variant know as CAM-B3LYP. [7, 8] B3LYP has the following form,

$$E_{xc}^{B3LYP} = E_x^{LDA} + E_c^{LDA} + a_0\left(E_x^{HF} - E_x^{LDA}\right) + a_x\left(E_x^{GGA} - E_x^{LDA}\right) + a_c\left(E_c^{GGA} - E_c^{LDA}\right)$$

where the parameters a_0 = 0.2, a_x = 0.72 and a_c = 0.81, were obtained from fitting to experimental data. CAM-B3LYP modifies B3LYP in such a way that it accounts for long-range exchange, this modification is needed for molecules exhibiting Rydberg or charge transfer states, were the electrons usually have the ability to travel far away from the nuclei. In the CAM-B3LYP [7] functional the short- and long-range exchange are adjusted through the use of the parameters, using the following equation,

$$\frac{1}{r_{12}} = \frac{1-\left[\alpha + \beta \cdot \mathrm{erf}\left(\mu r_{12}\right)\right]}{r_{12}} + \frac{\alpha + \beta \cdot \mathrm{erf}\left(\mu r_{12}\right)}{r_{12}}$$

In this dissertation work the standard parametrization (α = 0.19, β = 0.46, μ = 0.33) has been employed.

References

1. Hohenberg, P.; Kohn, W., Inhomogeneous electron gas. *Physical review* **1964,** *136* (3B), B864.

2. Kohn, W.; Sham, L. J., Self-consistent equations including exchange and correlation effects. *Physical Review* **1965,** *140* (4A), A1133.

3. Runge, E.; Gross, E. K. U., Density-Functional Theory for Time-Dependent Systems. *Phys. Rev. Lett.* **1984,** *52* (12), 997-1000.

4. Becke, A. D., Density-Functional Exchange-Energy Approximation with Correct Asymptotic Behavior. *Phys. Rev. A* **1988,** *38*, 3098-3100.

5. Becke, A. D., Density-Functional Thermochemistry. III. The Role of Exact Exchange. *J. Chem. Phys.* **1993,** *98*, 5648-5652.

6. Lee, C.; Yang, W.; Parr, R. G., Development of the Colle-Salvetti Correlation-Energy Formula into a Functional of the Electron Density. *Phys. Rev. B: Condens. Matter* **1988,** *37*, 785-789.

7. Yanai, T.; Tew, D. P.; Handy, N. C., A new Hybrid Exchange-Correlation Functional using the Coulomb-Attenuating Method (CAM-B3LYP). *Chem. Phys. Lett.* **2004,** *393*, 51-57.

8. Peach, M. J. G.; Helgaker, T.; Sałek, P.; Keal, T. W.; Lutnaes, O. B.; Tozer, D. J.; Handy, N. C., Assessment of a Coulomb-attenuated exchange-correlation energy functional. *Phys. Chem. Chem. Phys.* **2006,** *8*, 558-562.

APPENDIX E :

DETAILED CONTRIBUTIONS OF SINGLE EXCITATIONS TO ELECTRONIC EXCITED STATES OF S-BINAP (CHAPTER 4)

Comparative analysis of the most important excitations contributing to the first 40 electronic excited states of S-BINAP in THF. Calculation were performed with TD-DFT at the B3LYP/6-31G*/PCM and CAM-B3LYP/6-31G*/PCM levels of theory. Excitations are expressed as HOMO-X ➡LUMO+Y transitions. (# = excited state number, λ = excitation wavelength, f_{0f} = oscillator strength, Symm. = excited state symmetry, Cont. = percent of contribution to the excited state)

	B3LYP/6-31G*						CAM-B3LYP/6-31G*					
#	λ (nm)	f_{0f}	Symm.	Excitation		Cont. (%)	λ (nm)	f_{0f}	Symm.	Excitation		Cont. (%)
1	341.3	0.0107	A	HOMO	➡ LUMO	93	285.4	0.0182	A	HOMO	➡ LUMO	77
2	336.5	0.0819	B	HOMO	➡ LUMO+1	90	284.8	0.3238	B	HOMO	➡ LUMO+1	66
										HOMO-1	➡ LUMO	14
3	319.6	0.0557	B	HOMO-1	➡ LUMO	79	279.2	0.0265	B	HOMO-1	➡ LUMO	24
				HOMO-2	➡ LUMO	13				HOMO-4	➡ LUMO	10
										HOMO-3	➡ LUMO+1	12
										HOMO-1	➡ LUMO+2	13
4	313.6	0.0357	A	HOMO-2	➡ LUMO+1	11	277.8	0.0095	A	HOMO-4	➡ LUMO+1	12
				HOMO-1	➡ LUMO+1	73				HOMO-3	➡ LUMO	15
				HOMO	➡ LUMO+2	10				HOMO	➡ LUMO+2	19
5	307.2	0.1553	B	HOMO-2	➡ LUMO	80	262.8	0.0323	A	HOMO-1	➡ LUMO+1	61
				HOMO-1	➡ LUMO	11				HOMO	➡ LUMO+2	14
6	305.2	0.0370	A	HOMO	➡ LUMO+2	73	261.9	0.1130	B	HOMO-1	➡ LUMO	45
										HOMO	➡ LUMO+1	10
7	301.5	0.0111	A	HOMO-3	➡ LUMO	24	256.8	0.1414	B	HOMO-2	➡ LUMO	58
				HOMO-2	➡ LUMO+1	58				HOMO	➡ LUMO+1	10
				HOMO-1	➡ LUMO+1	12						
8	292.8	0.0076	B	HOMO-3	➡ LUMO+1	48	250.0	0.2427	A	HOMO-2	➡ LUMO+1	59
				HOMO-2	➡ LUMO+2	20				HOMO	➡ LUMO+2	17

	B3LYP/6-31G*					CAM-B3LYP/6-31G*				
#	λ (nm)	f_{0f}	Symm.	Excitation	Cont. (%)	λ (nm)	f_{0f}	Symm.	Excitation	Cont. (%)
9	286.9	0.0001	A	HOMO-3 ➡ LUMO	57	245.9	0.3140	A	HOMO-2 ➡ LUMO+3	21
				HOMO-2 ➡ LUMO+1	20				HOMO ➡ LUMO+4	26
				HOMO ➡ LUMO+2	10					
10	286.3	0.0393	B	HOMO-1 ➡ LUMO+2	38	245.8	0.0663	B	HOMO-2 ➡ LUMO	10
				HOMO ➡ LUMO+3	51				HOMO-2 ➡ LUMO+4	20
									HOMO ➡ LUMO+3	32
11	280.6	0.0409	B	HOMO-3 ➡ LUMO+1	13	237.7	0.0992	A	HOMO-3 ➡ LUMO	10
				HOMO-1 ➡ LUMO+2	45				HOMO-2 ➡ LUMO+1	13
				HOMO ➡ LUMO+3	28				HOMO ➡ LUMO+4	11
12	280.1	0.2307	A	HOMO-1 ➡ LUMO+3	10	235.6	0.0097	B	HOMO-1 ➡ LUMO+2	11
				HOMO ➡ LUMO+4	79					
13	278.9	0.0949	B	HOMO-3 ➡ LUMO+1	33	232.7	0.0524	A	HOMO-3 ➡ LUMO	26
				HOMO-2 ➡ LUMO+2	20					
				HOMO ➡ LUMO+5	15					
14	272.5	0.0014	B	HOMO-2 ➡ LUMO+2	38	232.3	0.3303	B	HOMO-3 ➡ LUMO+1	50
				HOMO ➡ LUMO+5	57				HOMO-2 ➡ LUMO+2	10
									HOMO-1 ➡ LUMO	11
15	269.8	0.0088	A	HOMO-4 ➡ LUMO+1	24	229.2	0.0049	A	HOMO-11 ➡ LUMO+3	12
				HOMO-3 ➡ LUMO+2	18				HOMO-10 ➡ LUMO+4	10
				HOMO-1 ➡ LUMO+5	13					
16	264.7	0.0679	A	HOMO-1 ➡ LUMO+3	72	229.2	0.0194	B	HOMO-11 ➡ LUMO+4	10
				HOMO ➡ LUMO+4	12				HOMO-10 ➡ LUMO+3	13
17	262.6	0.0108	B	HOMO-1 ➡ LUMO+4	72	226.8	0.0590	B	HOMO-1 ➡ LUMO+2	30
18	260.1	0.0289	B	HOMO ➡ LUMO+7	57	226.6	0.1216	A	HOMO-4 ➡ LUMO+1	13
									HOMO-3 ➡ LUMO	19
									HOMO ➡ LUMO+2	13
19	259.6	0.0097	A	HOMO-2 ➡ LUMO+5	11	220.0	0.8349	B	HOMO-4 ➡ LUMO	43
				HOMO ➡ LUMO+6	59				HOMO-1 ➡ LUMO+2	12

	B3LYP/6-31G*					CAM-B3LYP/6-31G*				
#	λ (nm)	f_{0f}	Symm.	Excitation	Cont. (%)	λ (nm)	f_{0f}	Symm.	Excitation	Cont. (%)
20	258.7	0.0016	A	HOMO-3 ➡ LUMO+2	27	217.9	0.0130	B	HOMO-2 ➡ LUMO+2	28
				HOMO-2 ➡ LUMO+3	52				HOMO ➡ LUMO+5	41
				HOMO-1 ➡ LUMO+3	10				HOMO ➡ LUMO+6	12
21	256.4	0.1057	B	HOMO-4 ➡ LUMO	39	216.5	0.5145	A	HOMO-4 ➡ LUMO+1	11
				HOMO-2 ➡ LUMO+4	12				HOMO-3 ➡ LUMO+2	34
				HOMO ➡ LUMO+8	13					
22	255.5	0.0049	A	HOMO-3 ➡ LUMO+2	36	213.8	0.2714	A	HOMO-1 ➡ LUMO+5	11
				HOMO-2 ➡ LUMO+3	32				HOMO-1 ➡ LUMO+6	10
				HOMO-1 ➡ LUMO+5	14				HOMO ➡ LUMO+9	23
23	254.4	0.0002	A	HOMO-5 ➡ LUMO	32	213.1	0.2015	B	HOMO-2 ➡ LUMO+2	17
				HOMO-4 ➡ LUMO+1	28				HOMO-2 ➡ LUMO+9	15
				HOMO-1 ➡ LUMO+5	15				HOMO ➡ LUMO+6	15
									HOMO ➡ LUMO+8	15
24	254.3	0.0091	B	HOMO-2 ➡ LUMO+4	69	208.4	0.0619	A	HOMO-5 ➡ LUMO	13
				HOMO ➡ LUMO+8	10				HOMO-3 ➡ LUMO+2	12
									HOMO-2 ➡ LUMO+5	13
25	254.1	0.0008	A	HOMO-5 ➡ LUMO	10	207.8	0.0386	A	HOMO-4 ➡ LUMO+1	15
				HOMO-2 ➡ LUMO+5	23				HOMO-1 ➡ LUMO+3	21
				HOMO-1 ➡ LUMO+5	33				HOMO ➡ LUMO+4	25
				HOMO ➡ LUMO+6	10					
26	253.6	0.0457	B	HOMO-5 ➡ LUMO+1	10	207.7	0.0268	B	HOMO-1 ➡ LUMO+4	20
				HOMO-4 ➡ LUMO	10				HOMO ➡ LUMO+3	29
				HOMO ➡ LUMO+8	58					
27	252.4	0.0794	A	HOMO ➡ LUMO+9	78	205.8	0.0210	A	HOMO-5 ➡ LUMO	17
									HOMO-4 ➡ LUMO+1	26
									HOMO-1 ➡ LUMO+3	19

	B3LYP/6-31G*						CAM-B3LYP/6-31G*					
#	λ (nm)	f_{0f}	Symm.	Excitation		Cont. (%)	λ (nm)	f_{0f}	Symm.	Excitation		Cont. (%)
28	250.4	0.0289	A	HOMO-5	➡ LUMO	11	205.6	0.1809	B	HOMO-6	➡ LUMO	10
				HOMO	➡ LUMO+10	44				HOMO-5	➡ LUMO+1	21
										HOMO-4	➡ LUMO	14
29	250.2	0.0124	B	HOMO-6	➡ LUMO	44	204.4	0.0028	A	HOMO	➡ LUMO+7	17
				HOMO-5	➡ LUMO+1	15						
				HOMO	➡ LUMO+11	18						
30	248.9	0.0010	B	HOMO-7	➡ LUMO	37	204.3	0.0347	B	HOMO-1	➡ LUMO+4	13
				HOMO-6	➡ LUMO	26				HOMO	➡ LUMO+8	20
				HOMO-5	➡ LUMO+1	14						
31	247.3	0.0049	A	HOMO-9	➡ LUMO	13	203.1	0.0017	B	HOMO-9	➡ LUMO+1	10
				HOMO-8	➡ LUMO	12				HOMO-5	➡ LUMO+1	21
				HOMO-5	➡ LUMO	29						
				HOMO	➡ LUMO+10	26						
32	247.1	0.0111	A	HOMO-10	➡ LUMO	20	202.3	0.0113	A	HOMO-2	➡ LUMO+5	26
				HOMO-9	➡ LUMO	11				HOMO-1	➡ LUMO+5	15
				HOMO-8	➡ LUMO	41						
				HOMO-7	➡ LUMO+1	13						
				HOMO-6	➡ LUMO+1	10						
33	246.9	0.0586	B	HOMO-5	➡ LUMO+1	19	201.8	0.2210	A	HOMO-9	➡ LUMO	24
				HOMO	➡ LUMO+11	26				HOMO-2	➡ LUMO+5	10
34	246.0	0.1147	B	HOMO-7	➡ LUMO	32	201.6	0.3022	B	HOMO-4	➡ LUMO+2	36
				HOMO-6	➡ LUMO	14						
35	245.5	0.0018	A	HOMO-8	➡ LUMO	13	200.7	0.0554	A	HOMO-2	➡ LUMO+3	28
				HOMO-7	➡ LUMO+1	17				HOMO-1	➡ LUMO+3	10
				HOMO-6	➡ LUMO+1	56						

	B3LYP/6-31G*						CAM-B3LYP/6-31G*					
#	λ (nm)	f_{0f}	Symm.	Excitation		Cont. (%)	λ (nm)	f_{0f}	Symm.	Excitation		Cont. (%)
36	244.6	0.0096	B	HOMO-3	➡ LUMO+3	73	200.7	0.2529	B	HOMO-4	➡ LUMO+2	12
										HOMO-3	➡ LUMO+5	16
										HOMO-2	➡ LUMO+4	20
										HOMO-1	➡ LUMO+4	20
37	244.4	0.0123	A	HOMO-10	➡ LUMO	18	198.3	0.0051	A	HOMO-8	➡ LUMO+1	13
				HOMO-9	➡ LUMO	32				HOMO-6	➡ LUMO+1	14
				HOMO-7	➡ LUMO+1	16						
				HOMO-1	➡ LUMO+7	12						
38	243.8	0.0029	B	HOMO-1	➡ LUMO	18	198.2	0.0182	B	HOMO-9	➡ LUMO+1	14
				HOMO-9	➡ LUMO+1	10						
				HOMO-8	➡ LUMO+1	30						
				HOMO-1	➡ LUMO+6	18						
39	243.2	0.0008	B	HOMO-11	➡ LUMO	35	197.7	0.0195	A	HOMO	➡ LUMO+10	31
				HOMO-10	➡ LUMO+1	12						
				HOMO-9	➡ LUMO+1	25						
40	242.6	0.0009	A	HOMO-10	➡ LUMO	19	197.3	0.0646	B	HOMO-14	➡ LUMO	15
				HOMO-1	➡ LUMO+7	50						

APPENDIX F :

AUTHORIZATIONS FROM EDITORIAL OFFICES FOR USE OF COPYRIGHTED MATERIAL

Chapter 1: J. Phys. Chem. Lett. 2012, 3, 1808-1813. (American Chemical Society)

Chapter 2: Chem. Phys. Lett. 2013, 568-569, 176-183. (Elsevier)

ELSEVIER LICENSE
TERMS AND CONDITIONS

Apr 21, 2015

This is a License Agreement between Carlos E Diaz ("You") and Elsevier ("Elsevier") provided by Copyright Clearance Center ("CCC"). The license consists of your order details, the terms and conditions provided by Elsevier, and the payment terms and conditions.

All payments must be made in full to CCC. For payment instructions, please see information listed at the bottom of this form.

Supplier	Elsevier Limited The Boulevard,Langford Lane Kidlington,Oxford,OX5 1GB,UK
Registered Company Number	1982084
Customer name	Carlos E Diaz
Customer address	16203 East Alameda Place Apt #108 AURORA, CO 80017
License number	3613790331897
License date	Apr 21, 2015
Licensed content publisher	Elsevier
Licensed content publication	Chemical Physics Letters
Licensed content title	Overcoming the existent computational challenges in the ab initio calculations of the two-photon circular dichroism spectra of large molecules using a fragment-recombination approach
Licensed content author	None
Licensed content date	1 May 2013
Licensed content volume number	568
Licensed content issue number	n/a
Number of pages	8
Start Page	176
End Page	183
Type of Use	reuse in a thesis/dissertation
Portion	full article
Format	both print and electronic
Are you the author of this Elsevier article?	Yes
Will you be translating?	No
Title of your thesis/dissertation	STRUCTURE-PROPERTY RELATIONSHIP OF THE TWO-PHOTON CIRCULAR DICHROISM OF COMPOUNDS WITH AXIAL AND HELICAL

Chapter 3: J. Phys. Chem. A 2013, 117, 8416-8426. (American Chemical Society)

Chapter 4: J. Phys. Chem. A 2013, 117, 8416-8426. (American Chemical Society)

RightsLink®

Home | Account Info | Help | Live Chat

Title:	Two-Photon Circular Dichroism of an Axially Dissymmetric Diphosphine Ligand with Strong Intramolecular Charge Transfer
Author:	Carlos Díaz, Lorenzo Echevarria, Antonio Rizzo, et al
Publication:	The Journal of Physical Chemistry A
Publisher:	American Chemical Society
Date:	Feb 1, 2014

Logged in as: Carlos Diaz

LOGOUT

PERMISSION/LICENSE IS GRANTED FOR YOUR ORDER AT NO CHARGE

This type of permission/license, instead of the standard Terms & Conditions, is sent to you because no fee is being charged for your order. Please note the following:

- Permission is granted for your request in both print and electronic formats, and translations.
- If figures and/or tables were requested, they may be adapted or used in part.
- Please print this page for your records and send a copy of it to your publisher/graduate school.
- Appropriate credit for the requested material should be given as follows: "Reprinted (adapted) with permission from (COMPLETE REFERENCE CITATION). Copyright (YEAR) American Chemical Society." Insert appropriate information in place of the capitalized words.
- One-time permission is granted only for the use specified in your request. No additional uses are granted (such as derivative works or other editions). For any other uses, please submit a new request.

BACK | CLOSE WINDOW

Chapter 4: J. Phys. Chem. A 2013, 117, 8416-8426. (American Chemical Society)

Two-photon absorption and two-photon circular dichroism of hexahelicene derivatives: a study of the effect of the nature of intramolecular charge transfer

C. Díaz, Y. Vesga, L. Echevarria, I. G. Stará, I. Starỳ, E. Anger, C. Shen, M. El Sayed Moussa, N. Vanthuyne, J. Crassous, A. Rizzo and F. E. Hernández, *RSC Adv.*, 2015, **5**, 17429
DOI: 10.1039/C4RA16732E